


5-1-2017

Synthesis, Characterization and Biological Studies of Technetium-99m and Rhenium-188 Peptides

Vanessa Anne Sanders
University of Nevada, Las Vegas, vsndrs1@aol.com

Follow this and additional works at: <https://digitalscholarship.unlv.edu/thesesdissertations>

 Part of the [Nuclear Commons](#), and the [Radiochemistry Commons](#)

Repository Citation

Sanders, Vanessa Anne, "Synthesis, Characterization and Biological Studies of Technetium-99m and Rhenium-188 Peptides" (2017). *UNLV Theses, Dissertations, Professional Papers, and Capstones*. 3029. <https://digitalscholarship.unlv.edu/thesesdissertations/3029>

This Dissertation is protected by copyright and/or related rights. It has been brought to you by Digital Scholarship@UNLV with permission from the rights-holder(s). You are free to use this Dissertation in any way that is permitted by the copyright and related rights legislation that applies to your use. For other uses you need to obtain permission from the rights-holder(s) directly, unless additional rights are indicated by a Creative Commons license in the record and/or on the work itself.

This Dissertation has been accepted for inclusion in UNLV Theses, Dissertations, Professional Papers, and Capstones by an authorized administrator of Digital Scholarship@UNLV. For more information, please contact digitalscholarship@unlv.edu.

SYNTHESIS, CHARACTERIZATION AND BIOLOGICAL STUDIES
OF $^{99\text{M}}\text{Tc}$ AND ^{188}Re PEPTIDES

By

Vanessa Sanders

Bachelor of Arts- Chemistry
Florida Memorial University

2009

A dissertation submitted in partial fulfillment of the requirements for the

Doctor of Philosophy- Radiochemistry

Department of Chemistry and Biochemistry
College of Sciences
The Graduate College

University of Nevada, Las Vegas

May 2017

Copyright 2017 by Vanessa Sanders

All Rights Reserved



Dissertation Approval

The Graduate College
The University of Nevada, Las Vegas

April 21, 2017

This dissertation prepared by

Vanessa Sanders

entitled

Synthesis, Characterization and Biological Studies of Technetium-99m and Rhenium-188 Peptides

is approved in partial fulfillment of the requirements for the degree of

Doctor of Philosophy- Radiochemistry
Department of Chemistry and Biochemistry

Ken Czerwinski, Ph.D.
Examination Committee Co-Chair

Kathryn Hausbeck Korgan, Ph.D.
Graduate College Interim Dean

Lynn Francesconi, Ph.D.
Examination Committee Co-Chair

Jason Lewis, Ph.D.
Examination Committee Member

Brian Zeglis, Ph.D.
Examination Committee Member

Alex Barzilov, Ph.D.
Graduate College Faculty Representative

Abstract

Synthesis, Characterization and Biological Studies of ^{99m}Tc and ^{188}Re Peptides

Vanessa Sanders

Advisors: Ken Czerwinski and Lynn Francesconi

Radiopharmaceuticals are very powerful diagnostic tools for evaluation of a host of medical conditions. These drugs are labeled with radioactive isotopes, which are utilized to create pictures of areas of interest through absorption of the drug. They are currently in high demand due to their ability to image areas that traditional imaging devices cannot. The radioisotope ^{99m}Tc , with a half-life of 6.01 hours and a 140 keV gamma emission, is central to many radiopharmaceutical compounds. This isotope is easily obtained from a ^{99}Mo - ^{99m}Tc generator, through beta decay and column chromatography separations. Very little technetium, less than 6 ng, is needed to label the pharmaceuticals for use in-vivo. Another radioisotope ^{188}Re is also important due to its ability to be used for therapy while being tracked throughout the body. Radiotherapy gives radiopharmaceuticals a huge advantage by their ability to destroy rapidly growing cells. One of the main reasons there is interest in rhenium pharmaceuticals is the chemical similarity between it and technetium. The ^{188}Re isotope also has a considerably short half-life of approximately 17 hours and has emission energy of 155 keV. The ^{188}Re isotope is separated from ^{188}W - ^{188}Re generator, analogously to the ^{99}Mo - ^{99m}Tc generator.

The ligand used in this work is a pentapeptide macrocyclic ligand. This ligand, KYCAR (lysyl-tyrosyl-cystyl-alanyl-arginine), has been designed as a potential chelating ligand for

imaging and therapeutic *in vivo* agents. Ligands are chosen based on their in-situ biological behavior, and are used in the complexation with technetium and rhenium. Understanding and exploiting technetium and rhenium chemistry can provide insight into the reaction mechanisms and coordination chemistry of these compounds. The exploration of various oxidation states as a function of the ligands used and the reaction conditions can help develop novel radiopharmaceuticals. The investigations of the manipulation of oxidation states have the possible application to simplify the synthesis of the pharmaceutical. The versatility of the oxidation states of these metals leads to numerous possibilities in developing new radiopharmaceuticals.

The coordination chemistry and reaction mechanisms must be efficiently characterized to ensure the reproducibility of the radiopharmaceutical. The current study focuses on technetium and rhenium complexes with peptides. These complexes have become increasingly interesting for their use in diagnostic and therapeutic radiopharmaceuticals. The characterization of the complexation of Tc(V), and Rh(V) with the pentapeptide KYCAR (lysyl-tyrosyl-cystyl-alanyl-arginine) will be discussed. Complexes will be characterized by High Performance Liquid Chromatography (HPLC), UV-Visible Spectroscopy, Proton NMR, Circular Dichroism (CD), and Electrospray Ionization Mass Spectroscopy, to compare them to current radiopharmaceuticals. Information on the underlying reactions and coordination will be discussed.

Acknowledgements

First, I would like to thank Dr. Kenneth Czerwinski for all of the support and opportunities throughout the duration of my research. To the radiochemistry program at University of Nevada at Las Vegas, thank you for all of the support.

I would like to express my deep gratitude to Dr. Lynn Francesconi for allowing me to complete my thesis research in her laboratory. Her vast knowledge of this field and endless availability for discussions were key in making this research a success. Thank you for molding me into the scientist I am today. I would also like all of her lab members and Hunter College at the City University of New York for welcoming me and working with me as one of their own.

Thanks also go to Dr. Jason Lewis for contributing to intellectual discussions during these projects. Thank you to all of the members of the Lewis Laboratory at Memorial Sloan Kettering Cancer Center for all of your guidance with the biological studies. I would like to thank Brian Zeglis and the Zeglis laboratory at Hunter College at the City University of New York for all of the guidance and trouble-shooting through the pretargeting project. A sincere thank you to Dr. Alex Barzilov for your support in this thesis.

Special thanks David Iskhakov for being a great undergraduate researcher. Our intellectual conversations pushed me as a scientist. Thank you to Dalya Abdel-Atti for all of the animal and cell support and for all of the late-night experiments. Thanks to the Director of Nuclear Magnetic Resonance Dr. Matthew Devany for the support and conversations regarding the characterization of the metal-peptides. I would like to thank Dr. Michelle Neary, Director of

X-ray Crystallography, for the willingness to answer the crystallization question and for supporting the crystallization part of this thesis.

To my Squeegee crew, thank you thank you thank you. I cannot thank you enough for all of your motivation through this thesis. Thank you for the intellectual guidance to become a better scientist, and life guidance to become a better person. To my support network from Florida to Nevada to New York, thank you for always just being there.

Finally, I would like to thank my mother, Valeria Sanders, for your endless support and belief in me, I could not have done this without you.

To my motivation

My Heart:

My Daddy,

John C. Sanders

Table of Contents

Abstract.....	iii
Acknowledgements.....	v
Table of Contents.....	viii
List of Tables.....	xi
List of Figures.....	xiv
1. Introduction.....	1
1.1. Background.....	1
1.2. PET/ SPECT Instrumentation.....	5
1.3. Technetium Chemistry and ^{99m} Tc Radiopharmaceuticals.....	9
1.4. Rhenium Chemistry and ¹⁸⁸ Re Radiopharmaceuticals.....	18
1.5. Ligands, Linkers, Targeting Vectors, Pre-Targeting.....	21
2. Synthesis and Characterization of Re, ^{99m} Tc, and ¹⁸⁸ Re Pentapeptides.....	25
2.1. Introduction.....	25
2.2. Materials.....	30
2.3. Syntheses.....	30
2.4. HPLC Analyses.....	32
2.5. Mass Spectrometry Analysis.....	33

2.6.	NMR Analysis.....	33
2.7.	Infrared Spectroscopy	34
2.8.	Circular Dichroism Analysis	34
2.9.	Crystallization	35
2.10.	X-ray Structure Determination	36
2.11.	LogD Studies	36
2.12.	Biodistribution Studies	36
2.13.	Results and Discussion.....	37
2.14.	Conclusion	89
3.	^{99m} Tc and ¹⁸⁸ Re Pretargeting Spect and Radioimmunotherapy Agents Employing Bioorthogonal Diels Alder Click Chemistry	92
3.1.	Introduction.....	92
3.2.	Materials	95
3.3.	Synthesis.....	96
3.4.	HPLC Analysis	98
3.5.	Mass Spectrometry Analysis	99
3.6.	Proton NMR Analysis.....	99
3.7.	Infrared Spectroscopy	100
3.8.	LogD Studies	100

3.9. SPECT Imaging	100
3.10. Biodistribution Studies	101
3.11. Results and Discussion.....	101
3.12. Conclusion	142
4. Summary.....	144
5. Future Work.....	147
References	149
Curriculum Vitae	157

List of Tables

Table 1. List of Commonly Used Radionuclides for Radiopharmaceuticals	4
Table 2. Summary of Notable Tc Pharmaceuticals	16
Table 3. Current Preclinical and Clinical Trials with ¹⁸⁸ Re-labelled Agents ³⁷	20
Table 4. ¹ H NMR of KYCAR, ReO-KYCAR peak 1, ReO-KYCAR peak 2, and the change (Δ) in ppm between peak 1 and peak 2	50
Table 5. Chemical shifts (middle column) of the alpha proton on the lysine of ReO-KYCAR at various pH. The first and last columns represent the x and y axes for the following figure.....	56
Table 6. Chemical shifts (middle column) of the epsilon proton on the lysine of ReO-KYCAR at various pH. The first and last columns represent the x and y axes for the following figure.....	58
Table 7. Chemical shifts (middle column) of the alpha proton on the lysine of free KYCAR at various pH. The first and last columns represent the x and y axes for the following figure.....	60
Table 8. Chemical shifts (middle column) of the epsilon proton on the lysine of free KYCAR at various pH. The first and last columns represent the x and y axes for the following figure.....	62
Table 9. Summary of Crystallization Results ReO-KYCAR Peak1 (anti).....	70
Table 10. Summary of Crystallization Results ReO-KYCAR Peak 2 (syn).....	71
Table 11. Crystal and Structure Refinement Data for ReO-KYC Peak 2 (syn)	75
Table 12. Bond Lengths and Bond Angles for ReO-KYC Peak 2 (Syn)	76
Table 13. ^{99m} TcO-KYCAR(syn). The results are reported in %ID/g. Shows that the activity travels through the gastrointestinal track. Also shows some decomposition to ^{99m} TcO ₄ ⁻ as seen with thyroid accumulation	82

Table 14. $^{188}\text{ReO-KYCAR}$ (syn) The results are reported in %ID/g. Shows that the activity travels through the gastrointestinal track. Also shows some decomposition to $^{99\text{m}}\text{TcO}_4^-$ as seen with thyroid and stomach accumulation 88

Table 15. Biodistribution of $^{99\text{m}}\text{TcO-KYCAR-Sh-Tz}$. The results are reported in %ID/g. Shows that the activity travels through the gastrointestinal track. 112

Table 16. Biodistribution of $^{188}\text{ReO-KYCAR-Sh-Tz}$. The results are reported in %ID/g. Shows that the activity travels through the gastrointestinal track. Also shows some decomposition to $^{188}\text{ReO}_4^-$ through stomach and thyroid accumulation. 115

Table 17. Biodistribution of $^{99\text{m}}\text{TcO-KYCAR-PEG}_5\text{-Tz}$. The results are reported in %ID/g. Shows that the activity travels through the gastrointestinal track. Also shows some decomposition to $^{99\text{m}}\text{TcO}_4^-$ over time through slow thyroid accumulation..... 118

Table 18. Biodistribution of $^{188}\text{ReO-KYCAR-PEG}_5\text{-Tz}$. The results are reported in %ID/g. Shows that the activity travels through the gastrointestinal track. Also shows some decomposition to $^{188}\text{ReO}_4^-$ through stomach and thyroid accumulation. 121

Table 19. Pre-clicked Biodistribution of $^{99\text{m}}\text{TcO-KYCAR-PEG}_5\text{-Tz-A33-TCO}$. The results are reported in %ID/g. Shows retention of activity in the blood due to long circulation time. Also shows significant tumor uptake..... 124

Table 20. Pretargeted Biodistribution of $^{99\text{m}}\text{TcO-KYCAR-Sh-Tz}$. The results are reported in %ID/g. Shows an unusual high accumulation in the muscle. There is some decomposition $^{99\text{m}}\text{TcO}_4^-$ accumulating over time in the thyroid, a minimal tumor uptake. 128

Table 21. Pretargeted Biodistribution of $^{188}\text{ReO-KYCAR-Sh-Tz}$. The results are reported in %ID/g. Shows an unusual high accumulation in the muscle. There is some decomposition $^{188}\text{ReO}_4^-$ accumulating in the thyroid and stomach, Minimal tumor uptake. 132

Table 22. Pretargeted Biodistribution of $^{99m}\text{TcO-KYCAR-PEG}_5\text{-Tz}$. The results are reported in %ID/g. Shows possible unclicked $^{99m}\text{TcO-KYCAR-PEG}_5\text{-Tz}$ in the gastrointestinal track. Shows slow accumulation at the tumor site. 136

Table 23. Pretargeted Biodistribution of $^{188}\text{ReO-KYCAR-PEG}_5\text{-Tz}$. The results are reported in %ID/g. Shows high accumulation in the gastrointestinal track. There is decomposition $^{188}\text{ReO}_4^-$ accumulating in the thyroid and stomach, Minimal tumor uptake. 140

List of Figures

Figure 1. Positron emission and annihilation	6
Figure 2. Photoelectric effect and Compton scattering	8
Figure 3. Periodic Table of Elements	9
Figure 4. Decay chain of Tc from fission products	10
Figure 5. Decay Scheme of $^{99}\text{MoO}_4^{2-}$ to $^{99\text{m}}\text{TcO}_4^-$: The Chemistry of the Tc Generator	12
Figure 6. Tagged Radiopharmaceuticals	13
Figure 7. Examples of Technetium Cores.....	15
Figure 8. Pretargeted Click Chemistry Approach.....	23
Figure 9. KYCAR Ligand	27
Figure 10. Anti and Syn Diastereomers of ReO-KYCAR.....	28
Figure 11. Kinetic study of ReO-KYCAR over 10 day period. Immediately post synthesis there are three peak present (A,B,C). Peak A (intermediate peak) converts to peak B (peak 1), which converts to peak C (peak 2).	38
Figure 12. Mass spectroscopy of ReO-KYCAR peak B molecular ion $[\text{M} + \text{H}]^+$ peak at m/z 840 which corresponds to an exact mass of 839.24 g/mol.	39
Figure 13. Structure of ReO-KYCAR + Methyl Ester Adduct	40
Figure 14. Mass Spectroscopy of ReO-KYCAR + Methyl Ester Adduct	41
Figure 15. Kinetic study ReO-KYCAR in acetonitrile. Initially reveals three peaks (A, B, and C). Shows that peak B does not interconvert to peak C	42
Figure 16. HPLC Trace $^{99\text{m}}\text{TcO-KYCAR}$	44

Figure 17. Coelution of $^{99m}\text{TcO-KYCAR}$ with ReO-KYCAR Peak 1(anti).....	45
Figure 18. HPLC Trace of $^{188}\text{ReO-KYCAR}$	46
Figure 19. Coelution of $^{188}\text{ReO-KYCAR}$ with ReO-KYCAR	46
Figure 20. Structures of ReO-KYCAR diastereomers (Anti and Syn).....	48
Figure 21. ReO-KYCAR Structure Labelled with 1-letter Amino Acid Code	49
Figure 22. ReO-KYCAR Peak 2 (Syn) Downfield Aliphatic TOCSY	52
Figure 23. ReO-KYCAR Peak 2 (syn) Upfield Aliphatic TOCSY	53
Figure 24. NMR Titration Curve for ReO-KYCAR. Connected dots represent the lysine alpha proton, and the connected squares represent the lysine epsilon protons.....	54
Figure 25. NMR Titration Curve for the free KYCAR ligand. Connected dots represent the lysine alpha proton, and the connected squares represent the lysine epsilon protons.....	55
Figure 26. NMR titration curve for ReO-KYCAR alpha proton on the lysine. $\text{pK}_a=6.00$ plotted by Prism via sigmoidal curve fit. Free solid dots represent experimental data points, dashed and solid lines are representative of the sigmoidal curve fit.	57
Figure 27. NMR titration curve for ReO-KYCAR epsilon proton on the lysine. $\text{pK}_a=7.53$ plotted by Prism via sigmoidal curve fit. Free solid dots represent experimental data points, dashed and solid lines are representative of the sigmoidal curve fit.	59
Figure 28. NMR titration curve for free KYCAR alpha proton on the lysine. $\text{pK}_a=7.48$ plotted by Prism via sigmoidal curve fit. Free solid dots represent experimental data points, dashed and solid lines are representative of the sigmoidal curve fit.	61

Figure 29. NMR titration curve for free KYCAR epsilon proton on the lysine. $pK_a=10.28$ plotted by Prism via sigmoidal curve fit. Free solid dots represent experimental data points, dashed and solid lines are representative of the sigmoidal curve fit. 63

Figure 30. IR Spec. of KYCAR(Top), Re starting material, ReO-KYCAR peak 1, ReO-KYCAR peak 2(Bottom)..... 65

Figure 31. Circular Dichorism of ReO-KYCAR Peak 1(anti) (Black), and ReO-KYCAR Peak 2 (syn) (Blue)..... 66

Figure 32. Comparison of Previously Reported Anti and Syn Metal-Peptides..... 68

Figure 33. Stucture of ReO-KYC 73

Figure 34. Reversed Phase HPLC of ReO-KYC Post Synthesis. Shows 2 major peaks. Peak 1 (anti) and peak 2 (syn) 74

Figure 35. Ball and Stick Diagram for ReO-KYC (syn) 77

Figure 36. Reversed phase HPLC of ReO-KYC syn crista confirming that peak 2 corresponds to the syn crystal structure. 78

Figure 37. HPLC of $^{99m}\text{TcO-KYCAR (syn)}$ in PBS monitored over time..... 80

Figure 38. HPLC of $^{99m}\text{TcO-KYCAR (syn)}$ in Human Serum monitored over time 81

Figure 39. $^{99m}\text{TcO-KYCAR(syn)}$. The results are reported in %ID/g. Shows that the activity travels through the gastrointestinal track. Also shows some decomposition to $^{99m}\text{TcO}_4^-$ as seen with thyroid accumulation 83

Figure 40. HPLC of $^{188}\text{ReO-KYCAR (syn)}$ in PBS monitored over time..... 85

Figure 41. HPLC of $^{188}\text{ReO-KYCAR (syn)}$ monitored in Human Serum over time..... 86

Figure 42. $^{188}\text{ReO-KYCAR}$ (syn) The results are reported in %ID/g. Shows that the activity travels through the gastrointestinal track. Also shows some decomposition to $^{99\text{m}}\text{TcO}_4^-$ as seen with thyroid and stomach accumulation	89
Figure 43. Structure of tetrazine-NHS ester (sh-Tz).....	94
Figure 44. Structure tetrazine-PEG ₅ -NHS ester (PEG ₅ -Tz)	95
Figure 45. Lysine-tetrazine Reaction Mechanism.....	102
Figure 46. HPLC of ReO-KYCAR-Sh-Tz showing one major peak.....	103
Figure 47. Mass Spectroscopy of ReO-KYCAR-Sh-Tz molecular ion $[\text{M} + \text{H}]^+$ peak at m/z 1038 which corresponds to an exact mass of 1037.30 g/mol.	104
Figure 48. HPLC of ReO-KYCAR-PEG5-Tz showing one major peak	105
Figure 49. Mass Spectroscopy of ReO-KYCAR-PEG ₅ -Tz molecular ion $[\text{M} + \text{H}]^+$ peak at m/z 1329 which corresponds to an exact mass of 1328.47 g/mol.	106
Figure 50. Coelution of ReO-KYCAR-Sh-Tz and $^{99\text{m}}\text{TcO-KYCAR-Sh-Tz}$	107
Figure 51. Coelution of ReO-KYCAR-PEG5-Tz and $^{99\text{m}}\text{TcO-KYCAR-PEG5-Tz}$	108
Figure 52. Infrared Spectra of ReO-KYCAR-Sh-Tz	110
Figure 53. Infrared Spectra of ReO-KYCAR-PEG5-Tz.....	111
Figure 54. Biodistribution of $^{99\text{m}}\text{TcO-KYCAR-Sh-Tz}$. The results are reported in %ID/g. Shows that the activity travels through the gastrointestinal track.	113
Figure 55. Biodistribution of $^{188}\text{ReO-KYCAR-Sh-Tz}$. The results are reported in %ID/g. Shows that the activity travels through the gastrointestinal track. Also shows some decomposition to $^{188}\text{ReO}_4^-$ through stomach and thyroid accumulation.	116

Figure 56. Biodistribution of $^{99m}\text{TcO-KYCAR-PEG}_5\text{-Tz}$. The results are reported in %ID/g. Shows that the activity travels through the gastrointestinal track. Also shows some decomposition to $^{99m}\text{TcO}_4^-$ over time through slow thyroid accumulation..... 119

Figure 57. Biodistribution of $^{188}\text{ReO-KYCAR-PEG}_5\text{-Tz}$. The results are reported in %ID/g. Shows that the activity travels through the gastrointestinal track. Also shows some decomposition to $^{188}\text{ReO}_4^-$ through stomach and thyroid accumulation. 122

Figure 58. Pre-clicked Biodistribution of $^{99m}\text{TcO-KYCAR-PEG}_5\text{-Tz-A33-TCO}$. The results are reported in %ID/g. Shows retention of activity in the blood due to long circulation time. Also shows significant tumor uptake..... 125

Figure 59. SPECT Images of pre-clicked $^{99m}\text{TcO-KYCAR-PEG}_5\text{-Tz-A33-TCO}$. A large amount of activity is found in the blood pool through all time points. However, shows significant tumor uptake by 8 hours. The tumor is marked by the white arrow..... 127

Figure 60. Pretargeted Biodistribution of $^{99m}\text{TcO-KYCAR-Sh-Tz}$. The results are reported in %ID/g. Shows an unusual high accumulation in the muscle. There is some decomposition $^{99m}\text{TcO}_4^-$ accumulating over time in the thyroid, a minimal tumor uptake..... 129

Figure 61. Pretargeted SPECT Images of $^{99m}\text{TcO-KYCAR-Sh-Tz}$. Shows high accumulation in the gallbladder in early time points. There is a large amount of gut uptake. Tumor uptake at 1 and 4 hours post injection is observed and distinctive. The tumor is marked by the white arrow..... 131

Figure 62. Pretargeted Biodistribution of $^{188}\text{ReO-KYCAR-Sh-Tz}$. The results are reported in %ID/g. Shows an unusual high accumulation in the muscle. There is some decomposition $^{188}\text{ReO}_4^-$ accumulating in the thyroid and stomach, Minimal tumor uptake. 133

Figure 63. Pretargeted SPECT Images of $^{188}\text{ReO-KYCAR-Sh-Tz}$. Shows high accumulation in the gallbladder, small intestines and bladder. Tumor uptake is not observed. Tumor is marked by the white arrow. 135

Figure 64. Pretargeted Biodistribution of $^{99\text{m}}\text{TcO-KYCAR-PEG}_5\text{-Tz}$. The results are reported in %ID/g. Possible unclicked $^{99\text{m}}\text{TcO-KYCAR-PEG}_5\text{-Tz}$ is found in the gastrointestinal track. These data show slow accumulation at the tumor site. 137

Figure 65. Pretargeted SPECT Images $^{99\text{m}}\text{TcO-KYCAR-PEG}_5\text{-Tz}$. Shows high accumulation in the gallbladder, small intestines and bladder. Tumor uptake is observed and discernable throughout the experiment. The tumor is marked by the white arrow. 139

Figure 66. Pretargeted Biodistribution of $^{188}\text{ReO-KYCAR-PEG}_5\text{-Tz}$. The results are reported in %ID/g. Shows high accumulation in the gastrointestinal track. There is decomposition $^{188}\text{ReO}_4^-$ accumulating in the thyroid and stomach, Minimal tumor uptake. 141

1. Introduction

1.1. Background

Radiopharmaceuticals are very powerful diagnostic or therapeutic tools for evaluation of a host of medical conditions, which include defect in organs, infection and most notably cancer. In 2014 over 14 million people reported having a history of cancer and nearly 2 million people would be diagnosed within the next few years.¹ As the amount of people diagnosed and the need for earlier detection increases the demand for optimal radiopharmaceuticals also increases.

By definition radiopharmaceuticals are drugs, organic or bioorganic molecules, that include a radionuclide. The radionuclides, depending on the isotope emit particles and can be utilized to create pictures or induce therapy on areas of interest through absorption of the drug.^{2,3} Before a radionuclide can be incorporated into a drug it first must possess certain properties for radioimaging or radiotherapy. Depending on the application must emit ionizing particles, alpha (α), beta (β), or gamma (γ). Specifically, for radioimaging the particles must emit penetrating radiation which consists of gamma rays, either direct or through positron emission. The energies of the gamma rays are dependent on the nature of the gamma particle and are used with specific detection instruments. For instance, gamma particles that are the product of the annihilation of positron are 511 keV and are released at approximately 180° from each other. Nuclides that emit positron particles, and the resulting 511 keV photons, are exclusively used in Positron Emission Tomography (PET). Nuclides that

emit incident gamma rays are typically used with Single Photon Emission Computed Tomography if their energies are within the range of 100- 250 keV.

Next, the nuclide of interest must have a half-life, the time in which half the particles have decayed, that is of an adequate length. An effective half-life is one where there is sufficient activity to image the area of interest post synthesis, purification, and injection. In order to reduce dose to the patient the nuclide should also decay to a stable daughter or to a nuclide with a relatively short biological half-life.

Finally, the cost and availability to produce the nuclide of interest plays an important role. Most nuclides are produced by cyclotrons, accelerators, or through a generator system. Accelerators/ cyclotron production systems have the potential to produce multiple isotopes at a single location. This increases the application, allowing for detailed exploration through the utilization of multiple isotopes. However, production utilizing this system can be expensive and limits availability to areas outside of the production facility. Alternatively, a generator system, where a parent or longer-lived nuclide is adsorbed onto a chromatographic column and as it decays the shorter-lived nuclide of interest is eluted for use. This production system is more cost effective and since the generator can be shipped the nuclides of interest become more available. An isotope can possess excellent energies and optimal half-lives, however if it is impractical to produce it will not be a good candidate for a radiopharmaceutical.

Some of the first radionuclides produced for medical commercial use were ^{24}Na , ^{32}P , and most notably ^{131}I . Phosphorus and sodium were used during that time to analyze cardiac

functions.^{4, 5} Iodine is currently being used for imaging and therapy after uptake in the thyroid was noticed as early as 1938.^{6, 7} One of the first myocardial scintigraphy radiopharmaceuticals used, that is still used today, was ^{201}Tl , and was discovered by Strauss et al. in 1975.⁸ Many nuclear medicine scans are used for the detection of bone metastases. Bone scintigraphy began in the 1960's using ^{85}Sr as the radionuclide. Many of these early radionuclides have been replaced with $^{99\text{m}}\text{Tc}$, presently the most widely used diagnostic radioisotope. Table 1 shows some of the commonly used radionuclides for radiopharmaceuticals.

Commonly Used Radionuclides				
Radionuclide	Half-life	Most Common Production Methods	Particle Emission	Application
^{11}C	20.3 m	Cyclotron	β^+	PET
^{18}F	109.7 m	Cyclotron	β^+	PET
^{67}Ga	78 h	Cyclotron	EC	SPECT
^{68}Ga	68 m	Generator	β^+	PET
^{111}In	2.80 d	Cyclotron	EC	SPECT
$^{99\text{m}}\text{Tc}$	6.01 h	Generator	IT	SPECT
^{131}I	8.02 d	Reactor	β^-	Therapy
^{82}Rb	1.27 m	Generator	β^+	PET
^{201}Tl	3.05 d	Generator	EC	SPECT
^{123}I	13.2 h	Cyclotron	EC	SPECT
^{89}Zr	78.4 h	Accelerator/Cyclotron	β^+	PET
^{90}Y	64.1 h	Reactor	β^-	Therapy
^{64}Cu	12.7 h	Accelerator	β^+	PET

Table 1. List of Commonly Used Radionuclides for Radiopharmaceuticals

1.2. PET/ SPECT Instrumentation

Early detection of diagnostic radiopharmaceuticals utilized basic gamma cameras for planar imaging. In this practice as the emitted gamma was being detected, a lead collimator was used to guarantee that the path of the particles being collected parallel to one another. From there the particles were transformed from photons to visible light using a scintillator and the particles are amplified through photomultiplier tubes. Finally, the origin of the incident is determined from various electronics and a 2D picture is created. While this was a novel technique, one major trepidation was the attenuation of the emitted particle by other organs. Also, the lack of sensitivity within the detector results in poor resolution of the final image. As a result, currently there are two main modalities used for the detection of incident particles and tomographic reconstruction.

Positron Emission Tomography (PET) imaging employs the use of radionuclides that emit positrons. Most commonly the isotope ^{18}F and the compound fluorodeoxyglucose are used in the PET imaging to measure tissue metabolism. These positrons are subsequently annihilated upon interaction with an electron producing two 511 keV photons (Figure 1).⁹ The photons are emitted approximately 180° from each other which enhances the reconstruction of the location of the incident event. The detectors are configured as a circular ring of block detectors coupled to photo multiplier tubes. The scintillation crystals, which convert the photons to visible light, are used to achieve more incidences thus allowing for better spatial resolution. When both photons are detected simultaneously within the timing window of about 10 ns a line of

response is created. Through additional electronics and the summation of the created line of response an image is formed.^{10, 11} The main advantage for PET imaging is better resolution of the images than found in SPECT imaging. This does not negate the fact that the instrumentation has room for improvement. The performance of the instrument can be enhanced by the optimizing the scintillation crystals, photo multiplier tubes and the geometry and location of the detectors.¹²

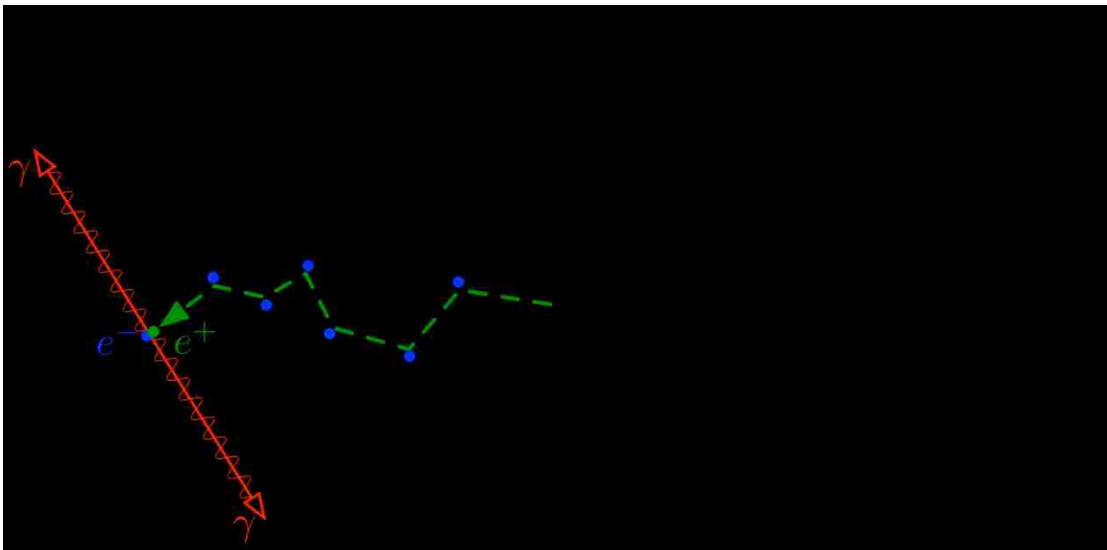


Figure 1. Positron emission and annihilation

Single Photon Emission Computed Tomography (SPECT) imaging evolved from the first planar detector used in nuclear medicine. Typically, nuclides used with SPECT imaging are those that emit gamma particle with energies ranging between 100-250 keV. The most common radionuclide that utilizes this application is ^{99m}Tc . These gamma rays are produced through one

of two mechanisms: the photoelectric effect or Compton scattering. In the photoelectric effect, an incident photon displaces an inner electron from its shell, as it deexcites a photon is emitted. Conversely in Compton scattering an incident photon is deflected resulting from its interaction with an inner electron (Figure 2).¹³ The major disadvantage to SPECT imaging is the poor resolution compared to PET, attributed to many factors with the detector system as well as keeping the dose low to the patient. Collimators play an important role in the detection of gamma particles and assist in determining the location of the incident event. This is due to the collimator only recording events from a specific position and direction, eliminating all other gamma particles. In early SPECT designs the detector used is often noted as the Anger camera^{14, 15}, consisting of a collimator, scintillation crystal, and photon multiplier tubes.¹⁶ Since the primary goal is a local image of the area of interest optimization of the detection system is of utmost importance. To suppress photons that may have scattered upon exiting tissue only photons of a specific energy are recorded. Also, multiple scintillation crystals were introduced to increase the probability of interaction with the photon. Another approach is replacing the crystal, typically NaI(Tl), with solid state detectors. As further research on improving the components of the detector system is completed the overall resolution will improve. Currently, to circumvent resolution issues SPECT systems are coupled with computed tomography (CT) systems to improve the quality of the images.¹⁷

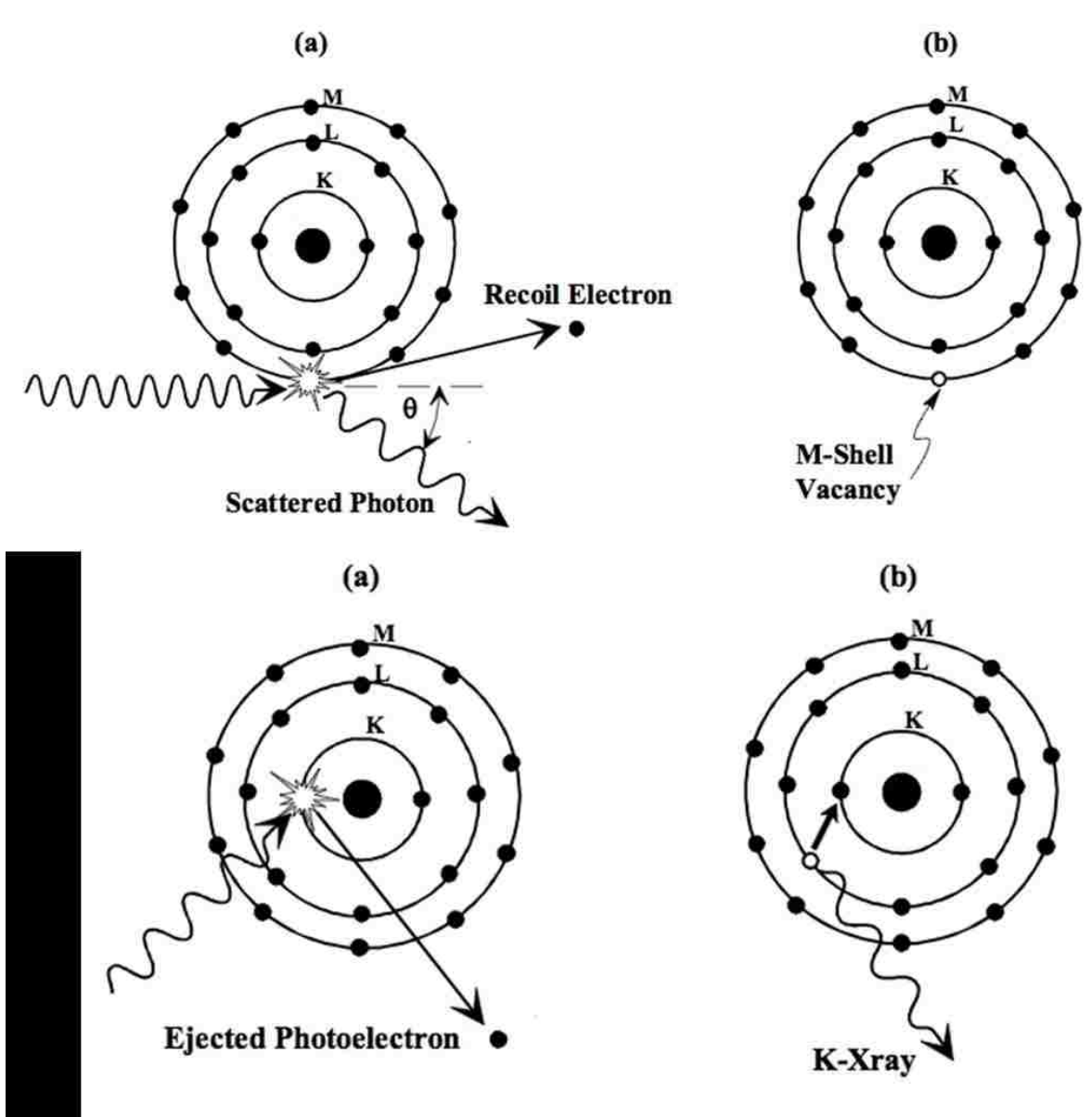


Figure 2. Photoelectric effect and Compton scattering

1.3. Technetium Chemistry and ^{99m}Tc Radiopharmaceuticals

Technetium, the most widely used medical isotope, is a transition metal which sits in the middle of the periodic table (Figure 3). The lightest synthetic element was discovered in 1937 by Pierre and Segre through a cyclotron irradiation of molybdenum foil.¹⁸

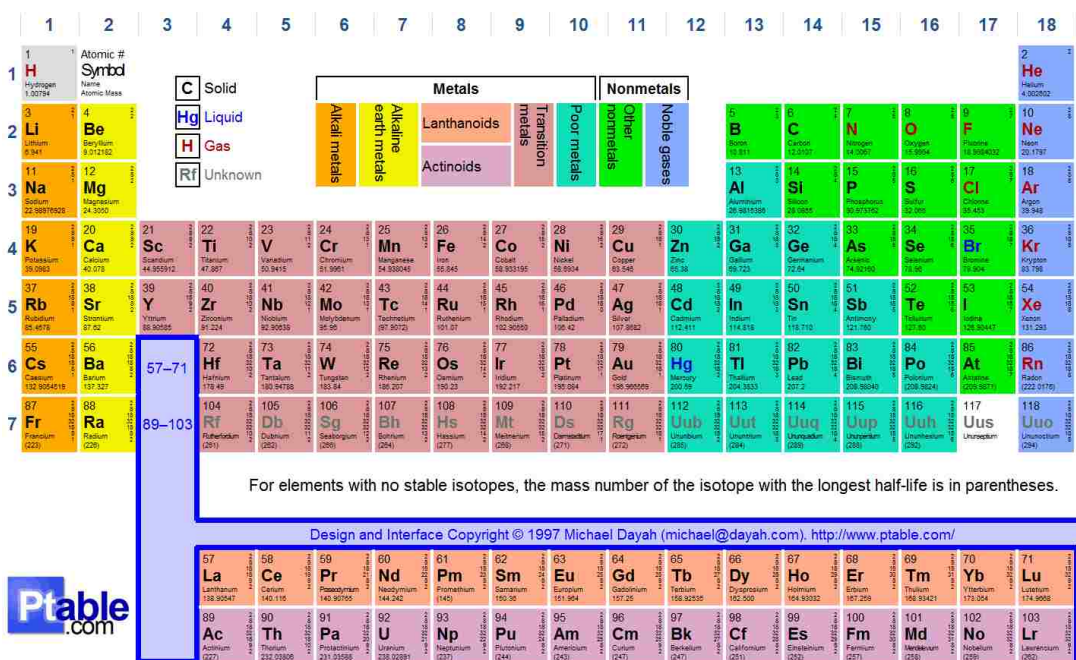


Figure 3. Periodic Table of Elements

It is the lightest synthetic elements with an atomic number of 43 and over 30 isotopes. The most common isotope of technetium is ⁹⁹Tc, which has a half-life of 21000 years is produced

as a fission product of uranium ion nuclear reactors (Figure 4). The A=99 isobar have a cumulative fission yield of 6.1% from the fission of ^{235}U by thermal neutrons.¹⁹ While the independent fission yield of $^{99\text{m}}\text{Tc}$ is relatively low, the isobaric beta decay produces the isotope through ^{99}Mo with a half-life of 2.747 days. The stable end member of the A=99 fission product isobar is ^{99}Ru .

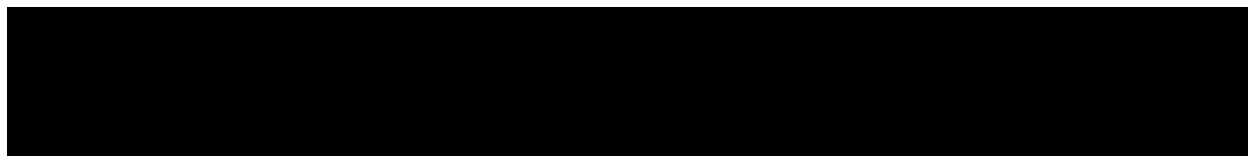


Figure 4. Decay chain of Tc from fission products

The isotope ^{99}Tc is separated from the other fission products through various reprocessing techniques, such as liquid-liquid extraction via the uranium extraction (UREX) process. Trace amounts of technetium can also be found in the earth's crust, as ^{98}Tc , and in red giant stars.²⁰ Despite being the lightest artificial element technetium has a vast interesting chemistry with oxidation states ranging from -1 to +7. Technetium can form chemical bonds consisting of pi electrons and sigma electrons, that can be of colligative and coordinative types when spin compensation and electron pair donation occurs.²¹ Compounds have been reported

with coordination chemistries from 4 to 9 which allows for complexation to a wide range of ligands.

The isotope ^{99m}Tc is central to many radiopharmaceutical compounds and is used in over 85% of nuclear diagnostic tests, with over 25 million completed procedures each year.²² It has excellent physical properties (half-life= 6.02 hrs, gamma emission= 142 keV) and has optimal medicinal characteristics. Less than 6 ng is needed to label the pharmaceuticals for use *in vivo*. Also, the low γ ray energy allows for optimal imaging with current gamma camera technology, and its short half-life insures that the radiopharmaceutical can be injected with minimal radiation burden to the patient.^{23, 24}

The production of ^{99m}Tc is facile and can be available to medical centers through the use of the $^{99}\text{Mo}/^{99m}\text{Tc}$ generator, discovered by Brookhaven National Laboratory,²⁵ with a shelf life of one week. Briefly the parent isotope, ^{99}Mo (half-life= 66 hrs) as MoO_4^{2-} is adsorbed onto an alumina column. As ^{99}Mo continuously decays $^{99m}\text{TcO}_4^-$ is separated using saline, owing to the charge difference (Figure 5). Following the elution, the peak activity of ^{99m}Tc accumulates on the alumina column within 24 hours. However, if necessary the generator can be eluted earlier producing about half of the activity within 8 hours.²⁶

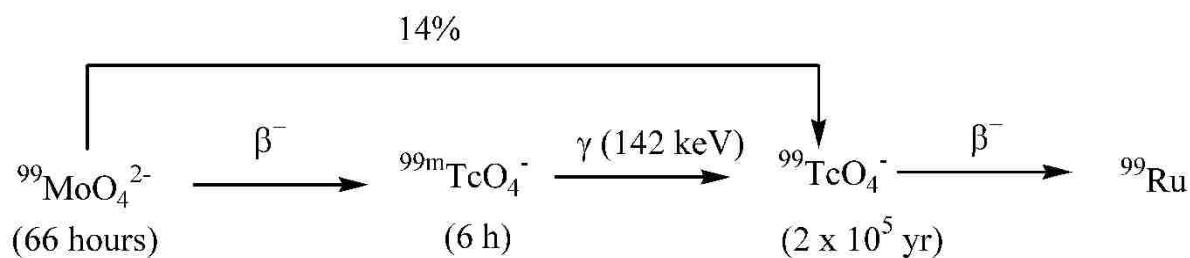


Figure 5. Decay Scheme of ${}^{99}\text{MoO}_4^{2-}$ to ${}^{99m}\text{TcO}_4^-$: The Chemistry of the Tc Generator

Once eluted $\text{Na}^{99m}\text{TcO}_4$ is the conventional starting material for the majority of ${}^{99m}\text{Tc}$ radiopharmaceuticals. Generally, the eluate is introduced to a ‘kit’ containing a reducing agent, the ligand of choice and buffers. These instant kits were developed in the 1970 shortly after the development of several Tc imaging agents. The entire kit is then incubated at an elevated temperature and followed by purification before use. The development of the instant kits propelled the advancement of Tc radiopharmaceutical discovery, and by the late 1970’s ${}^{99m}\text{Tc}$ brain heart and renal imaging agents had been discovered.²⁷

The first group of explored ${}^{99m}\text{Tc}$ imaging agents is tagged as “Tc essential” radiopharmaceuticals. These are the simplest and oldest agents with respect to radiopharmaceutical structure. These are non-targeted complexes that showed uptake in areas of interest due to the size, charge and lipophilicity of the complex. Examples include ${}^{99m}\text{Tc}$ -DTPA, and ${}^{99m}\text{Tc}$ -DMSA, for the imaging of renal function. The second generation of imaging agents consisted of complexes where the design and structure was deliberate, characterized

and understood. Several brain and kidney ^{99m}Tc agents, for example ^{99m}Tc -HMPAO and ^{99m}Tc -Mag₃, are included in this generation.

The next wave of Tc imaging agents came around the late 1980's, and involved Tc-complexes bound to a biologically active molecule through the use of a linker molecule. Figure 6 shows a depiction of a "tagged radiopharmaceutical". Here Tc is complexed to a ligand; the resulting molecule has an available linker portion that can be used to conjugate to a targeting vector, usually a biologically active molecule (BAM).



Figure 6. Tagged Radiopharmaceuticals

In this class of Tc radiopharmaceuticals, the targeting vector determines the distribution of the agent in the body by utilizing antibody/ antigens, or molecular targeted receptors. The ^{99m}Tc apcitide ($^{99m}\text{TcO}(\text{P246})$) was the first radiolabeled peptide used in nuclear medicine. Complexation of Tc with the 13 amino acid shows high affinity and selectivity for the GPIIb/IIa

receptors. This agent has been successfully incorporated into a lyophilized kit with the trade name AcuTect™, and used to image deep vein thrombosis.²⁸⁻³⁰

Pertechnetate, $^{99m}\text{TcO}_4^-$, has an oxidation state of +7. However, many ^{99m}Tc radiopharmaceuticals require an oxidation state of +5 for complexation to ligands. When pertechnetate is reduced, typically by a stannous ion, a technetium(V)-oxo core is formed. This technetium core describes a group of stable structures by which ligands can coordinate (Figure 7).²⁷ The Tc-oxo, $\text{Tc}=\text{O}^{3+}$, core is most often used in conjugation with radiopharmaceuticals, typically N_3S , or N_2S_2 tetradentate ligands. Upon formation with these ligands the geometry becomes square pyramidal with the Tc-oxo core in the apical position. The mechanism associated with N_3S or similar ligand is a very strong bond between Tc^{V} and the thiolate followed by a deprotonation of the amide nitrogens resulting in a tetradentate complexation. When chiral centers are present in the ligand it is typical that diastereomers form, where side chains within the ligand are syn or anti to the Tc=oxo group. Tc radiopharmaceuticals have been used to image a vast array of areas within the body. The most notable are tabulated in the table below (Table 2).

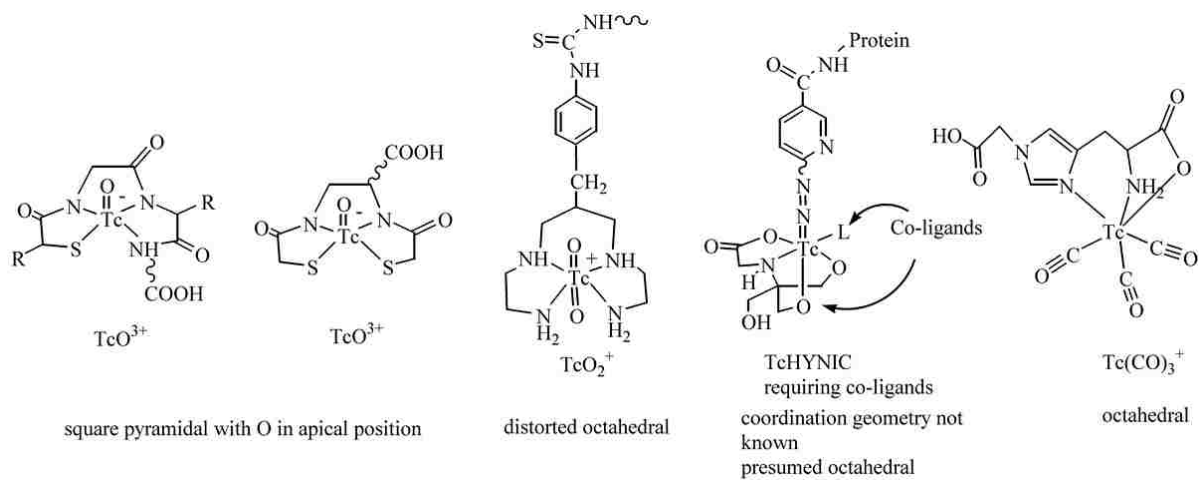


Figure 7. Examples of Technetium Cores

Agent	Commercial Name	Oxidation State	Area of Interest
^{99m} Tc-MIBI	CardioLite	I	Heart
^{99m} Tc-BATO	Cadiotec	III	Heart
^{99m} Tc-Furifosmin	TechneScan Q12	III	Heart
^{99m} Tc-Methyl Diphosphonate	^{99m} Tc-MDP	IV	Bone
^{99m} Tc-Tertrofosmin	Myoview	V	Heart
^{99m} Tc-HMPAO	Certec	V	Brain
^{99m} Tc-ECD	Neurolite	V	Brain
^{99m} Tc-Mag3	Technescan	V	Kidneys
^{99m} Tc-Apcitide	AcuTect	V	Deep Vein Thrombosis
^{99m} Tc-Depreotide	NeoTect	V	Neuroendocrine Tumors

Table 2. Summary of Notable Tc Pharmaceuticals

^{99m}Tc-Depreotide was the next technetium labelled peptide to enter the clinic, and shows affinity for the somatostatin receptor. This agent thus has the ability to imaging neuroendocrine tumors. This agent proved interesting due to the observation of syn and anti diastereomers upon complexation with Tc. ³¹

Imaging the brain proved to be difficult when the blood brain barrier is intact. This barrier separates circulating blood from extracellular fluid in the central nervous system. The semipermeable barrier allows for the passage of certain molecules depending on their size, charge, and lipophilicity. Generally, molecules must be small neutral and lipophilic. However, the requirements for each parameter are quite arbitrary; therefore, radiopharmaceuticals that aspire to image the brain must be highly optimized. There are a couple of Tc radiopharmaceuticals that are used clinically to image defects in the brain. ^{99m}Tc -HMPAO, also known as CeretecTM, and ^{99m}Tc -ECD, NeuroliteTM, are agents that detect regional cerebral blood flow changes. Both utilize ^{99m}Tc in the +5 oxidation state and exploit the $^{99m}\text{Tc}=\text{O}^{3+}$ core. The ligands are tetradentate and contain a *n*thiolate-*n*amide ($n=2,4$) complexation site.

One first generation Tc radiopharmaceutical used to image bone infarction and bone diseases is ^{99m}Tc -MDP. Though there are various complexes involving technetium and phosphonates, ^{99m}Tc -MDP is the most noteworthy. The complexation is thought to involve Tc coordinating to a diphosphonate system through the oxygen. There is very little information reported on the structure of Tc-phosphonates with the exception of x-ray crystallography of polymeric $[\text{Tc}(\text{OH})(\text{MDP})]$. In this structure, the Tc is octahedral, and oxygen atoms of the phosphonate bridge the Tc atoms with an additional oxygen bridge from a hydroxy ligand. Despite the discovery of this structural information the oxidation state of the complex is still unknown, though thought to be a +3/+4 mixture.³²

A second-generation Tc radiopharmaceutical used to evaluate kidney function is ^{99m}Tc -Mercaptoacetyltriglycine(Tc-MAG₃). Tc-MAG₃ was developed as an alternative to o-radioiodo-hippurate because radiopharmaceuticals with high tubular secretion were needed for optimal

renal imaging.³³ It was thought that the free carboxylate group would promote more efficient renal clearance. Upon coordination, the Tc=O³⁺ core the three amide nitrogens and the thiolate sulfur are deprotonated producing an anionic complex with a square pyramidal complex, with the Tc-oxo group in the apical position.²⁷

The study of how blood flows through the heart has been a routine procedure in nuclear medicine which began using ²⁰¹Tl-Cl, however due to the relatively long half-life, 3.05 day imaging was not optimal. Thus, several Tc-agents were developed. Commercially known as CardioliteTM, ^{99m}Tc-MIBI, is an FDA approved imaging agent derived from the hexakis isonitrile family of compounds.²⁷ The ligands are coordinated through the carbon on the nitrile group and the Tc has a +1 oxidation state. Myocardial perfusion imaging agents where the Tc is in the +5 oxidation state include, MyoviewTM, a trans-dioxo technetium bisphosphine complex.²⁷ There are two agents that possess a +3 oxidation state: CardiotecTM, ^{99m}Tc-teboroxime cryptate, and Technescan Q12, which is a mixed ligand complex containing Schiff-base bisphosphine.²⁷

1.4. Rhenium Chemistry and ¹⁸⁸Re Radiopharmaceuticals

Rhenium is a third-row transition metal typically used as a surrogate for technetium due to its similar chemistry. There are two naturally occurring isotopes, ¹⁸⁵Re (37.4%) and ¹⁸⁷Re (62.6%), which were discovered by the Noddacks in 1925.³⁴ Rhenium is used as a nonradioactive analog to technetium simply for handling purposes during synthetic and analytical chemistry. It is an ideal candidate found just below technetium on the periodic table and is predicted to have similar physical characteristics, like size and lipophilicity. Due to the

'lanthanide contraction' the two have nearly equivalent ionic radii thus suggesting that they should have complementary bond parameters.

Despite their similarities in practice their differences can have a significant impact. Perrhenate has a considerably higher reduction potential than pertechnetate (-0.361 V versus -0.548 V respectively).²⁶ Generally rhenium complexes are harder to reduce and easier to oxidize which causes difficulties when replicating technetium chemistry. This is especially apparent when working with tracer-level radioactive rhenium.

Currently there are over 30 isotopes of rhenium several of which have characteristics optimal for nuclear medicine, particularly radiotherapy. Radiotherapy gives radiopharmaceuticals a huge advantage by their ability to destroy rapidly growing cells. The isotope ^{186}Re has shown promise for its use as a therapeutic agent (half-life= 90 hrs, β^- max= 1.07 MeV, 5 mm range.). It is produced in a nuclear reactor by the neutron irradiation of ^{185}Re , $^{185}\text{Re}(n,\gamma)^{186}\text{Re}$, and decays to stable osmium. Though production is limited to reactors due to its long half-life ^{186}Re can still be transported and available to isolated sites. SPECT imaging can be performed by exploiting the 136 keV (9%) gamma emission. Presently ^{186}Re is used clinically as a therapeutic agent for the treatment of bone pain, from bone metastases.^{35, 36}

^{188}Re (half-life= 16.9 hrs, β^- max= 2.12 MeV, 11 mm range) is another isotope of interest as a theragnostic agent, that is a radiopharmaceutical with imaging and therapeutic capabilities. The gamma emission, 155 keV (15%), is more applicable than the ^{186}Re isomer, since the emission is more abundant and the energies are similar to $^{99\text{m}}\text{Tc}$. The isotope ^{188}Re is produced

from a $^{188}\text{W}/^{188}\text{Re}$ generator. Currently there are several ^{188}Re radiopharmaceuticals that are in clinical or preclinical trials tabulated below.³⁷

^{188}Re Agent	Application	Institution
^{188}Re -HEDP	Bone Pain Palliation	Bronn and Dresden Germany Montevideo, Uruguay; Szeged, Hungary; Athens, Greece
$^{188}\text{Re}^{\text{V}}$ -DMSA	Bone Pain Palliation	Kent and Canterbury Hospital, Great Britain
^{188}Re -MAG ₃	Endovascular Radiation Therapy	Cedars Sinai Medical Center, Los Angeles; Perth Australia
^{188}Re -Peptides	Tumor Therapy	Preclinical- Bonn, Germany
^{188}Re -Particles	Endoradiation of Tumors- Catheter Administration	Preclinical- Dresden, Germany; Seoul Republic of Korea; Kaichung, Taiwan
^{188}Re -Labelled Antigranulocyte Antibodies	Marrow Ablation Prior to Stem Cell Rescue	Ulm, Germany

Table 3. Current Preclinical and Clinical Trials with ^{188}Re -labelled Agents³⁷

1.5. Ligands, Linkers, Targeting Vectors, Pre-Targeting

Radiopharmaceuticals containing transition metals must use ligands that incorporate the metal into the framework. Ligands often called chelators are organic compounds that house metals through coordination of donor atoms. Ligands are chosen based on their in-situ biological behavior, and are used in the complexation with various radionuclides for imaging and therapy. Peptides are biologically active ligands comprised of amino acids. An advantage for using peptides is that they can mimic or replicate biological functions that naturally occur. Exploiting this advantage allows peptides to serve in two manners; as a biological vehicle where the molecule itself is the targeting vector, and as a bifunctional chelator (BFC). Bifunctional chelators are organic compounds that bind to a radiometal and are conjugated to a targeting vector or biologically active molecule for target specific imaging.

Monoclonal antibodies (mAbs) are targeting vectors that offer highly selective binding and affinity for the recognition of virtually an antigen thus represent essential molecules for diagnostic and therapeutic applications.³⁸⁻⁴⁰ Antibodies generally exhibit slow distribution kinetics, and slow clearance from the body.^{41, 42} The multiday biological half-life of an antibody necessitates the use of radioisotopes with comparable physical half-lives such as ⁸⁹Zr (half-life= 3.2 d) and ¹²⁴I (half-life= 4.2 d), which can lead to high radiation doses to healthy organs ultimately decreasing their desirability for noninvasive imaging of cancer biomarkers.⁴³⁻⁴⁵ Due to the short half-life, ^{99m}Tc is not practical for use in imaging when linked to antibodies, but ^{99m}Tc has been used clinically with antibodies to image cancers and melanomas by using antibody fragments that exhibit short circulation time.⁴⁶

In order to circumvent the long biological half-life of antibodies and the short physical half-life of ^{99m}Tc pretargeting methodologies have been developed. Pretargeted radioimmunoimaging and radioimmunotherapy proceeds by decoupling the monoclonal antibody from the radioisotope and injecting the two components separately, essentially leading to the synthesis of the radioimmunoconjugate at the target tumor site itself.⁴⁷ The radioactive component is generally a small molecule that binds to the tumor site and that which does not bind will be rapidly excreted.^{48, 49} An example is where an antibody is covalently bonded to streptavidin is injected and allowed to bind to the antigen. Once the residual antibody has cleared from the body, a radiometal complexed to biotin is injected and binds to the antibody at the antigen site.²⁷

There have been attempts at *in vivo* pretargeting using a variety of bioorthogonal click ligations. This bioorthogonal reaction does not interfere with the biological system and must form a stable covalent linkage between functional groups at a reasonable rate even when the concentrations are low.^{50, 51} Vugts et al. developed a pretargeting approach based on the Staudinger ligation reaction between an azide-bearing antibody and a phosphine-containing probe labeled with ^{68}Ga , ^{89}Zr , ^{177}Lu , and ^{123}I , however the product could not be observed *in vivo* due to the reactions slow kinetics of the reaction.⁵² Rossin et al. were the first to develop a pretargeting strategy based on the inverse electron demand Diels-Alder (IEDDA) reaction.⁵³ The IEDDA reaction proceeds with a fast rate without the need of a catalyst and displays the remarkably promising results among any other bioorthogonal reaction investigated in tumor pretargeting.^{54, 55} The reaction generally utilizes a trans-cyclooctene (TCO)-labeled antibody

and a tetrazine (Tz)-based radioligand.^{56, 57} The coupling is irreversible, and forms a stable pyridazine product after release of dinitrogen from the reaction intermediate.^{58, 59}

The IEDDA reaction is carried out in 4 steps: (1) the TCO-modified antibody is injected, (2) the modified antibody is given a few days to localize at the tumor site and clear from the blood, (3) a small Tz based radioligand is injected, and (4) an in vivo click reaction between the antibody and radioligand occurs at the tumor site (Figure 8).⁶⁰⁻⁶⁶

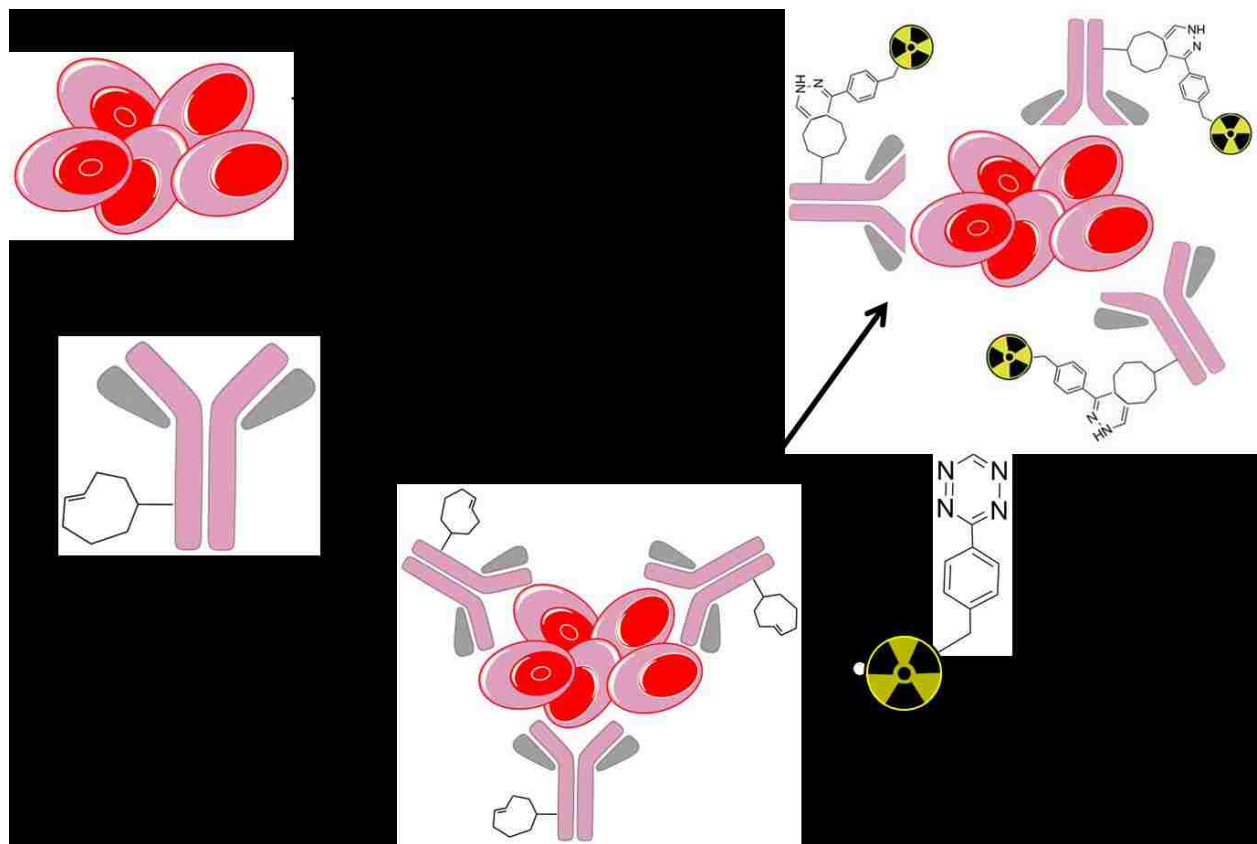


Figure 8. Pretargeted Click Chemistry Approach

The pretargeting approach allows time for the antibody to accumulate at the site of interest, while also clearing from non-target organs, before injection of a radiolabeled coupling partner. The radiolabeled coupling partner reacts selectively with the antibody and that which does not bind rapidly clears.^{67, 68} The pharmacokinetics of small-molecule ligands enables the use of radioisotopes with short half-lives, such as ^{99m}Tc and ^{188}Re , and thus, the pretargeting approach can significantly reduce the radiation dose to nontarget organs. This isotope ^{99m}Tc was selected as an imaging radionuclide because of its exceptional 6.02 hrs half-life and γ -radiation component of 0.140 MeV allowing for SPECT imaging. Similarly, ^{188}Re was selected as an imaging radionuclide because of its 17 hrs half-life and radiation component of 0.155 MeV.⁶⁹

2. Synthesis and Characterization of Re, ^{99m}Tc , and ^{188}Re

Pentapeptides

2.1. Introduction

Advancements in molecular imaging technology have provided opportunities for diagnostic and therapeutic procedures, especially using radiolabeled biological molecules.^{70, 71} Radioactive isotopes of technetium (Tc) and rhenium (Re) have significant medical application because of the nature of their associated radiation and physical half-life properties. Central to molecular imaging is the development of imaging probes.⁷¹⁻⁷³ The isotope ^{99m}Tc , a pure γ -emitter, is a major imaging agent used in over 80% of nuclear imaging.⁷⁴ It has excellent physical properties (γ ray= 142 keV, half-life= 6.02 hrs) and is readily obtained from a ^{99}Mo \rightarrow ^{99m}Tc generator in its pertechnetate form. The low γ ray energy allows for optimal imaging with current gamma camera technology, and its short half-life insures that the radiopharmaceutical can be injected with minimal radiation burden to the patient.^{75, 76} Rhenium, the third-row transition metal congener of Tc, exhibits similar complexation chemistry to technetium, therefore is often used as a surrogate for characterization of ^{99m}Tc radiopharmaceuticals. The isotope ^{188}Re has excellent properties as a potential radiotherapeutic isotope. It has a half-life of 16 hrs, emits a high-energy β^- ($E_{\text{max}}= 2.11$ MeV) that is effective for cell killing, and also generates an imageable γ ray of 155 keV that can be used to track the radiotherapeutic agent.⁷⁷⁻⁷⁹

Short peptide sequences labeled with ^{99m}Tc and ^{188}Re have attracted interest in the development of target-specific radiopharmaceuticals.^{80, 81} Radiolabeled peptides are valuable biological tools for tumor imaging and targeted radionuclide therapy because of their favorable pharmacokinetics and specific tumor targeting characteristics. Due to their small size, peptides generally exhibit rapid pharmacokinetics and are able to penetrate tumors very efficiently.^{82, 83} They also exhibit faster blood clearance and lower kidney retention. One can molecularly engineer peptides to exhibit desired pharmacokinetic characteristics by changing the peptide sequence during solid-phase synthesis or by grafting additional elements such as polyethylene glycol (PEG) linkers to the chelate region. The coordination chemistry of the metal will determine the geometry and stability of the radiopeptide complex in vivo.²⁴

Technetium and rhenium are group VIIB transition metals that share similar coordination geometries and form stable peptide complexes with amine and amide nitrogens, carboxylate oxygens, and thiolate sulfurs.^{23, 84} In this work structures of ^{99m}Tc , ^{188}Re , and Re complexes are investigated focusing on the KYCAR (lysyl-tyrosyl-cystyl-alanyl-arginine) peptide sequence. Chelation about the radiometal is N_3S , includes three nitrogens (one amine of Lys side chain, two amide nitrogens of Tyr and Cys) and one sulfur (the thiol sulfur of Cys) (Figure 9).

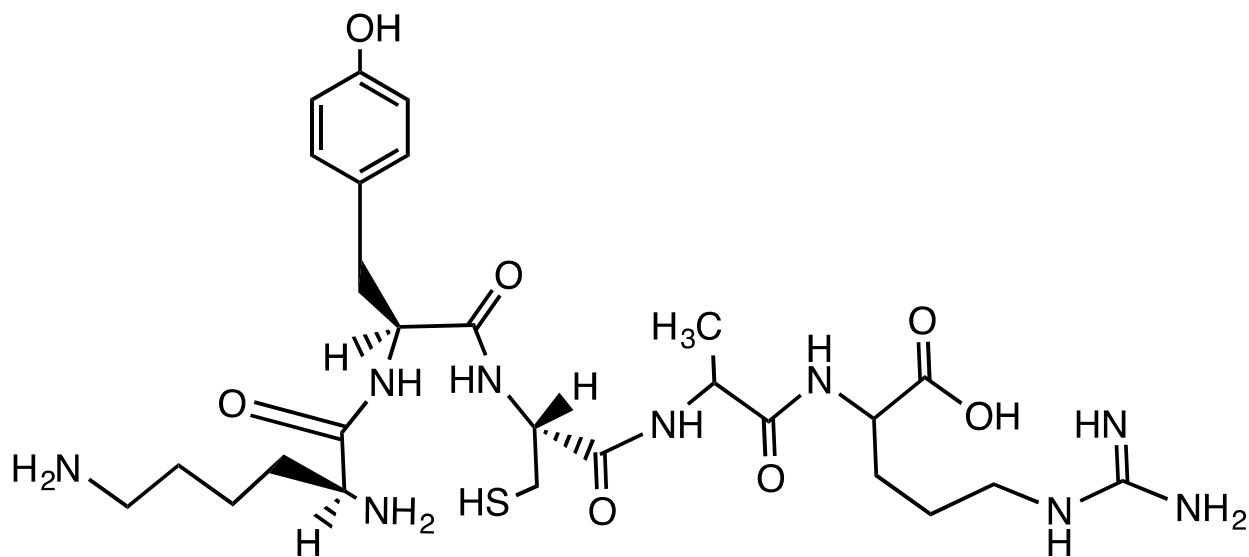


Figure 9. KYCAR Ligand

The thiol group has a high affinity for transition metals, a property convenient for labeling cysteine-based proteins with ^{99m}Tc or ^{188}Re .^{23, 85, 86} When peptide-based chelators are comprised of amino acids containing side chains, chiral centers are incorporated into the coordination plane, and diastereomeric complexes are known to form where the $\text{M}=\text{O}$ group ($\text{M} = \text{Tc}, \text{Re}$) is either syn or anti to the substituents.^{87, 88} In this work, it was found that two main products are formed when KYCAR is radiolabeled with rhenium, and these are purported to be the syn and anti diastereomers of $[\text{ReO}]\text{KYCAR}$. The two diastereomers are referred to as syn or anti with regard to the position of the side chain of Tyr relative to the $\text{M}=\text{O}$ bond (Figure 10).

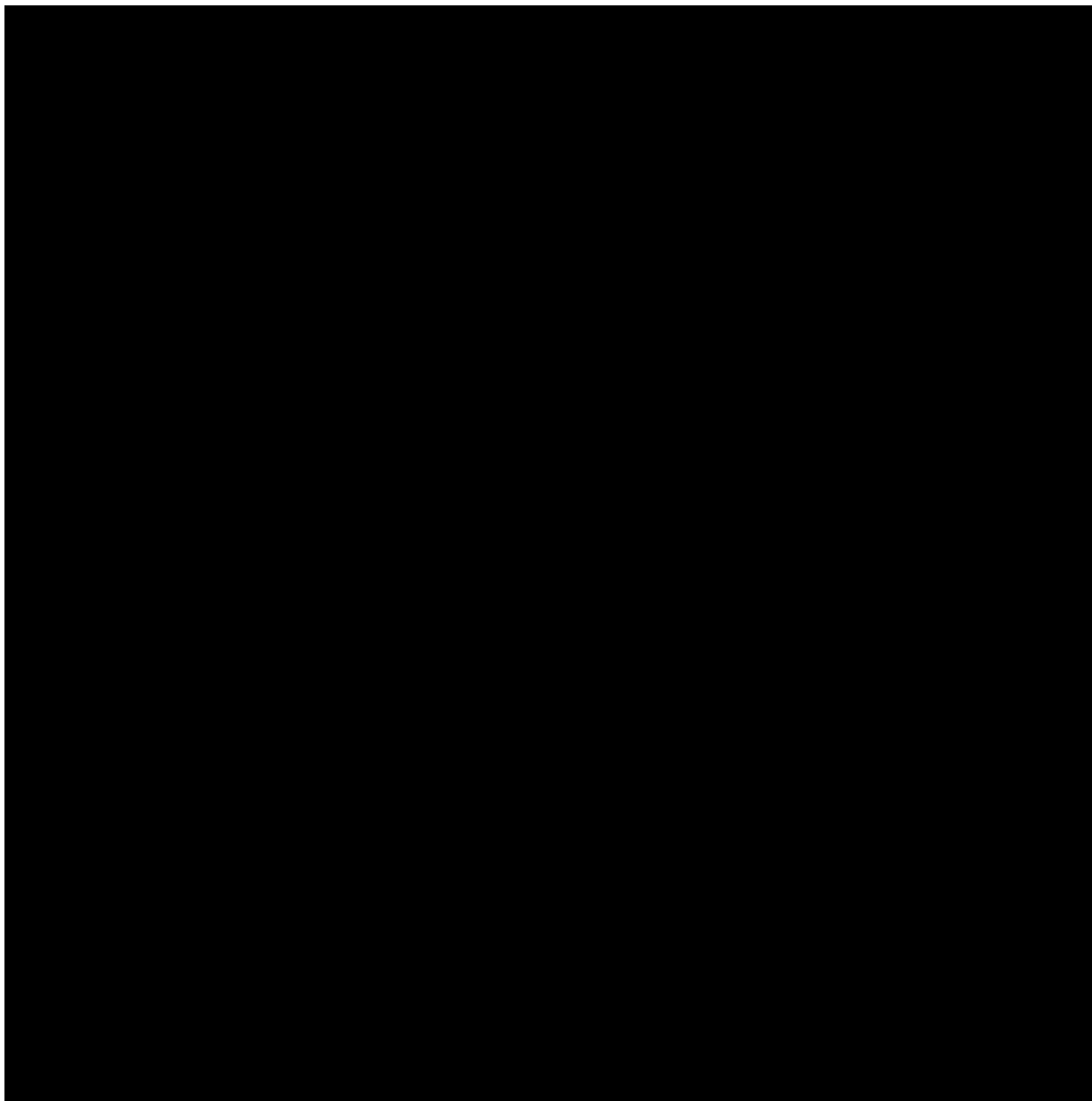


Figure 10. Anti and Syn Diastereomers of ReO-KYCAR

Although stereoisomers of radiopharmaceutical products often have different biodistribution behaviors⁸⁹⁻⁹², it was found that working on the tracer level with the ^{99m}Tc and ¹⁸⁸Re

radionuclides renders it difficult to observe the anti peak, therefore only the syn product was evaluated to understand its biological behavior and stability.

The overall goals of this project were (1) to synthesize the Tc/Re pentapeptide complexes, (2) to identify spectroscopic methods for characterization of syn versus anti rhenium peptide complexes, (3) to analyze the ex vivo stability, and (4) to assess the biological properties of the [^{99m}TcO]KYCAR and [^{188}Re]KYCAR complex in vivo. Details on this effort are provided below.

2.2. Materials

^{99m}Tc was obtained via Memorial Sloan Kettering Cancer Center, New York, New York, as $\text{Na}^{99m}\text{TcO}_4$, eluted from a $^{99}\text{Mo}/^{99m}\text{Tc}$ Generator. The isotope ^{188}Re was obtained as $\text{Na}^{188}\text{ReO}_4$ was eluted from an $^{188}\text{W}/^{188}\text{Re}$ generator with saline (0.9% NaCl solution). The $^{188}\text{W}/^{188}\text{Re}$ generator was purchased from RadioMedix, Houston, Texas, USA. Activity measurements were obtained from an Atomic Products Corporation Atomlab 100 Dose Calibrator. The ligand, KYCAR, was purchased from United Peptide, Herndon, Virginia, USA. Methanol (MeOH), dimethyl sulfoxide (DMSO), HPLC-grade acetonitrile, trifluoroacetic acid (TFA), and 0.9% NaCl solution were purchased from Fisher Scientific. Tin (II) tartrate 99%, tin (II) chloride dehydrate, and d- gluconic acid was purchased from Sigma Aldrich. Deionized water was obtained from a 0.22 μm Millipore filtration system. All *in vivo* experiments were performed according to protocols approved by the Memorial Sloan-Kettering Institutional Animal Care and Use Committee.

2.3. Syntheses

2.3.1. $(\text{Bu}_4\text{N})[\text{ReOBr}_4(\text{H}_2\text{O})]\cdot\text{H}_2\text{O}$

This rhenium starting material was prepared following the method of Rose et. al.⁹³ Briefly 14.05 mmol of n-butylphosphine, PBU_3 , was dissolved in 20 ml CH_2Cl_2 . 14.20 mmol Br_2 was also dissolved in 20 mL CH_2Cl_2 and added to the above butylphosphine solution dropwise. 4.06 mmol $(\text{Bu}_4\text{N})\text{ReO}_4$ was dissolved in 20 mL CH_2Cl_2 , to that the butylphosphine solution was added and the resulting solution was allowed to stir for 45 minutes. 3 mL cyclohexene, 100 mL

diethyl ether, 100 mL pentane was added sequentially. The purple product was collected via vacuum filtration, was washed with diethyl ether and allowed to air dry (2.67 g, 3.26 mmol, 86%). IR (ATR, cm^{-1}) 2959 (s), 2932 (m), 2873 (m), 1466 (s), 1380 (w), 1227 (w), 1103 (vs), 984 (vs), 903 (vs), 812 (w), 736 (m).

2.3.2. ReO-KYCAR

The KYCAR ligand (0.0403 mmol) was dissolved in 500 μL CH_3OH . The above synthesized $(\text{Bu}_4\text{N})[\text{ReOBr}_4(\text{H}_2\text{O})]\cdot\text{H}_2\text{O}$ (0.0403 mmol) was dissolved in 500 μL CH_3OH and added dropwise to the ligand. The resulting reddish brown solution was allowed to stir with a stir bar at 200 rpm for 10 minutes. Following stirring the solution was allowed to sit at room temperature for 30 minutes. The ReO-KYCAR product was analyzed and purified via HPLC with a yield of 40%.

2.3.3. ReO-KYC

The KYC ligand (0.0403 mmol) was dissolved in 500 μL CH_3OH . The above synthesized $(\text{Bu}_4\text{N})[\text{ReOBr}_4(\text{H}_2\text{O})]\cdot\text{H}_2\text{O}$ (0.0403 mmol) was dissolved in 500 μL CH_3OH and added dropwise to the ligand. The resulting reddish brown solution was allowed to stir with a stir bar at 200 rpm for 10 minutes. Following stirring the solution was allowed to sit at room temperature for 40 minutes. The ReO-KYC product was analyzed and purified via HPLC.

2.3.4. $^{99\text{m}}\text{TcO}$ -KYCAR

To a saline solution of $^{99\text{m}}\text{Tc}$ pertechnetate, KYCAR ligand (200 μL , 0.00234 mmol solution) in saline was added. To that mixture tin(II) tartrate (40 μL , 0.0221 mmol solution) in water was added and vortexed. The reaction mixture was then kept at 90° C for 10 minutes

followed by sitting at room temperature for 30 minutes. The solution was then filtered through a 0.1 μm syringe filter and analyzed or purified via HPLC. Radiochemical Purity 99.9%.

2.3.5. $^{188}\text{ReO-KYCAR}$

To a saline solution of ^{188}Re perrhenate solution, tin (II) chloride (75 μL , 0.105 mmol solution) in water and d-gluconic acid (150 μL , 0.102 mmol solution) in water were added. The reaction mixture was vortexed and kept at 37° C for 30 minutes. To this solution the KYCAR ligand (200 μL , 0.00313 mmol solution) in saline was added, the reaction mixture was vortexed and kept at 37° C for 30 minutes. The solution was then filtered through a 0.1 μm syringe filter and analyzed or purified via HPLC. Radiochemical Purity 99.9%.

2.4. HPLC Analyses

Complexes were analyzed using a Waters Symmetry C_{18} 3.5 μm 100 Å analytical column 4.6 x 150 mm. Complexes were purified using a semi-preparative Waters Nova Pak HR C_{18} 6 μm 60 Å column 19 x 300 mm. All non-radioactive Re “cold” HPLC experiments were conducted on a Rainin HPXL solvent delivery system. Radioactive $^{99\text{m}}\text{Tc}$, ^{188}Re “hot” HPLC experiments were completed using a Varian Pro Star HPLC system. The radioactive complexes were analyzed and purified using a Waters Atlantis dc18 3 μm 100 Å column 4.6 x 150 mm. The γ emissions were monitored using a Bicon 2m2/2 NaI detector and Tennelec Minibin components. The software used for all HPLC systems was the ProStar WorkStation. The solvents used were ultra-pure deionized water with 0.1% trifluoroacetic acid (solvent A), and HPLC-grade acetonitrile with 0.1% trifluoroacetic acid (solvent B). Method 1 describes the mobile phase gradient for cold

HPLC experiments. Method 1: 5-25% B over 26 minutes. Method 2 describes the mobile phase gradient for hot HPLC experiments. Method 2: 5-25% B over 20 minutes. The flow rate for analytical analyses was 1 mL/minute, and for semi-preparative separations 16.69 mL/minute. For all HPLC analyses the UV detection was monitored at 280 nm.

For complexes containing stable rhenium the solvent was blown off using N₂ for about 4 hours. The dry complex was then reconstituted in a 95%/5% (solvent A/ solvent B) mixture of the mobile phase for HPLC analysis. For complexes containing radioactive metal cores the complexes were analyzed upon completion of the syntheses in saline solution.

2.5. Mass Spectrometry Analysis

For cold rhenium compounds, mass spectral data were obtained on a LCMS system comprised of an Agilent 1200 LC system coupled to an Agilent 6340 ion trap mass spectrometer. Samples were injected onto an Agilent Zorbax column (SB-C8, 5 μ M, 2.1 x 50 mm) using a linear gradient of 5-95% acetonitrile in water (0.5% formic acid) over 10 minutes. The samples were prepared by dissolving the lyophilized ReO-KYCAR samples in water:acetonitrile solution (v:v, 450:50 μ L).

2.6. NMR Analysis

The 1D proton and 2D TOCSY (total correlation spectroscopy) NMR spectra were obtained from a Bruker Avance III 600 MHz with a TCI cryoprobe NMR spectrometer with chemical shift referenced to H₂O, at $T=296$ K. ReO-KYCAR samples (peak 1, anti, and peak 2, syn) (5-10 mg) was dissolved in an 800 μ L solution of 0.01 M HCl/D₂O 50:50 (v:v). The solution

was then transferred to a 5 mm U-Thin NMR tube. 1D proton NMR spectra were collected at 8 scans. 2D COSY scans were collected at 2 scans, 256 increments.

Techniques used for the titration studies are described by Cantorias et. al.⁸⁸ Briefly 10 mg of the cold rhenium complex was dissolved in 700 μ L 0.01 M DCl in D₂O. The pH was recorded, the solution was transferred to a 5 mm U-Thin NMR tube, and 1D proton and 2D COSY (correlation spectroscopy) NMR spectra were obtained. The sample was then titrated with 0.05 M NaOD until the pH changed from 0.5 to 1 intervals. The volume and pH was recorded, and NMR spectra were obtained.

2.7. Infrared Spectroscopy

Infrared spectra were obtained using a Perkin-Elmer Spectrum Two IR Spectrometer with attached UATR in the range of 500-4000 nm. Briefly a small amount of lyophilized sample was placed on the UATR and the appropriate pressure was applied.

2.8. Circular Dichroism Analysis

Circular Dichroism spectra were collected on an Aviv Biomedical Circular Dichroism spectrometer of approximately 1 nanomol solutions of Re-KYCAR in 1 mL methanol. The samples were scanned from 200 to 680 nm. The samples analyzed were peak 1 and peak 2 from the HPLC prep purification

2.9. Crystallization

Several different techniques were attempted to grow crystals of ReO-KYCAR. For each technique, the polar solvents used were as followed; H₂O, MeOH, EtOH, acetonitrile, ethylene glycol, or ethyl acetate. The nonpolar solvents used were; toluene, pentane, diethyl ether or dichloromethane. Technique 1: solvent evaporation. A 2 mg lyophilized sample was dissolved in a 3 mL vial with a minimal amount of polar solvent. A few drops of nonpolar solvent were added to the solution and the solution was allowed to sit at room temperature and monitored over time. Technique 2: vapor diffusion. A 2 mg lyophilized sample was dissolved in in a 3 mL vial with minimal amount of polar solvent and covered with perforated parafilm. The 3 mL vial was then placed into a 20 mL scintillation vial filled with 3 mL of the non-polar solvent. The solvent chamber was then allowed to stand at 4° C and monitored over time. Technique 3: purification recrystallization. A 2 mg of lyophilized sample was dissolved in minimal MeOH and precipitated with diethyl ether. The solution was centrifuged and the resulting pellet was dissolved in a minimal amount of polar solvent. A few drops of nonpolar solvent were added to the solution and the solution was allowed to sit at room temperature and monitored over time.

Crystals of ReO-KYC were obtained by supersaturation in methanol over 1 week at room temperature.

2.10. X-ray Structure Determination

X-ray diffraction data were collected on a Bruker X8 Kappa Apex II diffractometer. The structure was solved using direct methods and standard difference map techniques, and was refined by a full-matrix least-squares procedures on F^2 with SHELXTL (version 2014/7)

2.11. LogD Studies

To determine the extinction coefficients the radioactive metal (^{99m}Tc , ^{188}Re) complexes dried via high vacuum system following synthesis. The product was reconstituted in PBS and placed into a micro centrifuge tube with an equal amount of 1 octanol. The samples were vortexed followed by centrifugation at 10,000 rpm for 5 minutes.

2.12. Biodistribution Studies

The ^{99m}Tc and ^{188}Re labelled KYCAR complexes were evaluated for their biological distribution in healthy athymic nude female mice 6-8 weeks old. About 100 μCi to 200 μCi (3.7×10^3 - 7.4×10^3 kBq) of the radiolabeled complex was injected intravenously into the mice via the tail vein. Mice were sacrificed 30 minutes, 1 hour, 2 hour, and 4 hour post injection; 5 mice per time point. The following tissues were collected; blood, heart, lungs, liver, spleen, stomach, small intestines, large intestines, kidneys, muscle, bone, skin, thyroid, and gall bladder. The tissues were then counted on a Perkin Elmer Automatic Wizard γ -counter and the percent injected dose per gram (%ID/g) were calculated and reported. The %ID/g is the amount of activity found in a specific tissue divided by the total amount of activity injected multiplied by 100.

2.13. Results and Discussion

2.13.1. Synthesis and Isolation of ^{99m}Tc , ^{188}Re , and Re KYCAR Complexes

2.13.1.1. Kinetic studies

The reaction of $\text{Re}^{\text{V}}\text{OBr}_4^-$ with the KYCAR pentapeptide in methanol resulted in two major $[\text{Re}^{\text{V}}\text{O}]$ complexes. Rhenium contains a closed-shell d^2 electronic configuration that readily accepts π electron density during reactions with deprotonated amides and thiol groups from peptide ligands. The reversed phase HPLC data in figure 11 shows the kinetics of the reaction over a period of 10 days. The reversed phase HPLC data shows 3 peaks present immediately post synthesis, denoted peak A, B, and C. Peak A is classified as the intermediate peak, as it disappears over time. Peak B and C are the two major peaks. Peak B began to convert into peak C so that after 1 day; these peaks were formed in an approximately 2.1:1 ratio. After 3 days, the ratio was approximately 1:1. The two major complexes reached equilibrium 7 days post synthesis, where peak C was the dominant peak at a ratio of approximately 0.8:1. It is postulated that the two major peaks represent diastereomers, syn and anti, based on previous work in the literature.^{31, 88} This is further examined and confirmed, *vide infra*.

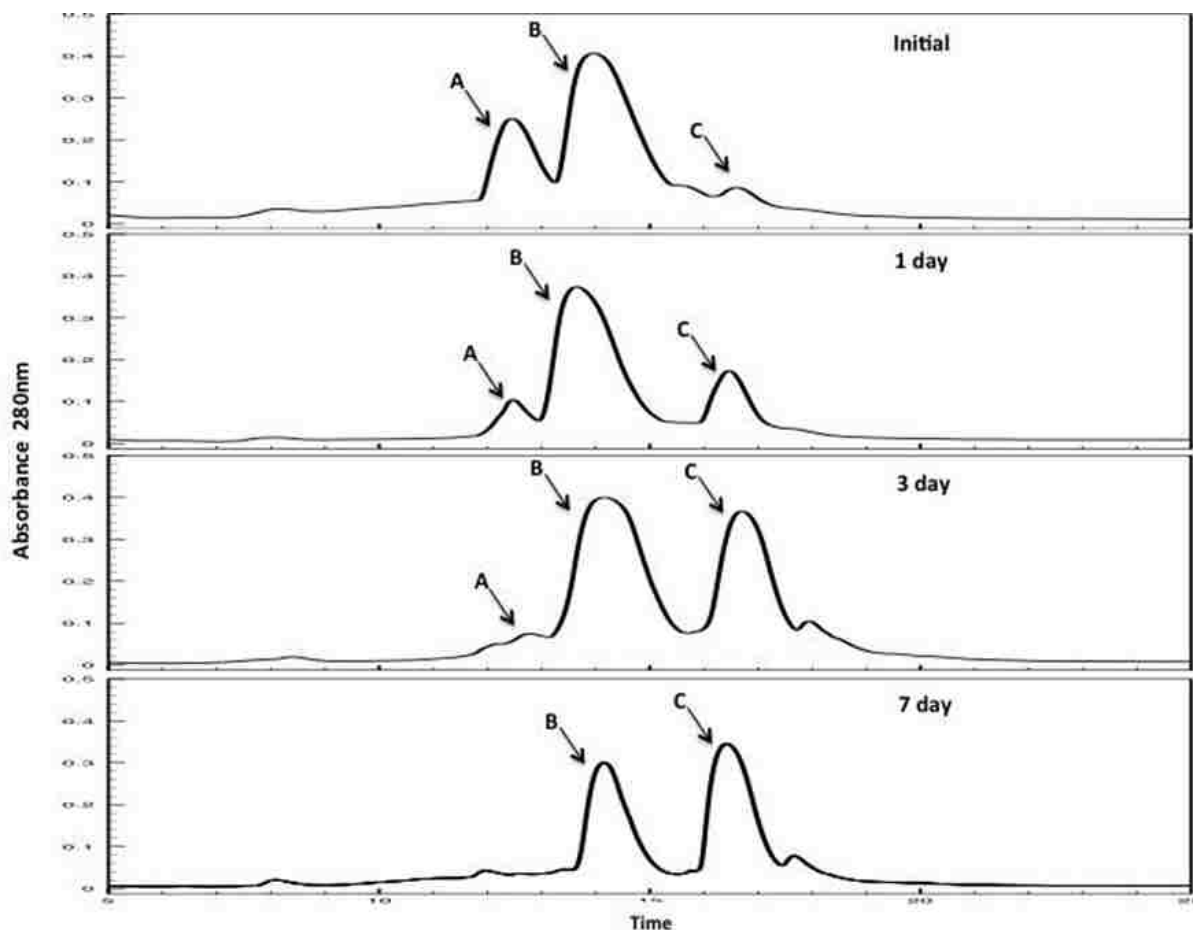


Figure 11. Kinetic study of ReO-KYCAR over 10 day period. Immediately post synthesis there are three peak present (A,B,C). Peak A (intermediate peak) converts to peak B (peak 1), which converts to peak C (peak 2).

To further characterize all species formed, peaks A, B, and C were collected separately after 1 day via Method 1 and lyophilized to powders. After lyophilization, the powders from both the peak A and B products exhibited a peach color, whereas the powder from peak C was darker, exhibiting a pinkish/peach color. Initially, we hypothesized that peaks B and C were diastereomers, however that was not consistent with mass spectral data. Peak B revealed a

molecular ion $[M + H]^+$ peak at m/z 840, which is consistent with the exact mass of the $[Re^V O]KYCAR$ complex (mass= 839.24 g/mol) (Figure 12).

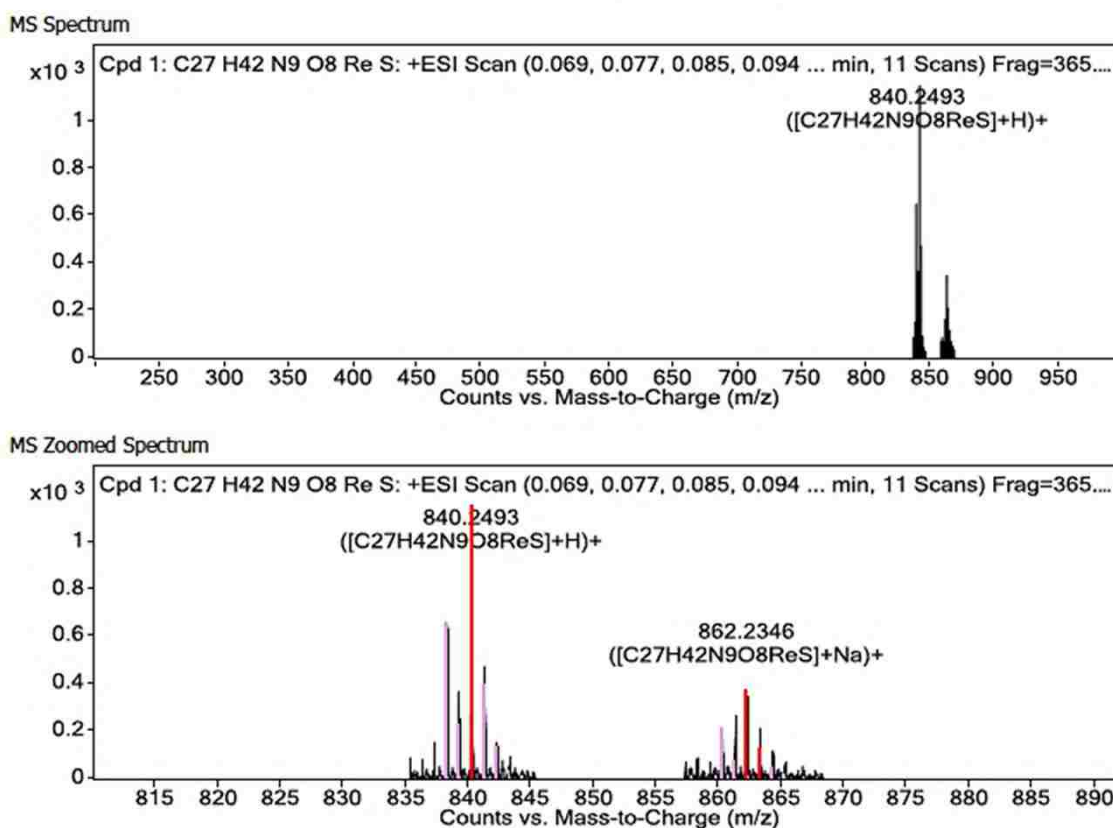


Figure 12. Mass spectroscopy of ReO-KYCAR peak B molecular ion $[M + H]^+$ peak at m/z 840 which corresponds to an exact mass of 839.24 g/mol.

Peak C, however, revealed a molecular ion $[M + H]^+$ peak at m/z 854, which is 14 dalton above the exact mass of ReO-KYCAR. Peak A contained a mixture of the peaks at m/z 840 and 854.

Knowing the reactivity of our peptide, specifically at the carboxyl terminus on the arginine, it was theorized that an acid-catalyzed esterification between methanol and the carboxylic acid occurred rapidly after synthesis, resulting in a methyl ester adduct (+14 adduct) (Figure 13, 14).

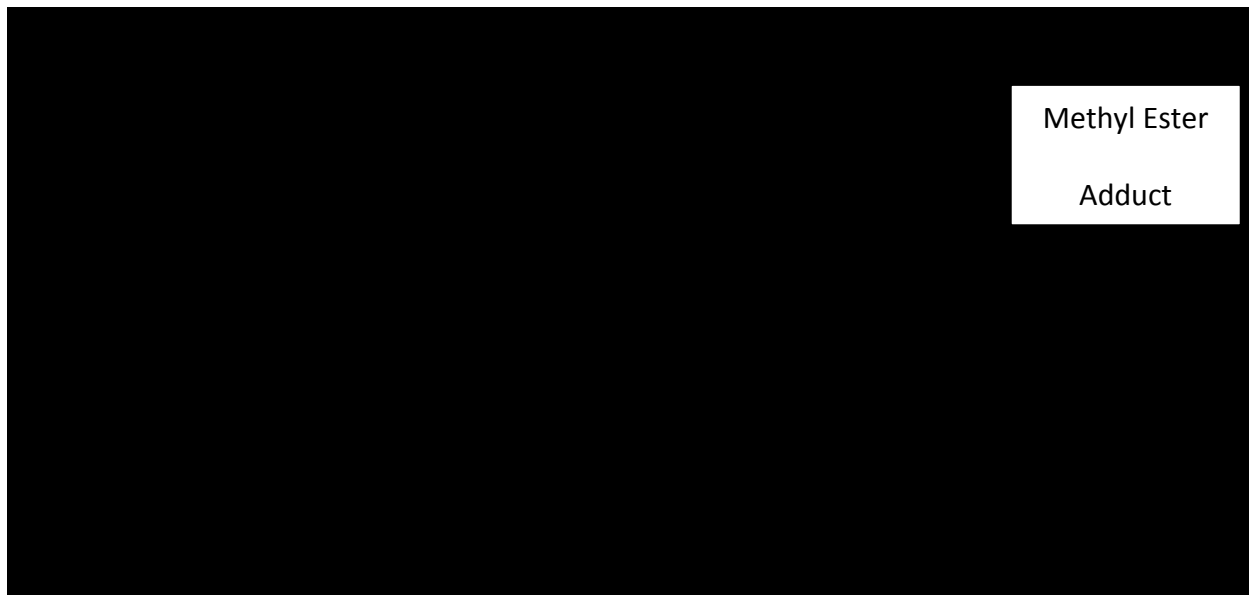


Figure 13. Structure of ReO-KYCAR + Methyl Ester Adduct

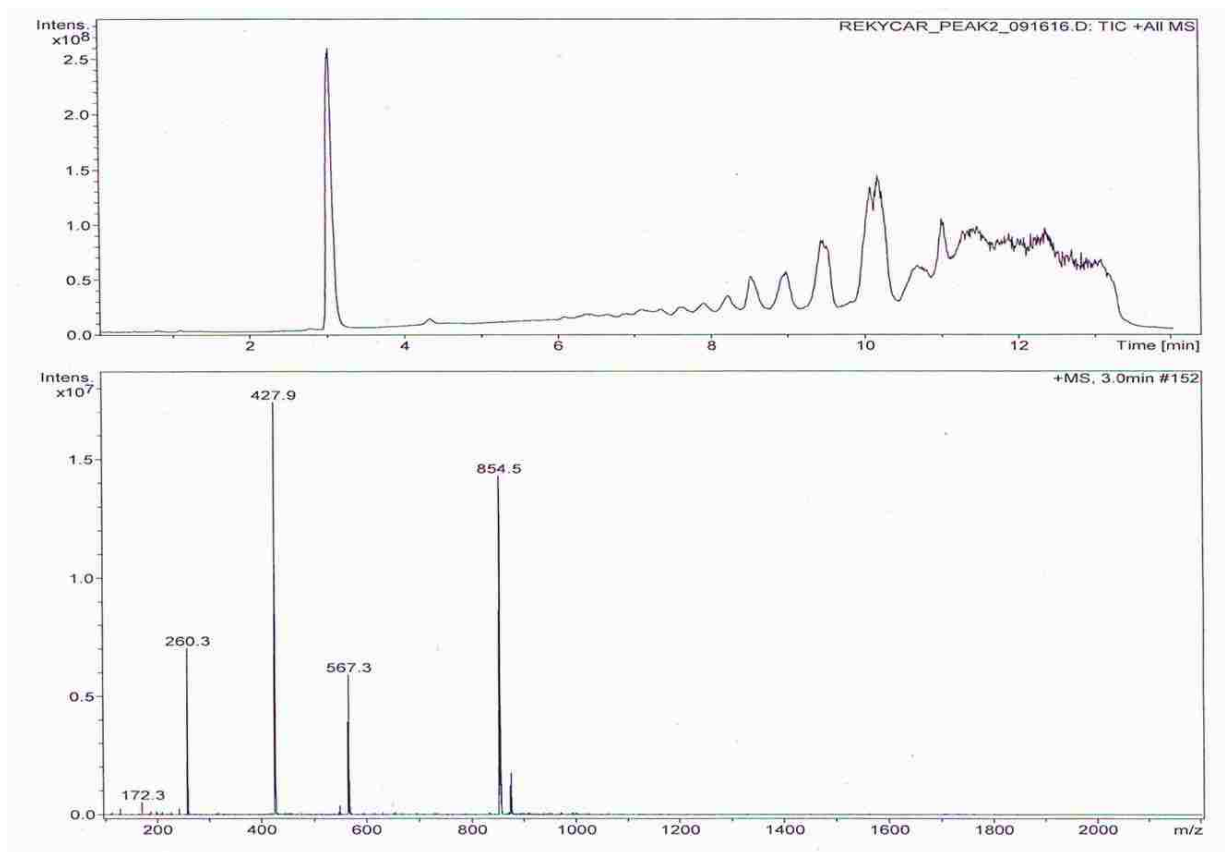


Figure 14. Mass Spectroscopy of ReO-KYCAR + Methyl Ester Adduct

To observe whether peak C could be isolated at m/z 840, it was collected 2 hours post synthesis via HPLC and lyophilized. The mass spectral data revealed a 1:2 ratio of m/z 840:854, revealing its rapid conversion to the adduct peak C.

To test whether methanol promotes this esterification, the reaction was performed in acetonitrile. Following the same synthetic procedure, KYCAR was dissolved in 500 μ L acetonitrile and $(\text{Bu}_4\text{N})[\text{ReOBr}_4(\text{H}_2\text{O})]\cdot\text{H}_2\text{O}$ with 5 drops of deionized water to ensure complete

dissolution. After allowing the reaction to sit for 1 day 100 μ L of the reaction solution was injected onto the HPLC via Method 1 (Figure 15).

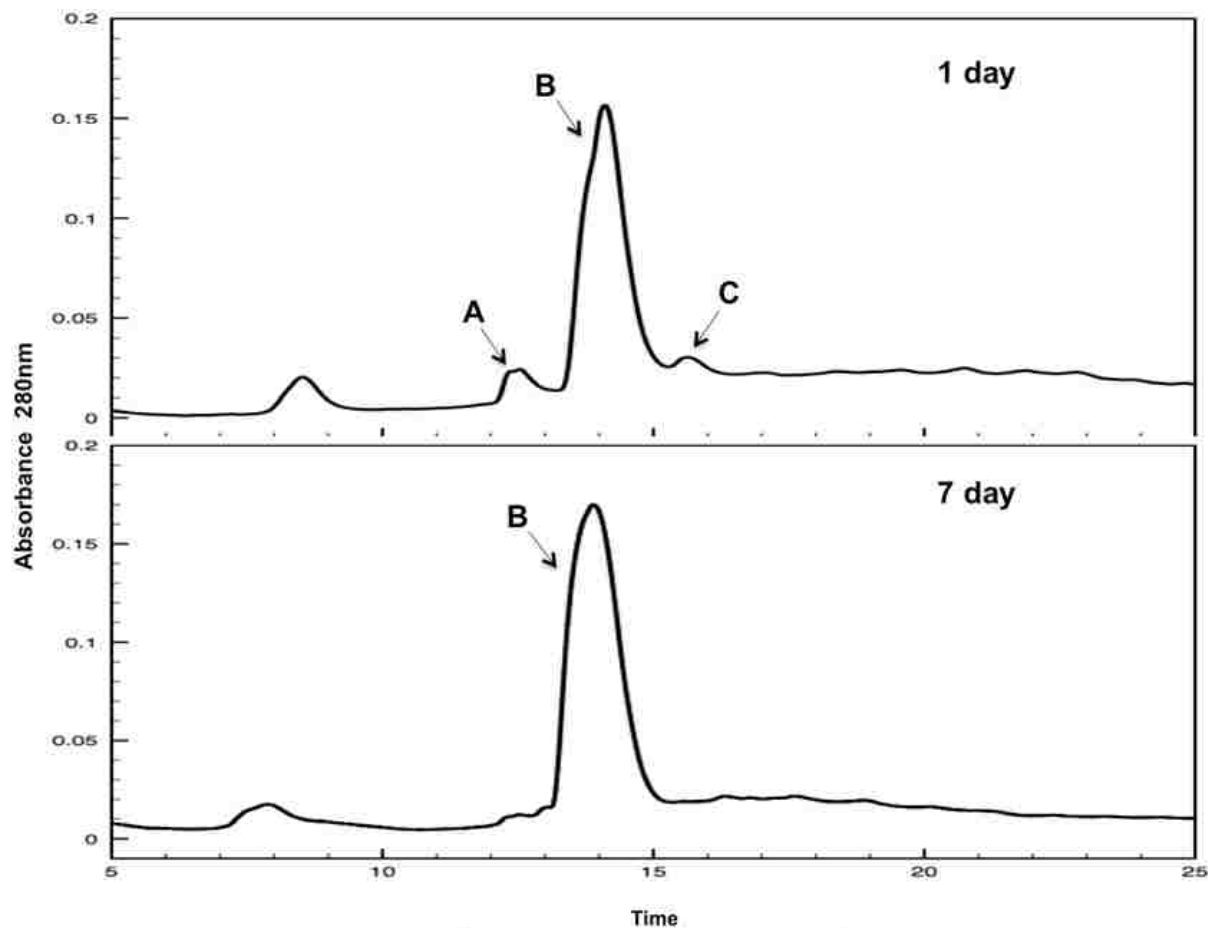


Figure 15. Kinetic study ReO-KYCAR in acetonitrile. Initially reveals three peaks (A, B, and C). Shows that peak B does not interconvert to peak C

After collecting and lyophilizing peaks B and C at day one, mass spectral data were obtained. Peak B retained the same m/z at 840. More importantly, peak C displayed a signal at m/z 840, with no additional mass at m/z 854, thus contributing to our hypothesis that methanol reacted with our metal-peptide complex. A kinetic study of the $[\text{Re}^{\text{V}}\text{O}]\text{KYCAR}$ dissolved in acetonitrile (Figure 15) reveals that peak B does not interconvert into peak C. One possible explanation for this may be that the use of organic solvents minimizes the interconversion of diastereomeric species.

2.13.1.2. $^{99\text{m}}\text{Tc}$ and ^{188}Re HPLC

The reaction of the KYCAR ligand with $^{99\text{m}}\text{TcO}_4^-$ reduced with tin(II) tartrate results in one major complex. Figure 16 shows the immediate post synthesis reverse phase HPLC trace. It is hypothesized that this single species occurs due to the extended heating/ reaction time during the synthesis. Instant thin layer chromatography shows that the purity post HPLC purification is 99.9%.

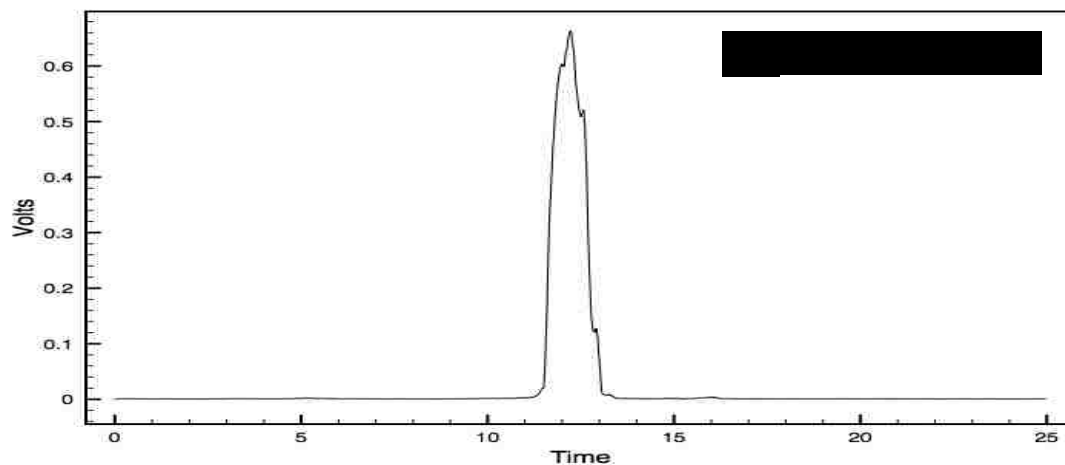


Figure 16. HPLC Trace $^{99m}\text{TcO-KYCAR}$.

The purified $^{99m}\text{TcO-KYCAR}$ was then coeluted with the macroscopic ReO-KYCAR lyophilized peak1 (anti) and is shown in figure 17. This shows the macroscopic rhenium complex eluting between 9 and 12 minutes and the tracer technetium complex eluting between 10 and 12.5 minutes. Due to the location and sequence of the UV and radio detectors in this HPLC system UV active species should elute 30 second to 1 minute before radio detection. We note that the shoulder appears in the radiotrace at 10 minutes, this co-elutes with the ReO-KYCAR and is assigned to the “anti” ^{99m}Tc diastereomer. The majority of the $^{99m}\text{TcO-KYCAR}$ is assigned to the “syn” diastereomer. The first radiotrace peak (anti diastereomer) likely occurs due to the orders of magnitude of macroscopic, carrier ReO-KYCAR .

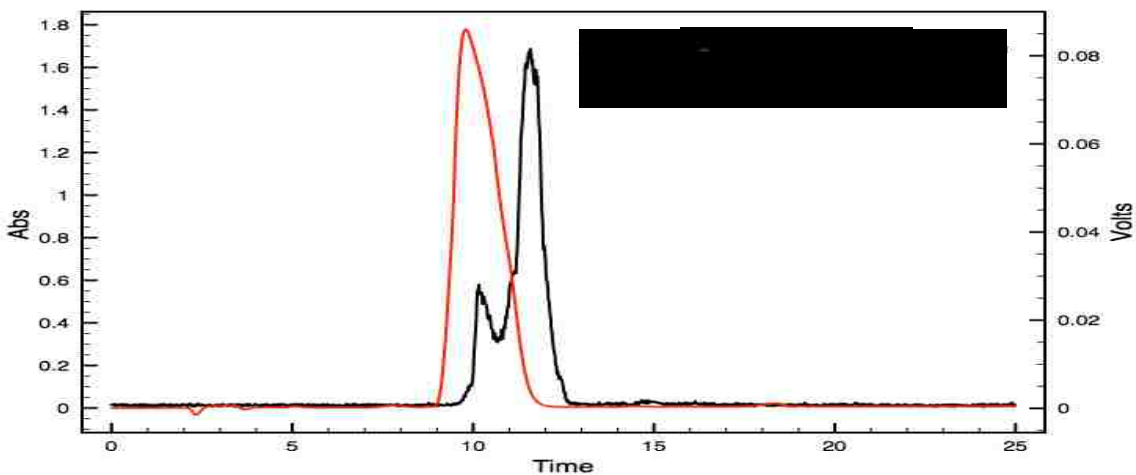


Figure 17. Coelution of $^{99m}\text{TcO-KYCAR}$ with ReO-KYCAR Peak 1(anti)

The reaction of $^{188}\text{ReO}_4^-$ reduced with tin (II) chloride with the KYCAR ligand in the presence of *d*-gluconic acid as an exchange ligand also results in major complex. Figure 18 shows the immediate post synthesis reverse phase HPLC trace. Instant thin layer chromatography demonstrates that the purity post HPLC purification is 99.9%.

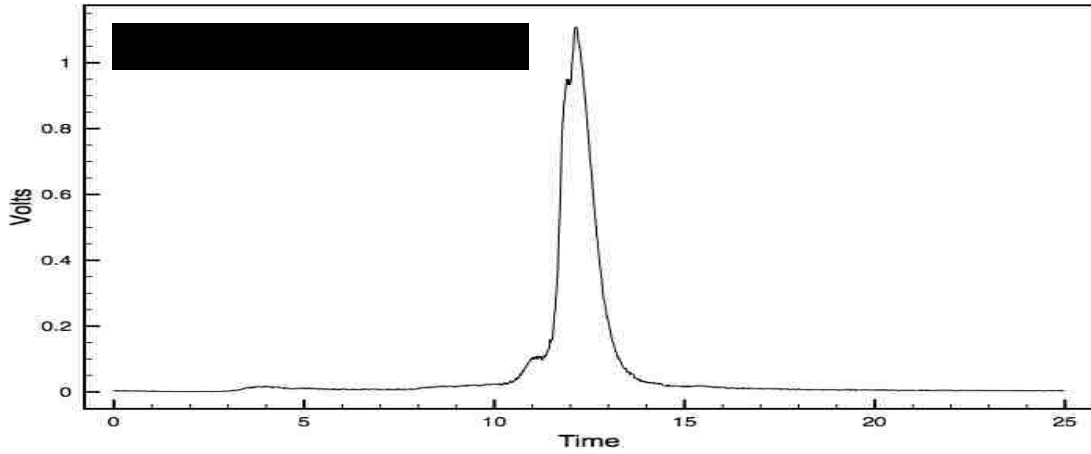


Figure 18. HPLC Trace of $^{188}\text{ReO-KYCAR}$

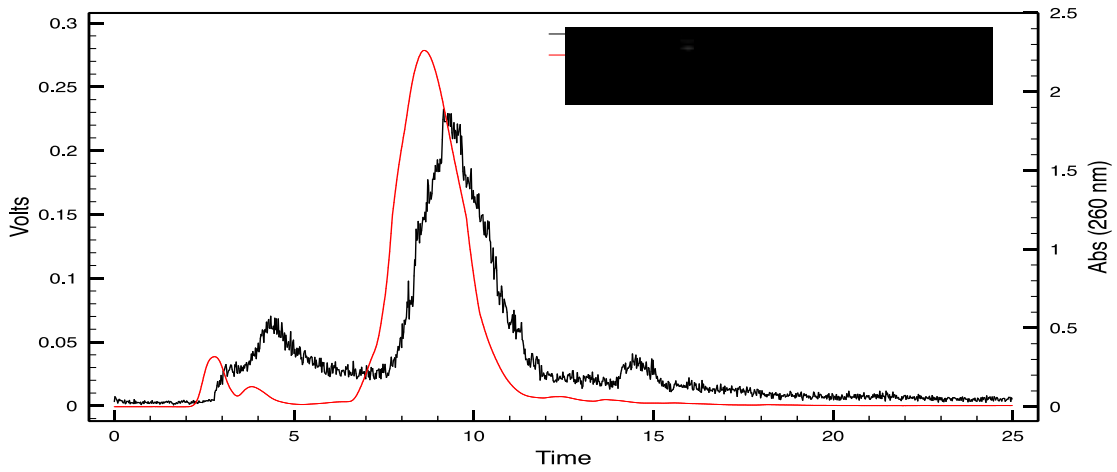


Figure 19. Coelution of $^{188}\text{ReO-KYCAR}$ with ReO-KYCAR

The purified $^{188}\text{ReO-KYCAR}$ was then coeluted with the macroscopic ReO-KYCAR lyophilized peak1 (anti) and is shown in Figure 19. This shows the macroscopic rhenium complex eluting between 7 and 11 minutes and the tracer rhenium complex eluting between 8 and 12 minutes. Due to the location and sequence of the UV and radio detectors in this HPLC system the UV active species should elute 30 second to 1 minute before radio detection. Therefore, it is observed that the two complexes are chemically identical. The ^{188}Re is less stable than its $^{99\text{m}}\text{Tc}$ congener, which is observed by the slight decomposition to $^{188}\text{ReO}_4^-$. There appears to be small amounts of other decomposition products as seen by the radiopeak at 4.5 minutes and 145 minutes.

2.13.2. Spectroscopic Characteristics

2.13.2.1. NMR

The chemical shifts from the ^1H NMR spectra of the macroscopic ReO-KYCAR diastereomers (Table 4) were compared to the free KYCAR ligand. This allows assignment of the protons of the diastereomers (Figure 20). For reference Figure 21 labels the amino acids within the ligand by its 1-letter code.

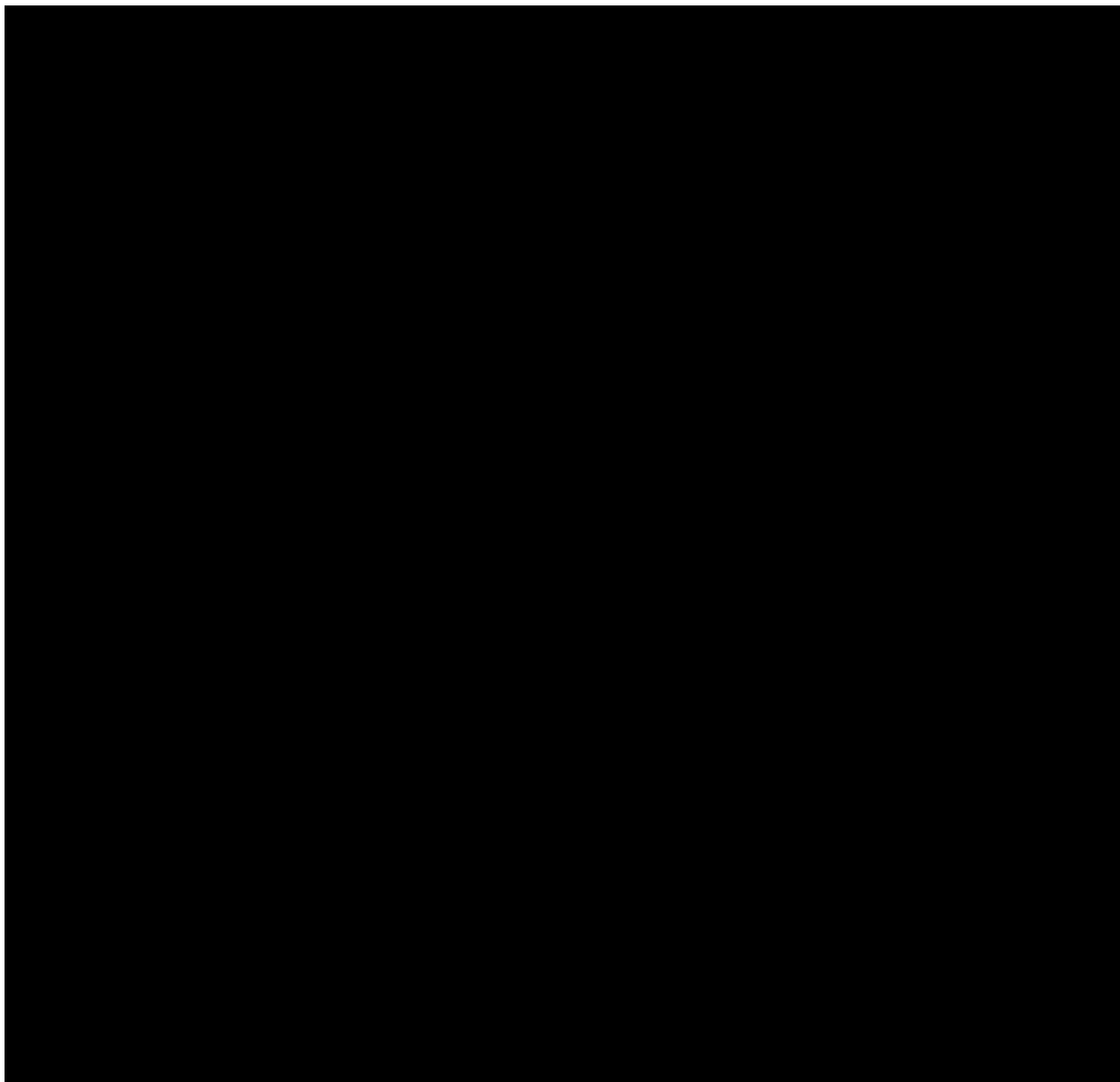


Figure 20. Structures of ReO-KYCAR diastereomers (Anti and Syn)

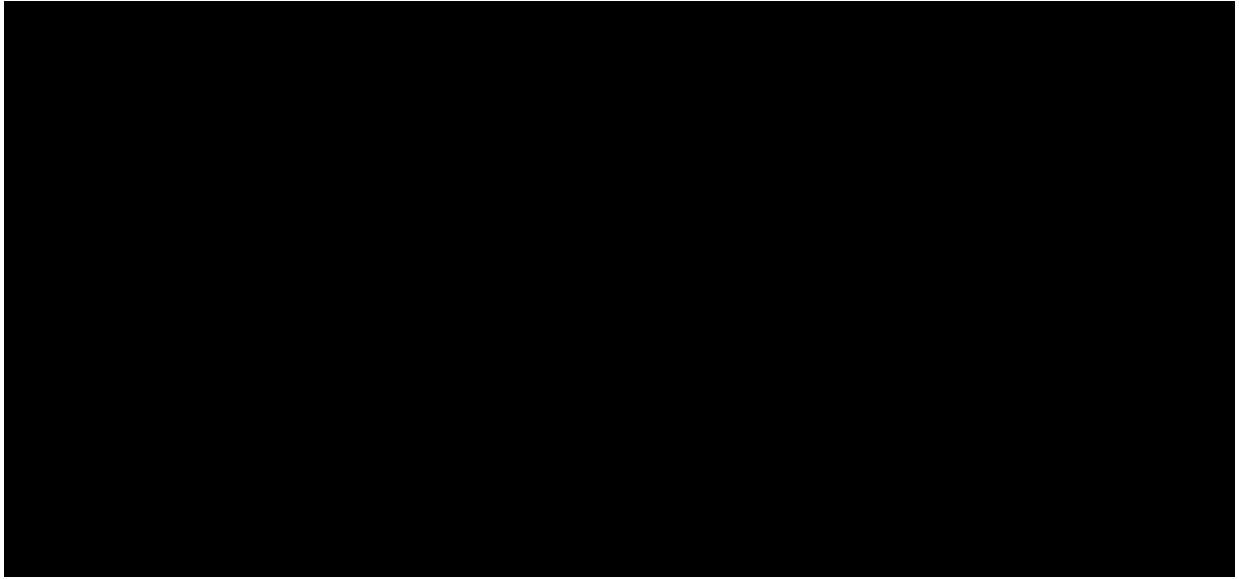


Figure 21. ReO-KYCAR Structure Labelled with 1-letter Amino Acid Code

	Residue	Free Ligand	Peak 1	Peak 2	Δ ppm
K	HN	7.42	-	-	-
	H α	3.84	3.97	4.86	0.89
	H β	1.73	1.87	2.08	0.21
		-	1.82	1.99	0.17
	H γ	1.24	1.48	1.68	0.20
	H δ	1.53	1.65	1.81	0.16
	H ϵ	2.85	2.92	3.09	0.17
Y	H ζ		7.51	7.65	0.14
	HN	8.69	-	-	-
	H α	4.41	4.89	5.19	0.30
	H β	2.91	3.16	3.40	0.24
		2.75	3.12	2.78	-0.34
	H δ	6.96	6.82	6.99	0.17
H ϵ	6.66	6.58	6.74	0.16	
C	HN	8.69	-	-	-
	H α	4.20	4.88	5.04	0.16
	H β	2.60	3.78	3.95	0.17
		-	3.25	3.48	0.23
A	HN	8.19	8.45	8.62	0.17
	H α	4.04	4.12	4.28	0.16
	H β	1.25	1.27	1.43	0.16
R	HN	8.24	8.26	8.42	0.16
	H α	4.19	4.18	4.33	0.15
	H β	1.78	1.75	1.91	0.16
		1.64	1.60	1.78	0.18
	H γ	1.49	1.45	1.61	0.16
	H δ	3.05	3.04	3.20	0.16
	H ϵ	7.03	7.00	7.17	0.17

Table 4. ^1H NMR of KYCAR, ReO-KYCAR peak 1, ReO-KYCAR peak 2, and the change (Δ) in ppm between peak 1 and peak 2

The deprotonation of the amide groups was immediately observed on the tyrosine and cysteine residues, thus showing the coordination to the Re-oxo core. The β -proton of the lysine shows two resonances in the complex resulting from the change in electron density due to the complexation to the metal core. The β -proton of the cysteine also shows two resonances due to the deprotonation of the thiol.

As seen previously in the literature, typically technetium(V)-oxo complexes carry a square pyramidal structure with the metal oxo group in the apical position when complexed to a tetradentate ligand.⁹⁴⁻⁹⁶ It is postulated that the peak 1, or the anti isomer, has the lysine side chain opposite the Re-oxo core and on opposite sides of the plane. Therefore peak 2, or the syn isomer, has the lysine side chain and the Re-oxo core on the same side of the plane. To further confirm this, the chemical shifts for the syn isomer are all located downfield in comparison to the anti isomer and the free KYCAR ligand, which correlates to the deshielding effect imposed by the Re-oxo core. To assist in the deconvolution of the ^1H chemical shifts, 2D TOCSY spectra were obtained. Formation of the lysine and cysteine β -proton resonances is also observed (Figures 22, 23).

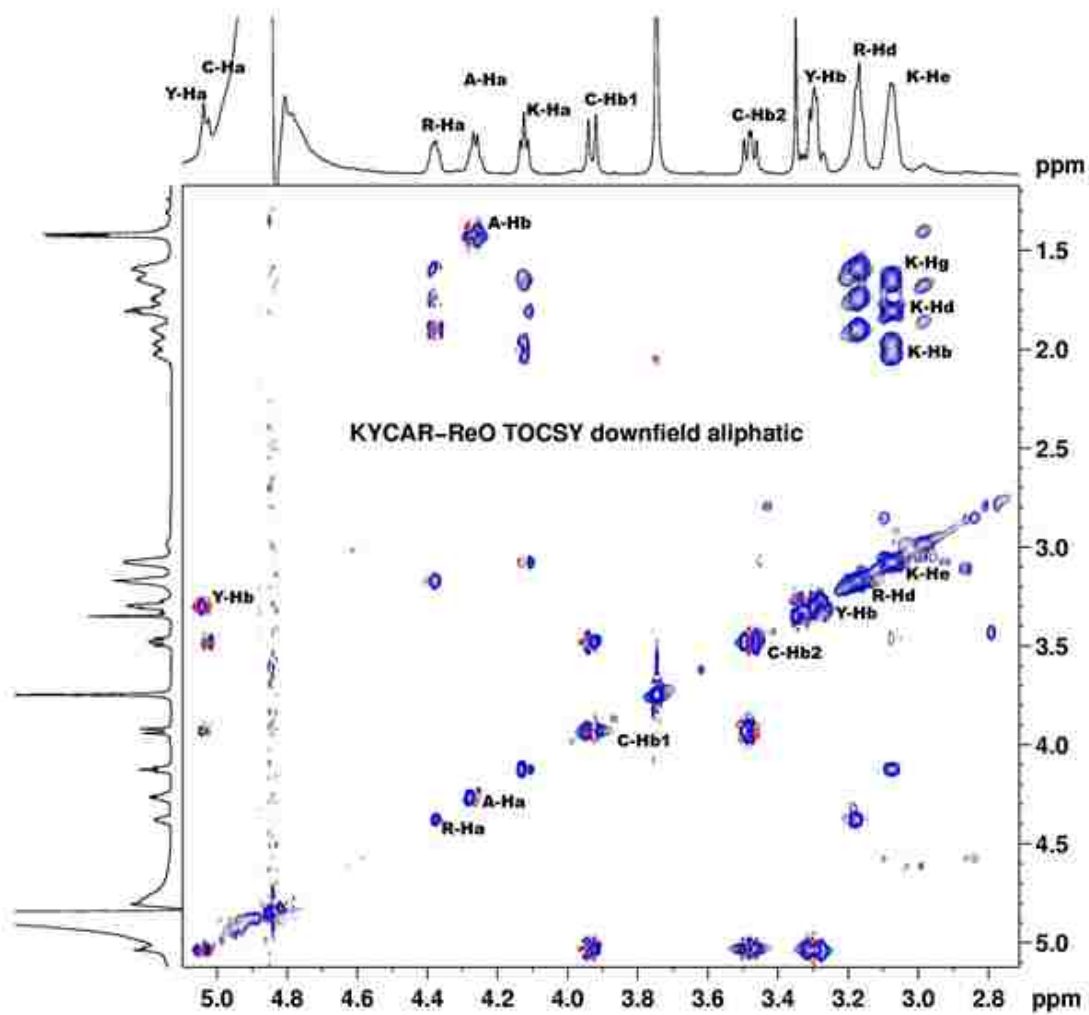


Figure 22. ReO-KYCAR Peak 2 (Syn) Downfield Aliphatic TOCSY

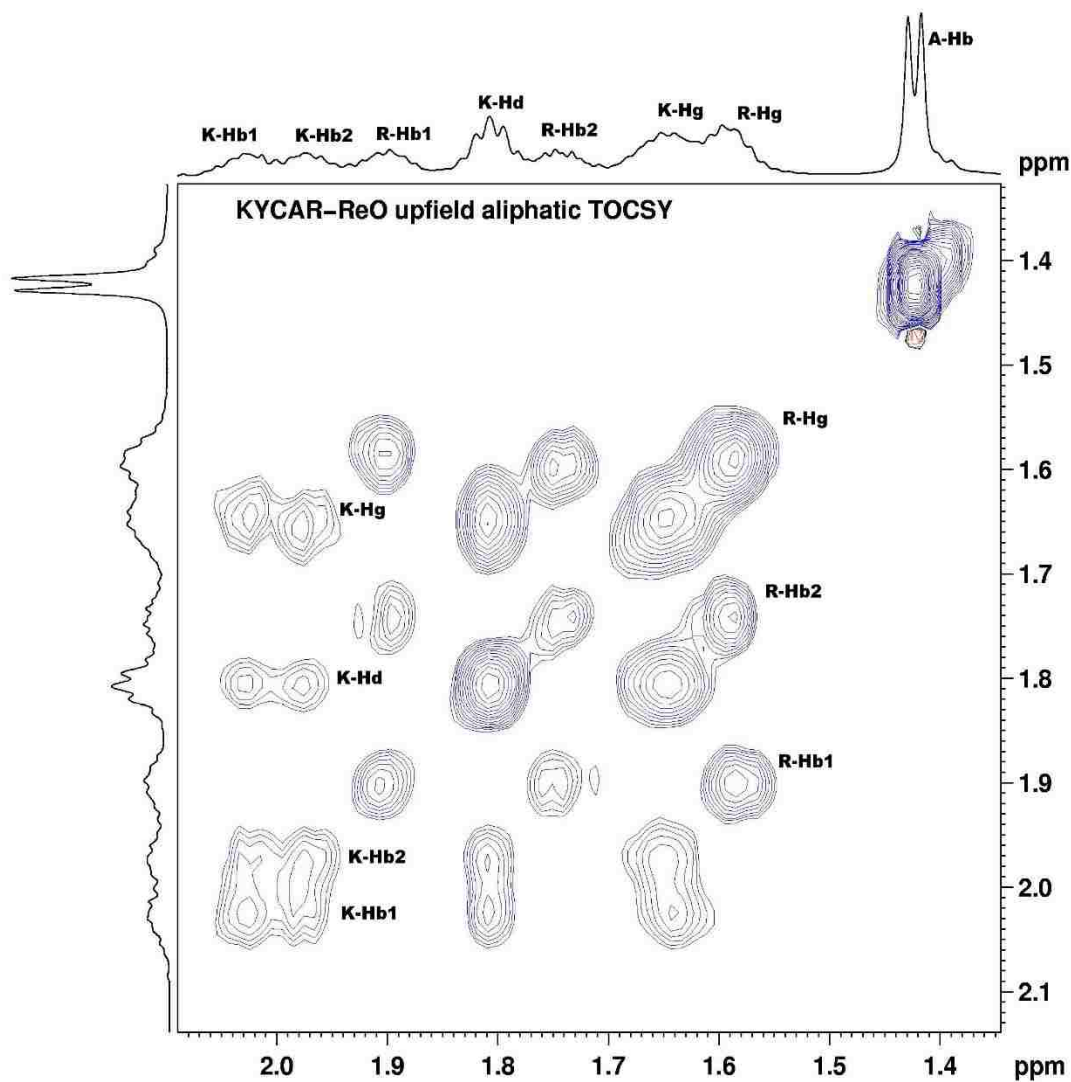


Figure 23. ReO-KYCAR Peak 2 (syn) Upfield Aliphatic TOCSY

NMR titration curves were used to determine the pK_a 's of specific residues on ReO-KYCAR and the free KYCAR ligand. For this study, it was decided to monitor the H_α and the H_ϵ found on the lysine of each construct (Figure 24 and 25).

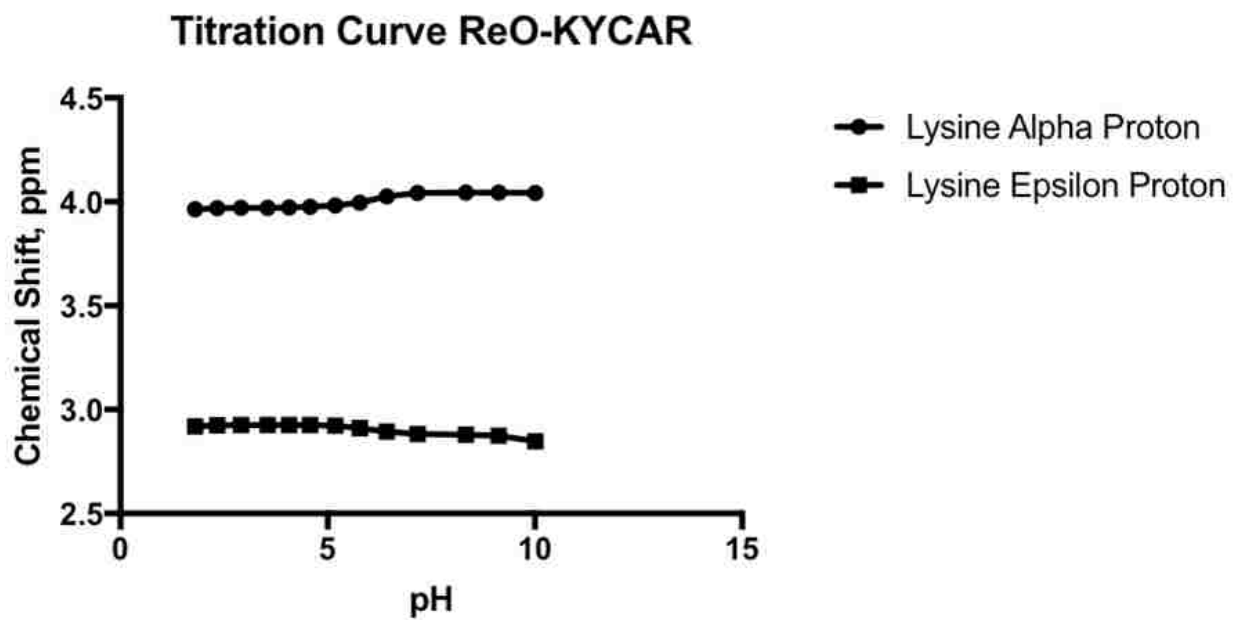


Figure 24. NMR Titration Curve for ReO-KYCAR. Connected dots represent the lysine alpha proton, and the connected squares represent the lysine epsilon protons.

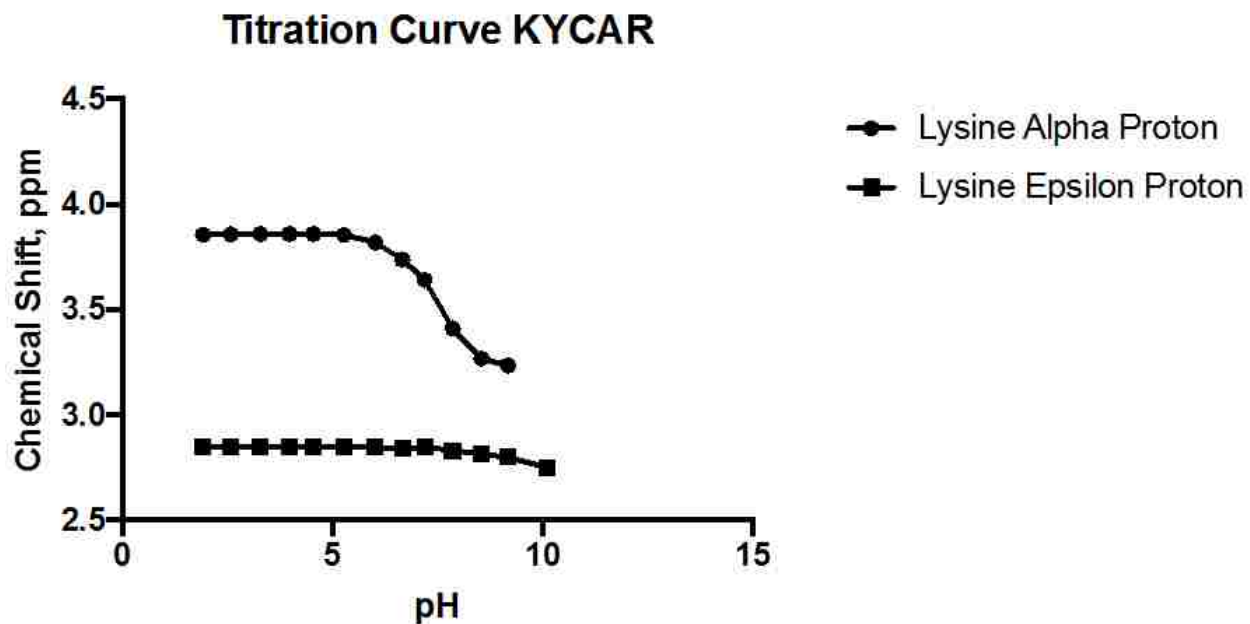


Figure 25. NMR Titration Curve for the free KYCAR ligand. Connected dots represent the lysine alpha proton, and the connected squares represent the lysine epsilon protons.

To determine the pK_a values a NMR titration procedure described by Rose et. al.⁹³. Briefly the values were determined by plotting pH vs. $100[(\sigma_{obs}-\sigma_{HL}) / (\sigma_L - \sigma_{HL})]$. Here σ_{obs} is the chemical shift at a specific pH; σ_{HL} is the chemical shift of the highest pH; σ_L is the chemical shift of the lowest pH. Below are tables summarizing the calculation (Tables 5-8) and figures highlighting the plots and the pK_a values (Figures 26-29)

ReO-KYCAR KHa α		
pH	δ , ppm of KH α	$100[\delta_{\text{obs}}-\delta_{\text{HL}}]/(\delta_{\text{L}}-\delta_{\text{HL}})$
1.8	3.965	0.0
2.34	3.969	5.2
2.91	3.97	6.5
3.55	3.971	7.8
4.07	3.972	9.1
4.58	3.976	14.3
5.19	3.982	22.1
5.78	3.995	39.0
6.43	4.025	77.9
7.17	4.042	100.0
8.34	4.045	103.9
9.13	4.045	103.9
10.01	4.042	100.0

Table 5. Chemical shifts (middle column) of the alpha proton on the lysine of ReO-KYCAR at various pH. The first and last columns represent the x and y axes for the following figure.

ReO-KYCARG K_Halpha

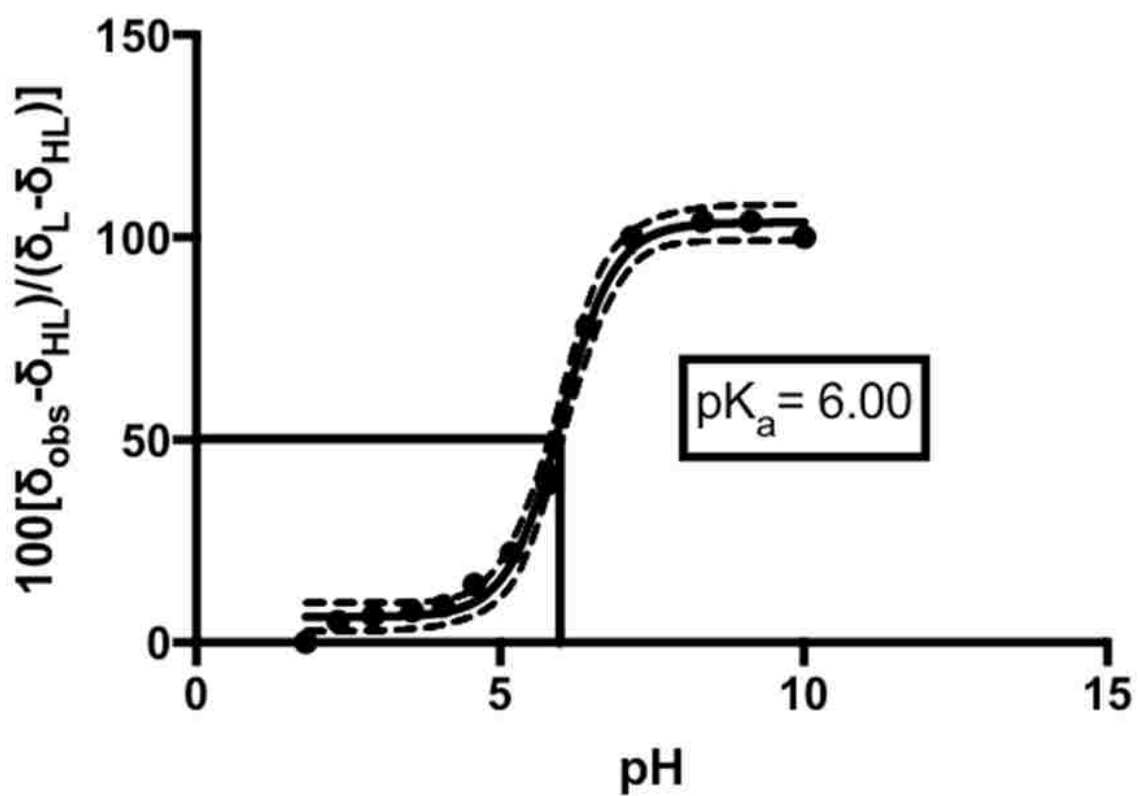


Figure 26. NMR titration curve for ReO-KYCARG alpha proton on the lysine. $pK_a=6.00$ plotted by Prism via sigmoidal curve fit. Free solid dots represent experimental data points, dashed and solid lines are representative of the sigmoidal curve fit.

ReO-KYCAR KHepsilon		
pH	δ , ppm of $\text{KH}\epsilon$	$100[\delta_{\text{obs}} - \delta_{\text{HL}}]/(\delta_{\text{L}} - \delta_{\text{HL}})$
1.8	2.92	0.0
2.34	2.924	-5.6
2.91	2.926	-8.3
3.55	2.926	-8.3
4.07	2.926	-8.3
4.58	2.926	-8.3
5.19	2.923	-4.2
5.78	2.91	13.9
6.43	2.894	36.1
7.17	2.883	51.4
8.34	2.88	55.6
9.13	2.875	62.5
10.01	2.848	100.0

Table 6. Chemical shifts (middle column) of the epsilon proton on the lysine of ReO-KYCAR at various pH. The first and last columns represent the x and y axes for the following figure.

ReO-KYCAR KHepsilon

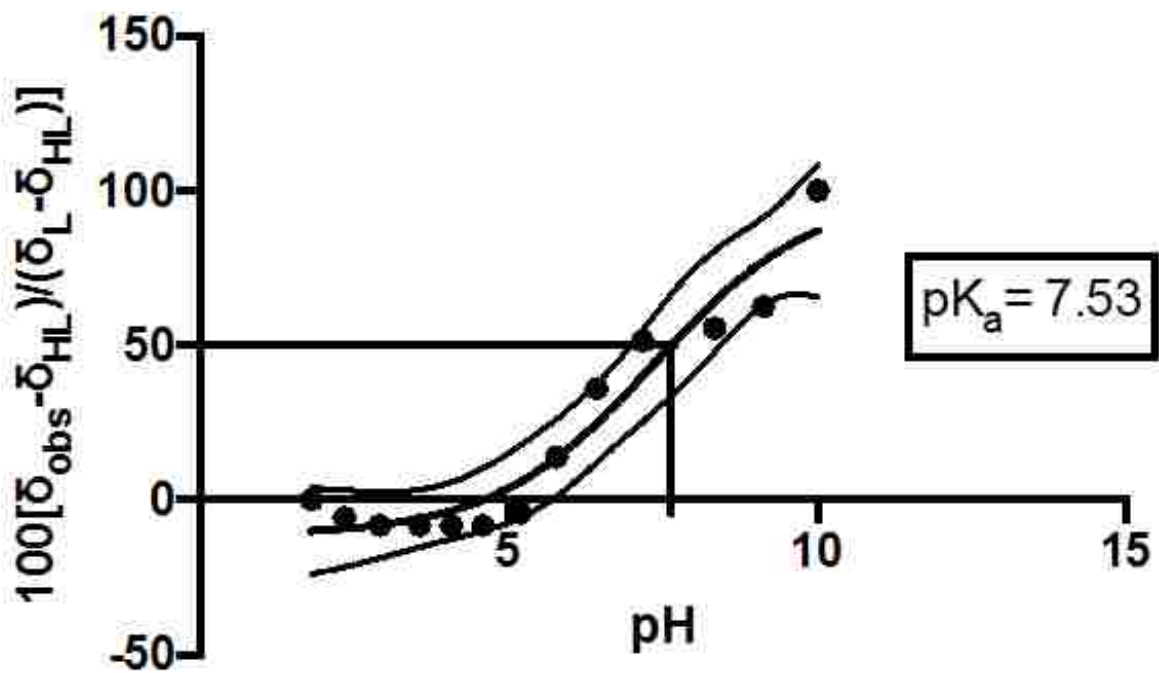


Figure 27. NMR titration curve for ReO-KYCAR epsilon proton on the lysine. $pK_a=7.53$ plotted by Prism via sigmoidal curve fit. Free solid dots represent experimental data points, dashed and solid lines are representative of the sigmoidal curve fit.

KYCAR KHalpha		
pH	δ , ppm of $\text{KH}\alpha$	$100[\delta_{\text{obs}} - \delta_{\text{HL}}]/(\delta_{\text{L}} - \delta_{\text{HL}})$
1.91	3.856	0.0
2.57	3.858	-0.3
3.28	3.86	-0.6
3.97	3.86	-0.6
4.54	3.86	-0.6
5.27	3.854	0.3
6.01	3.82	5.8
6.65	3.737	19.1
7.19	3.64	34.7
7.85	3.411	71.5
8.54	3.267	94.7
9.17	3.234	100.0

Table 7. Chemical shifts (middle column) of the alpha proton on the lysine of free KYCAR at various pH. The first and last columns represent the x and y axes for the following figure.

KYCAR KHalpha

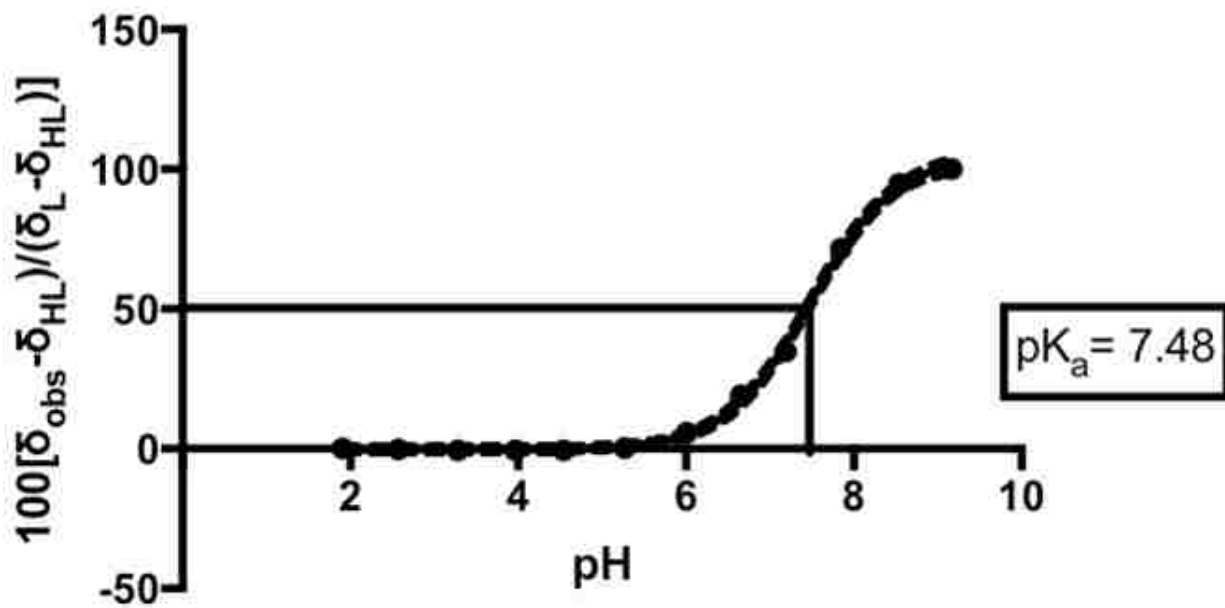


Figure 28. NMR titration curve for free KYCAR alpha proton on the lysine. $pK_a=7.48$ plotted by Prism via sigmoidal curve fit. Free solid dots represent experimental data points, dashed and solid lines are representative of the sigmoidal curve fit.

KYCAR KHepsilon		
pH	δ , ppm of KHe	$100[\delta_{\text{obs}} - \delta_{\text{HL}}]/(\delta_{\text{L}} - \delta_{\text{HL}})$
1.91	2.845	0.0
2.57	2.847	-2.1
3.28	2.847	-2.1
3.97	2.847	-2.1
4.54	2.849	-4.2
5.27	2.849	-4.2
6.01	2.845	0.0
6.65	2.84	5.3
7.19	2.847	-2.1
7.85	2.831	14.7
8.54	2.814	32.6
9.17	2.8	47.4
10.1	2.75	100.0

Table 8. Chemical shifts (middle column) of the epsilon proton on the lysine of free KYCAR at various pH. The first and last columns represent the x and y axes for the following figure.

KYCAR Kepsilon

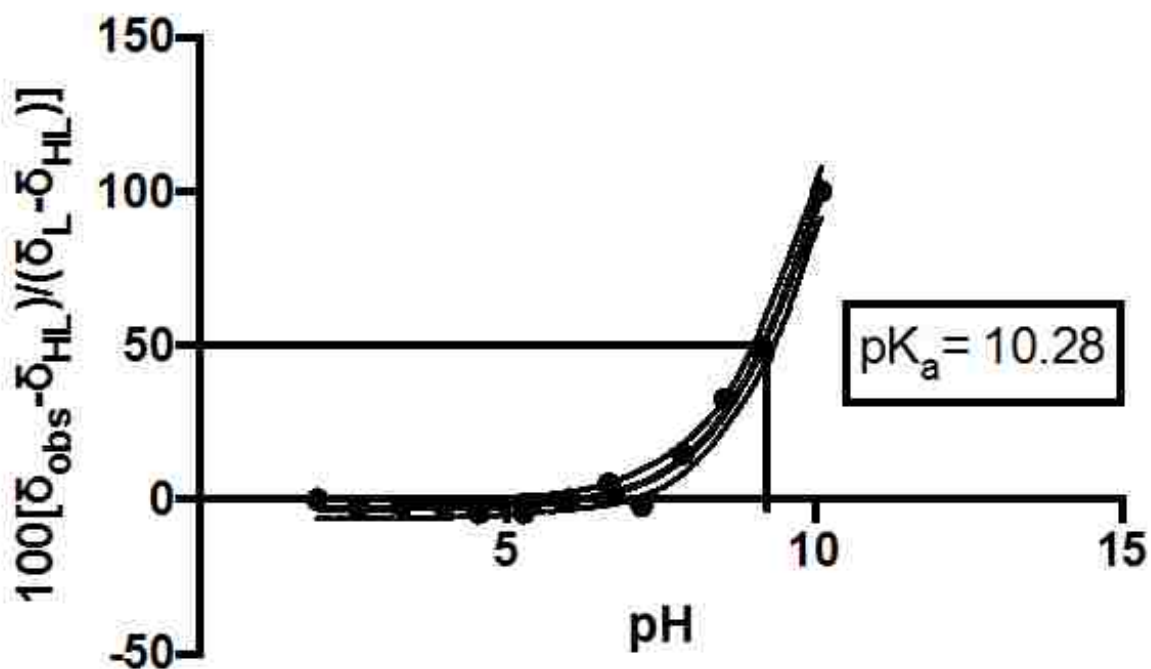


Figure 29. NMR titration curve for free KYCAR epsilon proton on the lysine. $pK_a=10.28$ plotted by Prism via sigmoidal curve fit. Free solid dots represent experimental data points, dashed and solid lines are representative of the sigmoidal curve fit.

In the free ligand, it was determined that the pK_a 's of the alpha proton and the epsilon proton on the lysine were 7.48 and 10.28 respectively. Also, the pK_a 's of the alpha proton and the epsilon proton on the lysine of ReO-KYCAR were 6.00 and 7.53 respectively. Due to the lower pK_a values for the alpha proton on the lysine of ReO-KYCAR, it is hypothesized that there may be an interaction between the Re=O core and the Re-N bonds that could facilitate the deprotonation of the NH_2 terminus on the lysine. This would create a Re- N_{amide} bond for the lysine N-terminus of the peptide. The Re- N_{amide} bond would carry a negative charge and this

suggests that under physiological pH, the chelator region of the ReO-KYCAR is negatively charged.

2.13.2.2. Infrared Spectroscopy

The infrared spectra for the anti and syn peaks C indicates a Re=O stretching frequency at 991 cm^{-1} and 990 cm^{-1} , respectively. These values are slightly shifted to higher energies to 984 cm^{-1} , which was observed from $(\text{Bu}_4\text{N})[\text{ReOBr}_4(\text{H}_2\text{O})]\cdot\text{H}_2\text{O}$, indicating that the Re=O bond from peaks B and C exhibit slightly more double bond character. The diastereomers also exhibit a broad peak at $2800\text{-}3500\text{ cm}^{-1}$, characteristic of the phenol and carboxylic acid O-H and amine N-H. Both peaks exhibit a strong intensity stretching frequency at around 1649 cm^{-1} (anti) and 1654 cm^{-1} (syn), indicative of the C=O secondary amide bond, specifically representing an amide I band. New medium intensity stretching frequencies at 1515 cm^{-1} (anti) and 1514 cm^{-1} (syn) are characteristic of our secondary amide as well, specifically corresponding to an amide II band.

The last new major peak that appears in ReKYCAR exhibits a strong intensity stretching frequency at 1199 cm^{-1} (anti) and 1198 cm^{-1} (syn), corresponding to the secondary amide C=O amide III band. For the syn peak specifically, a stretching frequency characteristic of a C=O ester band as our NMR confirmed is expected. It is believed that the ester carbonyl stretch shifted and overlaps with the amide carbonyl stretch at 1654 cm^{-1} because the infrared spectra of the syn peak reveals that there are actually 2 peaks at around 1654 cm^{-1} , whereas the infrared spectra of the anti isomer exhibits only 1 peak at 1649 cm^{-1} . This double peak indicates that the ester and amide carbonyl stretches are overlapping (Figure 30).

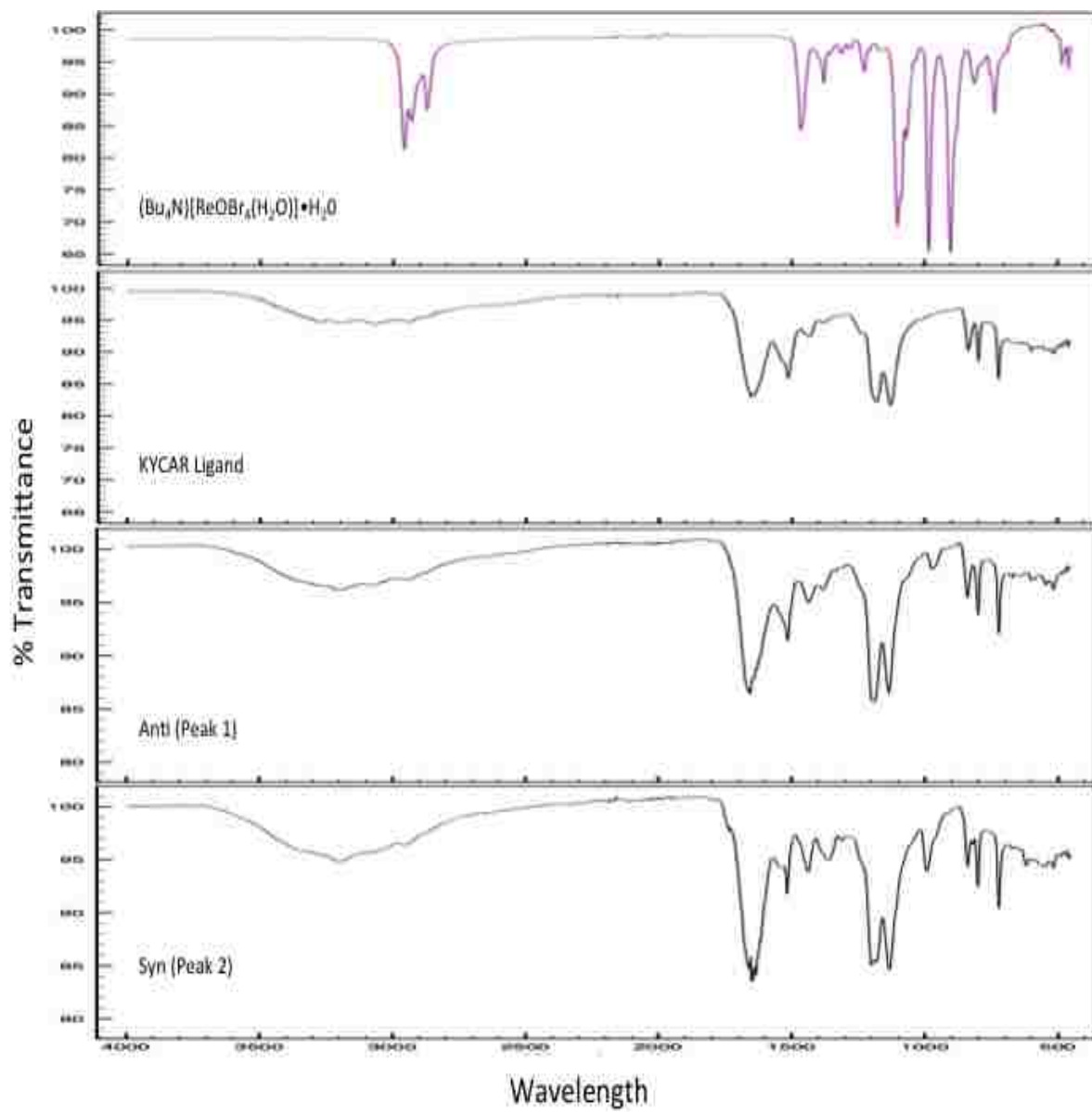


Figure 30. IR Spec. of KYCAR(Top), Re starting material, ReO-KYCAR peak 1, ReO-KYCAR peak 2(Bottom)

2.13.2.3. Circular Dichroism

To observe structural signatures of each of the isolated peaks, peaks 1 (anti) and peak 2 (syn), CD spectra were obtained and are shown below (Figure 31).

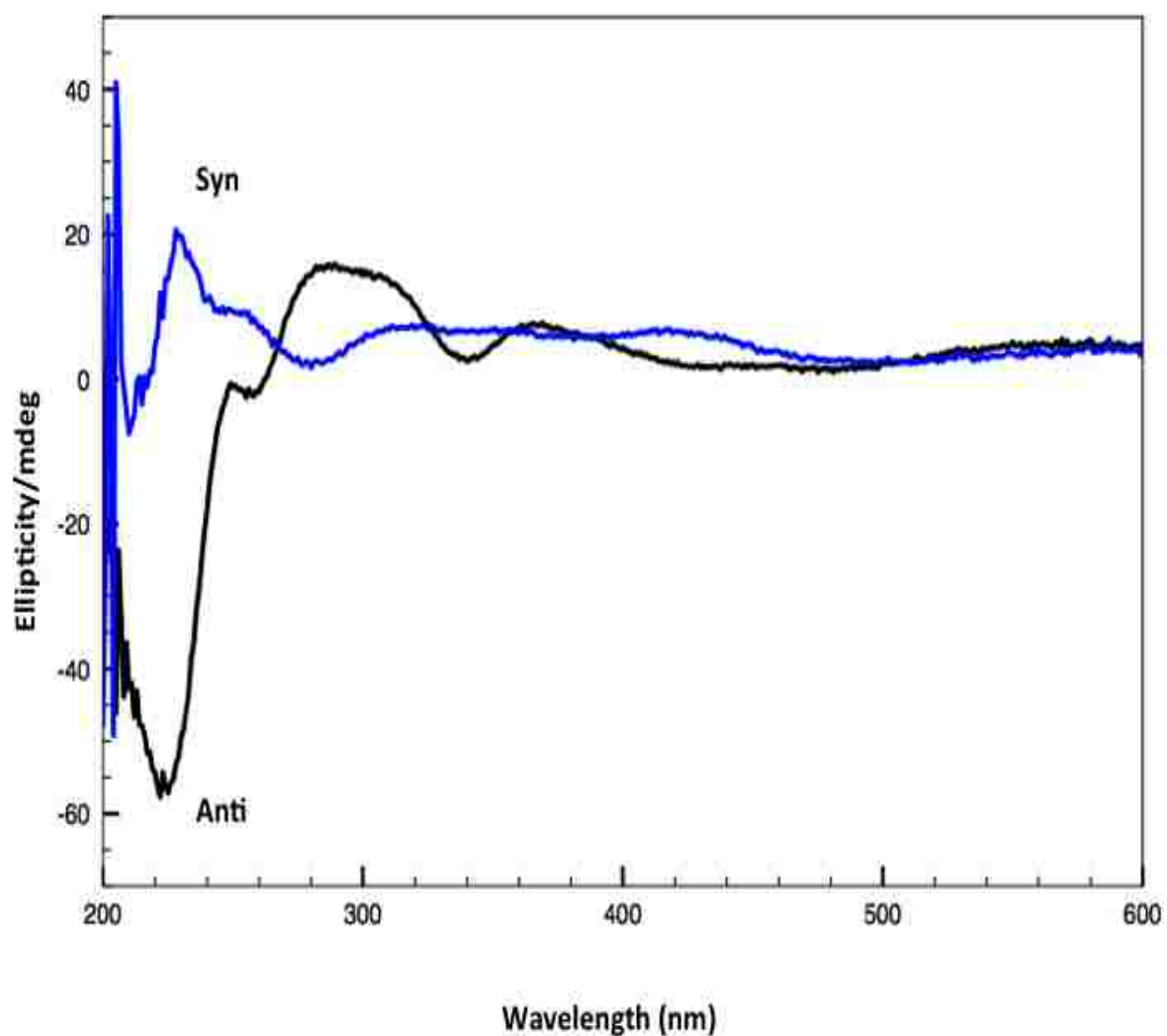


Figure 31. Circular Dichroism of ReO-KYCAR Peak 1(anti) (Black), and ReO-KYCAR Peak 2 (syn) (Blue)

The areas that provide the most information lie between 280 and 340 nm. Within this region are transitions, which include ligand to metal charge transfer. According to previous studies on rhenium-Schiff base complexes, this region correlates to the oxygen to rhenium charge transfer transitions.^{97,98} The strong positive Cotton effect, or characteristic change in optical rotatory, around 280 nm is assigned to the Re-oxo core in the anti position. Conversely, we see a negative Cotton effect of the Re-oxo core in the syn position. The postulated anti and syn circular dichroism spectra can be confirmed by comparing this CD data to previously reported data showing anti and syn complexes with crystallographically characterized Re-and Tc peptides (Figure 32).⁸⁸

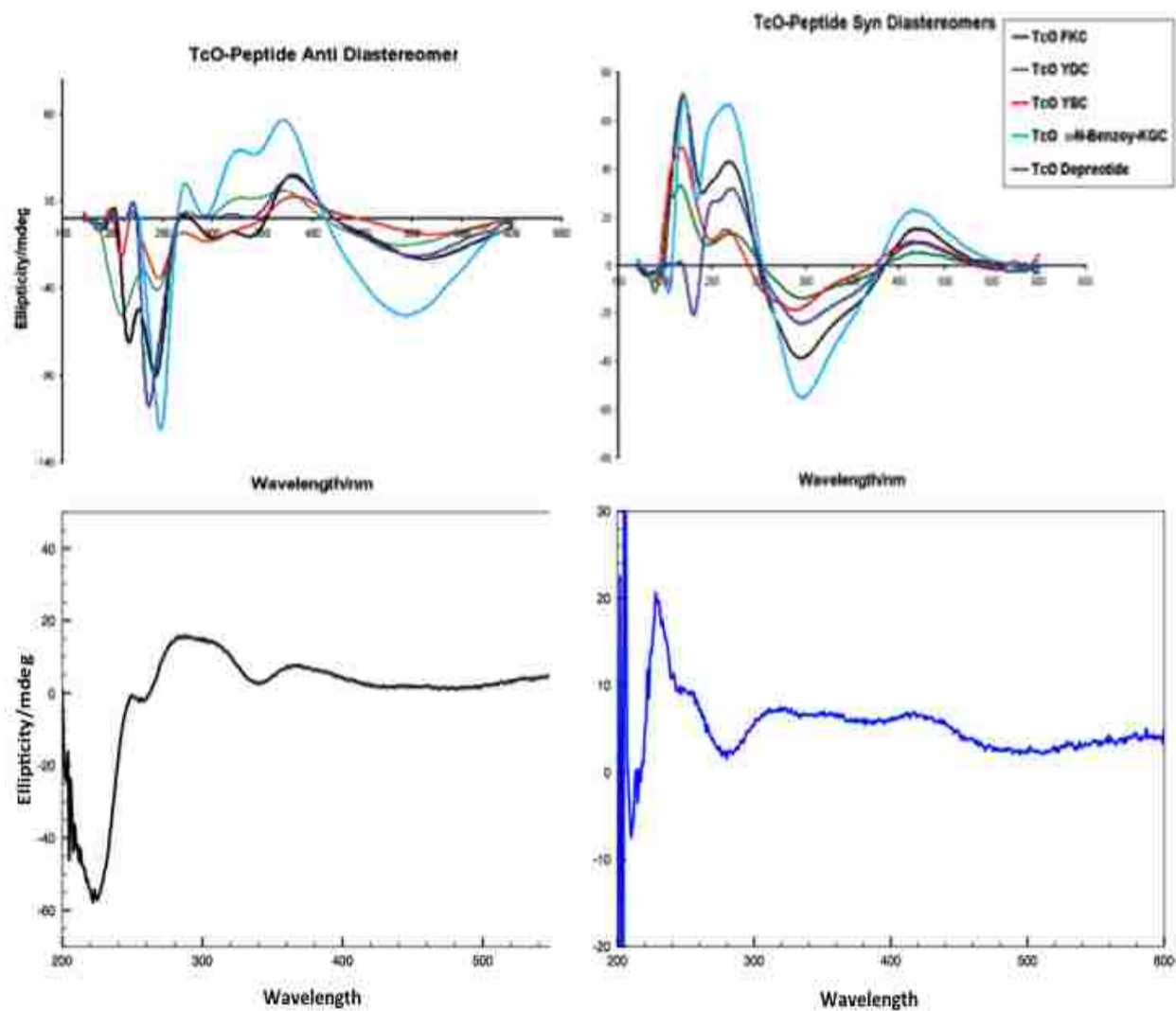


Figure 32. Comparison of Previously Reported Anti and Syn Metal-Peptides

2.13.2.4. Crystallography

The following (Tables 9, 10) shows a summary of crystallization results of peaks 1 and 2 ReO-KYCAR. The purification crystallization technique yielded a powdery substance along the walls of the vial, however the material did not diffract. The vapor diffusion technique yielded

two possible materials. The first was determined to be an oily substance, while the second which was crystalline in nature was determined to be rhenium oxide salt covered in an oil of our product.

Peak 1					
Number	Technique	Solvents Used	Temperature	Results	Comments
1	Vapor Diffusion	H2O Toluene	4°C	Nothing	
2	Solvent Evaporation	EtOH Toluene	25°C	Nothing	
3	Vapor Diffusion	MeOH Toluene	4°C	Oil	
4	Vapor Diffusion	EtOH Pentane	4°C	Oil	Submitted for XRD determined to be an oil; possible product with impurities
5	Vapor Diffusion	EtOH Diethyl ether	4°C	Powder	
6	Vapor Diffusion	MeOH Diethyl ether	4°C	Crystalline	Submitted for XRD Determined to possibly be Re-oxide salt
7	Vapor Diffusion	Acetonitrile H2O Pentane	4°C	Powder	
8	Vapor Diffusion	EtOH Pentane	4°C	Nothing	
9	Solvent Evaporation	EtOH Dichloromethane	25°C	Oil	
10	Solvent Evaporation	MeOH Pentane	25°C	Nothing	

Table 9. Summary of Crystallization Results ReO-KYCAR Peak1 (anti)

Peak 2					
Number	Technique	Solvents Used	Temperature	Results	Comments
1	Solvent Evaporation	MeOH Toluene	25°C	Nothing	
2	Solvent Evaporation	EtOH Toluene	25°C	Oil	
3	Vapor Diffusion	H2O Toluene	4°C	Powder	
4	Vapor Diffusion	EtOH Pentane	4°C	Nothing	
5	Vapor Diffusion	MeOH Pentane	4°C	Powder	
6	Vapor Diffusion	Ethylene Glycol Pentane	4°C	Nothing	
7	Vapor Diffusion	H2O Acetonitrile Pentane	4°C	Oil	
8	Solvent Evaporation	MeOH Diethyl Ether	25°C	Oil	
9	Vapor Diffusion	Ethyl Acetate Pentane	4°C	Oil	
10	Purification Crystallization/ Solvent Evaporation	EtOH Diethyl Ether	25°C	Residue	Submitted for XRD determined the material did not diffract
11	Purification Crystallization/ Solvent Evaporation	MeOH Diethyl Ether	25°C	Nothing	
12	Purification Crystallization/ Solvent Evaporation	H2O Diethyl Ether	25°C	Nothing	

Table 10. Summary of Crystallization Results ReO-KYCAR Peak 2 (syn)

Due to the unsuccessful attempts crystallizing ReO-KYCAR, ReO-KYC-NH₂ (ReO-KYC) (Figure 33) crystallization was attempted to investigate the structure around the complexation region. An amide capped peptide was used to prevent any potential methyl esterification from

occurring. Crystals of similar ReO and TcO tripeptide complexes bearing cysteine at the carboxylate terminus have been previously obtained and reported in the literature.⁸⁸ ReO-KYC was synthesized and analyzed via reverse phase HPLC (Figure 34). Post synthesis there are two major peaks present corresponding to two diastereomers. It is postulated that peak 1 is the anti peak and peak 2 is the syn peak. Orange crystals were obtained by supersaturation in methanol over 1 week. The crystal and structure refinement data are tabulated in table 11. Bond lengths and bond angles are tabulated in table 12, and the Ball and Stick diagrams are shown in Figure 35.

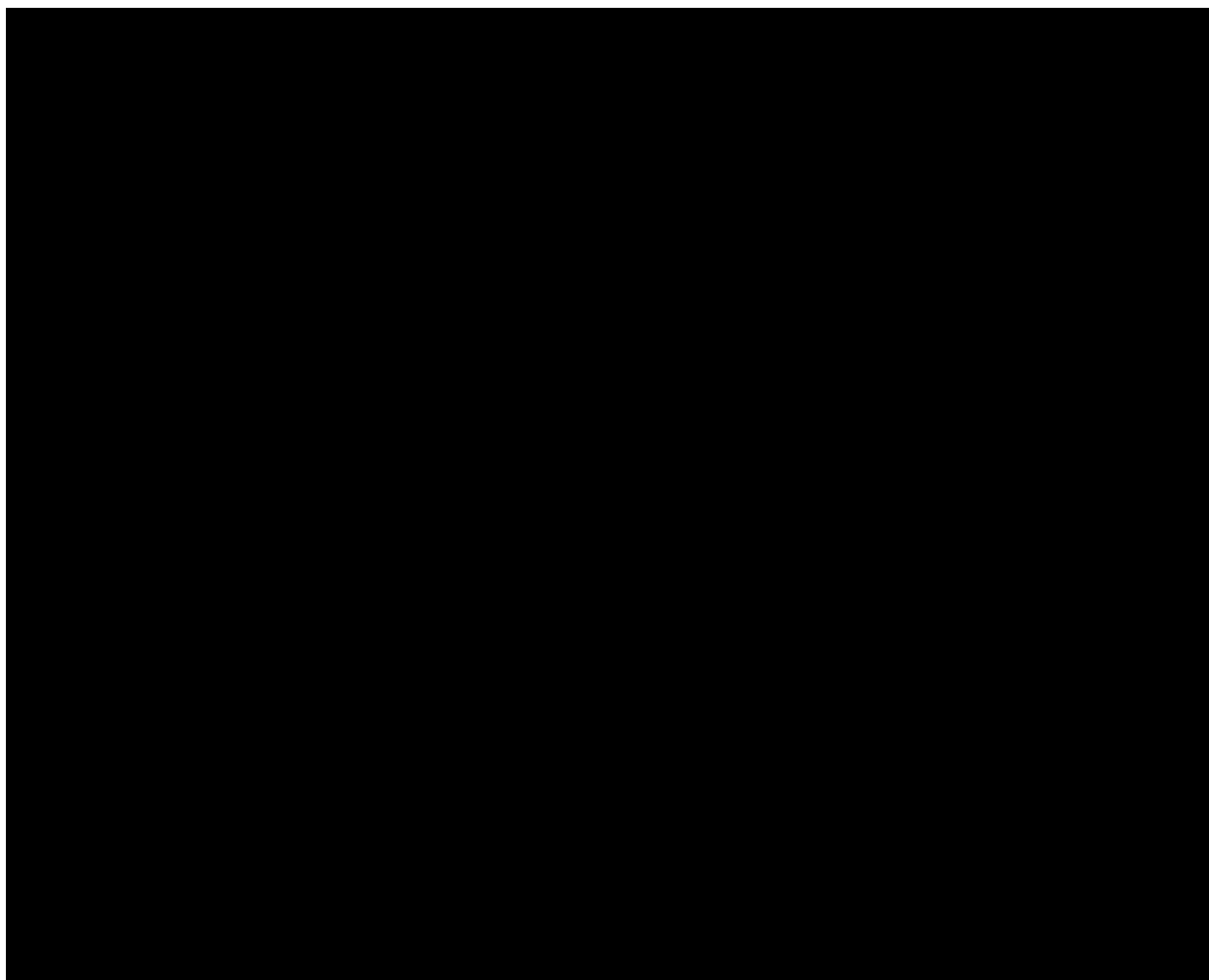


Figure 33. Structure of ReO-KYC

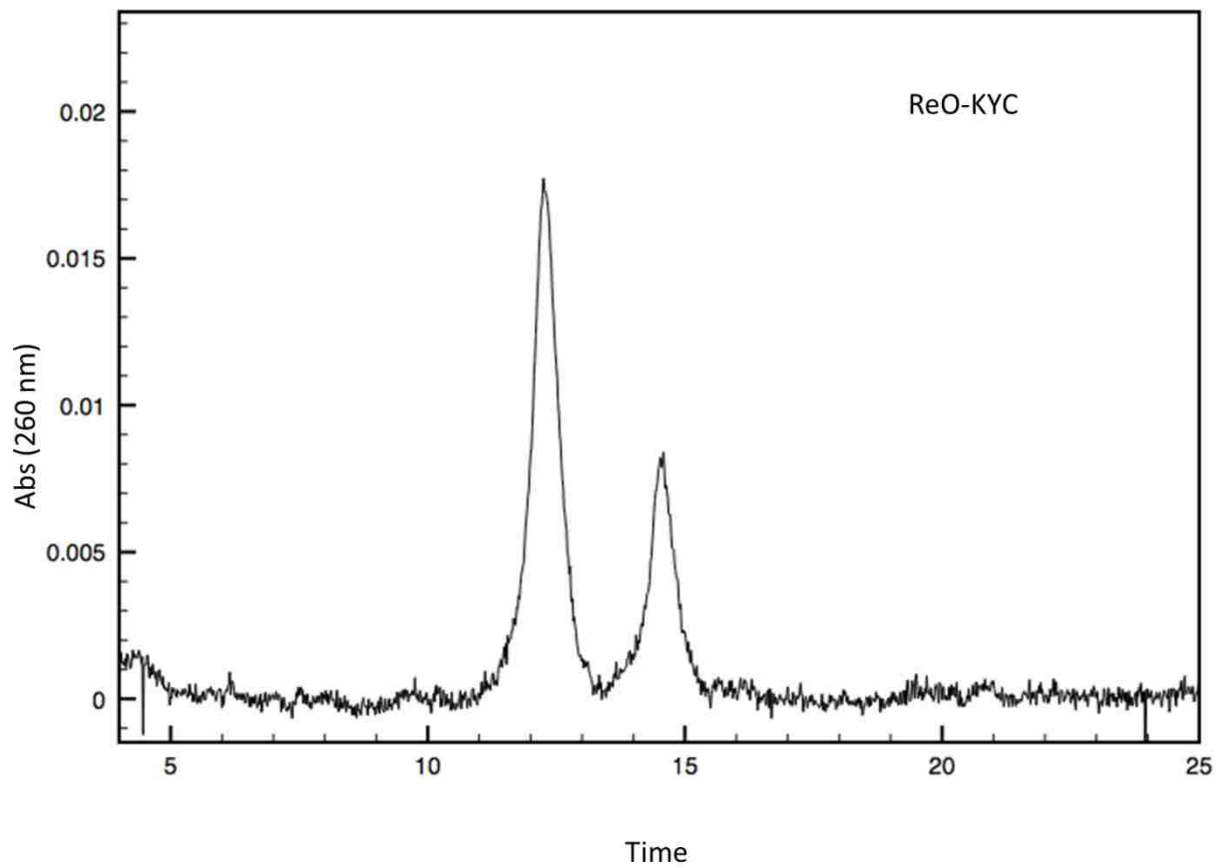


Figure 34. Reversed Phase HPLC of ReO-KYC Post Synthesis. Shows 2 major peaks. Peak 1 (anti) and peak 2 (syn)

	[(KYC-H)ReO][Br]
Lattice	Orthorhombic
Formula	C ₁₈ H ₂₇ BrN ₅ O ₅ ReS
Formula Weight	691.61
Space Group	P2 ₁ 2 ₁ 2 ₁
a/Å	9.1349(6)
b/Å	9.2608(7)
c/Å	26.2652(18)
α/°	90
β/°	90
γ/°	90
V/Å ³	2221.9(3)
Z	4
Temperature (K)	130(2)
Radiation (λ, Å)	0.71073
P (calcd.)g/cm ³	2.067
M (Mo Kα), mm ⁻¹	7.402
θ max, deg.	34.735
No. of Data Collected	44331
No. of Data	9549
No. of Parameters	303
R ₁ [I > 2σ(1)]	0.0247
wR ₂ [I > 2σ(1)]	0.0444
R ₁ [all data]	0.0288
wR ₂ [all data]	0.0453
GOF	1.024
R _{int}	0.048

Table 11. Crystal and Structure Refinement Data for ReO-KYC Peak 2 (syn)

Bond Length (Å)	[(KYC-H)ReO][Br]
Re-O	1.676(3)
Re-N1	1.983(3)
Re-N2	1.984(3)
Re-N3	2.117(3)
Re-S	2.2630(9)
N3-C6	1.497(5)
Bond Angle (deg)	
N2-Re-N3	79.06(12)
N3-Re-S	91.22(9)
N1-Re-N2	78.72(12)
N1-Re-S	82.66(9)
O-Re-N3	107.62(12)
O-Re-N2	113.23(12)
O-Re-N1	111.94(13)

Table 12. Bond Lengths and Bond Angles for ReO-KYC Peak 2 (Syn)

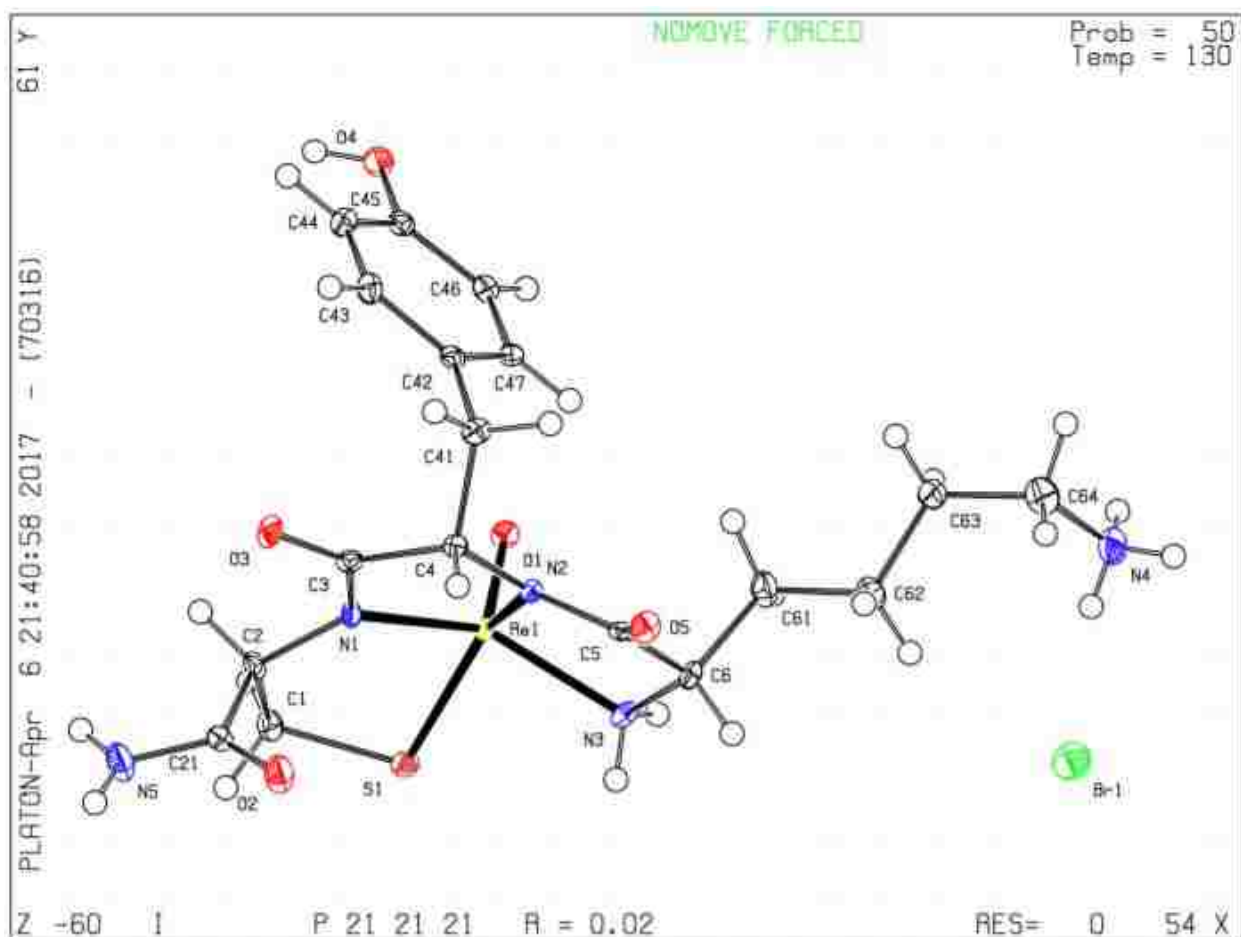


Figure 35. Ball and Stick Diagram for ReO-KYC (syn)

The crystal structure determined that the coordinating nitrogen on the lysine (N3) is an amine nitrogen. Also, the molecule exhibits a tetrahedral geometry, as all of the oxygen-rhenium-nitrogen bond angles fall in the 109.5° range. The crystallization in a non-centrosymmetric space group confirms that there is only one enantiomer present.

The crystals were dissolved and reinjected into the HPLC to confirm which peak coordinates with the syn diastereomer (Figure 36). The reversed phase HPLC trace shows that

the dissolved crystal corresponds to peak 2. Correlating this data to ReO-KYCAR it can be confirmed that peak 2 is also the syn diastereomer.

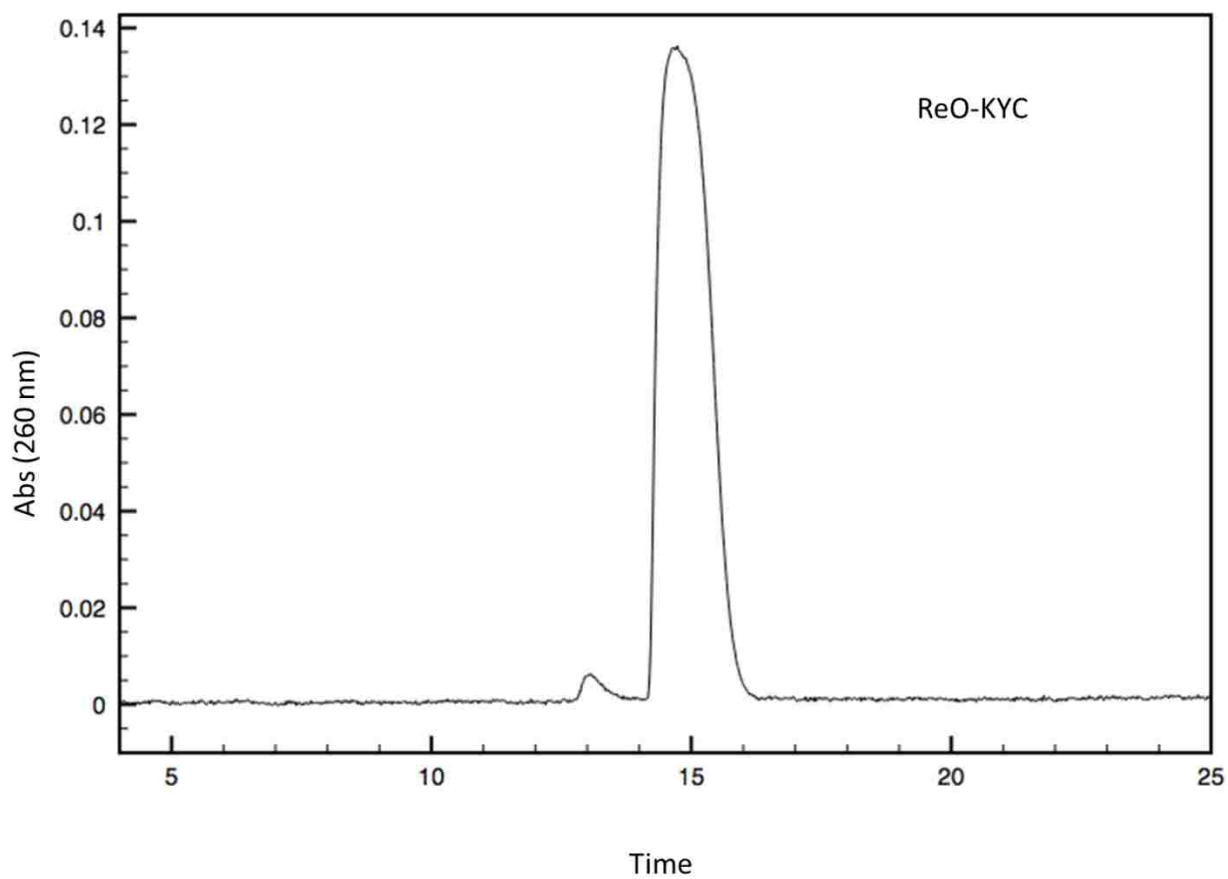


Figure 36. Reversed phase HPLC of ReO-KYC syn crystals confirming that peak 2 corresponds to the syn crystal structure.

2.13.3. Biology

The ^{99m}Tc -KYCAR and ^{188}Re -KYCAR stabilities in phosphate buffered saline (PBS) (Figure 37) and human serum (Figure 38) were evaluated *in vitro* via HPLC analysis. The ^{99m}TcO -KYCAR remained relatively stable with very little $^{99m}\text{TcO}_4^-$ growing in up to 2 hours. Decomposition of the complex to $^{99m}\text{TcO}_4^-$ would result in a peak with an elution time of 5 minutes. The *in vitro* incubation of ^{99m}TcO -KYCAR in human serum results in an immediate slight decomposition of the complex to $^{99m}\text{TcO}_4^-$ and another polar species. Though there is immediate decomposition there is no further decomposition up to 2 hours.

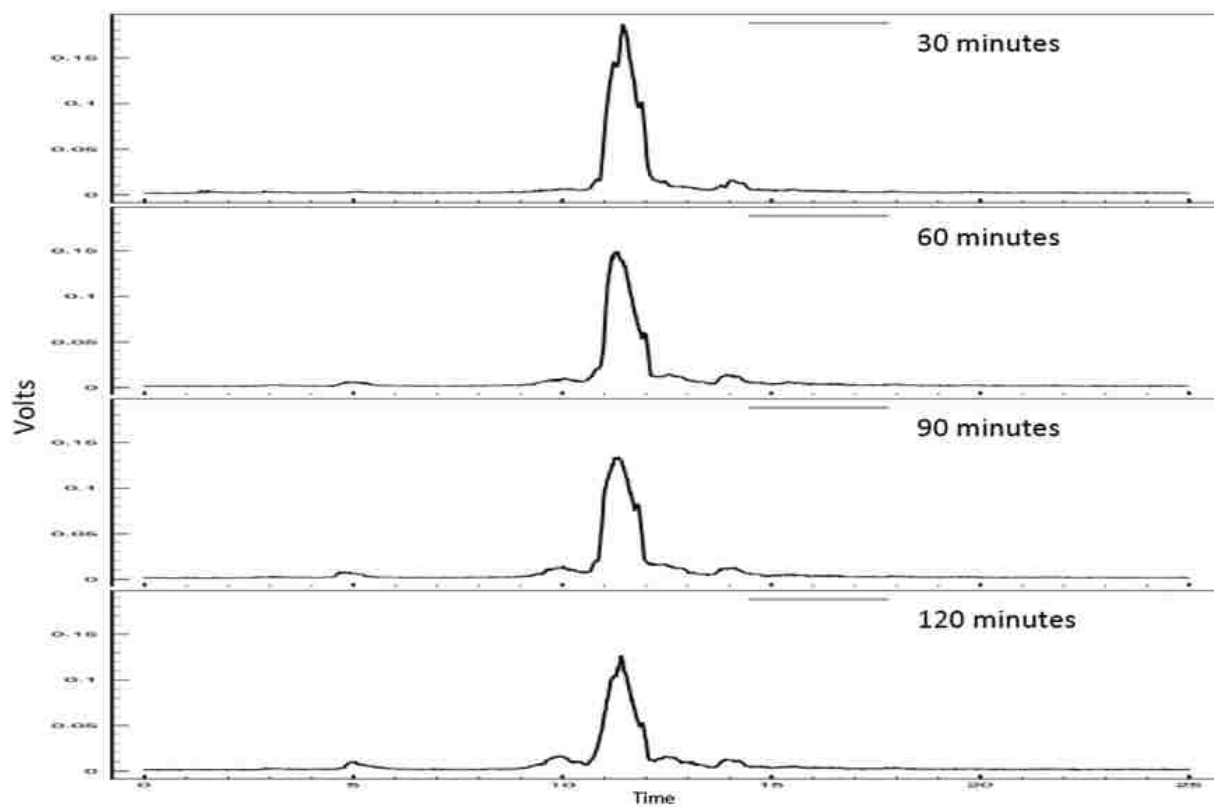


Figure 37. HPLC of $^{99m}\text{TcO-KYCAR (syn)}$ in PBS monitored over time

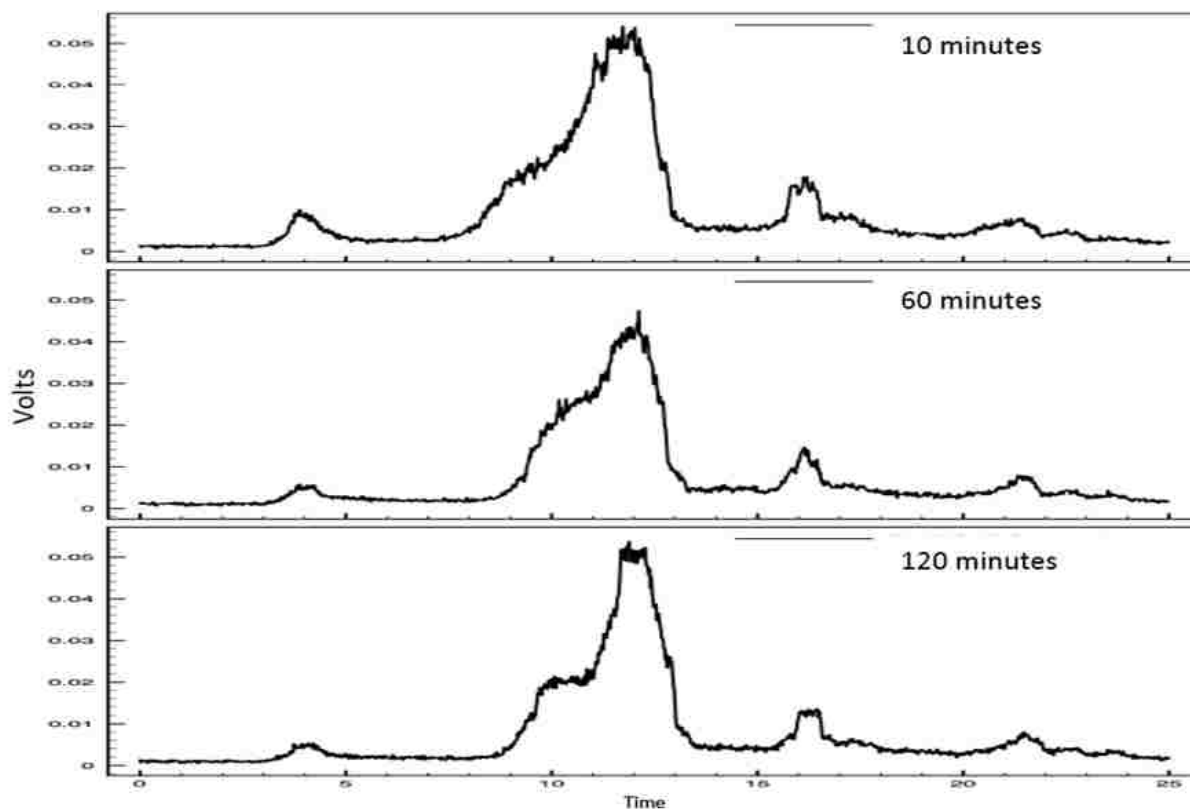


Figure 38. HPLC of $^{99m}\text{TcO-KYCAR}$ (syn) in Human Serum monitored over time

The biological distribution of $^{99m}\text{Tc-KYCAR}$ and $^{188}\text{Re-KYCAR}$ were of interest to understand the uptake of the complexes as well as monitor the degradation *in vivo*. The complexes were HPLC purified, reconstituted with sterile saline and injected into healthy athymic nude female mice intravenously. Animals were sacrificed at 30 min, 1 hr, 2 hrs, and 4 hrs post injection, and the results are summarized below as the percent of the injected dose to each selected organ of the mouse (%ID/g) (Table 13, Figure 39).

Organ	%ID/g \pm S.D.			
	30 min	1 hr	2 hr	4 hr
Blood	1.77 \pm 0.37	1.37 \pm 0.14	1.08 \pm 0.20	0.91 \pm 0.04
Heart	0.66 \pm 0.6	0.42 \pm 0.05	0.58 \pm 0.22	0.33 \pm 0.06
Lungs	1.39 \pm 0.23	1.13 \pm 0.18	1.52 \pm 0.98	0.99 \pm 0.38
Liver	22.10 \pm 4.80	13.35 \pm 1.85	4.37 \pm 1.55	1.83 \pm 0.19
Spleen	0.82 \pm 0.25	0.69 \pm 0.13	0.57 \pm 0.18	0.44 \pm 0.17
Stomach	4.57 \pm 0.86	5.06 \pm 1.33	5.83 \pm 2.10	4.07 \pm 1.03
Small Intestine	22.82 \pm 3.66	30.49 \pm 10.05	21.18 \pm 10.14	3.62 \pm 1.28
Large Intestine	0.31 \pm 0.07	0.30 \pm 0.04	1.82 \pm 1.81	36.77 \pm 10.76
Kidneys	5.95 \pm 0.60	5.58 \pm 0.85	5.09 \pm 0.50	4.87 \pm 0.54
Muscle	0.25 \pm 0.11	0.24 \pm 0.10	0.19 \pm 0.01	0.24 \pm 0.12
Bone	0.71 \pm 0.15	0.59 \pm 0.16	0.53 \pm 0.32	0.50 \pm 0.18
Skin	1.12 \pm 0.36	0.57 \pm 0.06	0.49 \pm 0.11	0.47 \pm 0.07
Thyroid	38.44 \pm 11.07	118.75 \pm 15.13	116.71 \pm 23.20	146.44 \pm 42.20
Gall Bladder	590.36 \pm 274.09	840.72 \pm 523.07	206.78 \pm 104.24	164.07 \pm 136.89

Table 13. $^{99m}\text{TcO-KYCAR}(\text{syn})$. The results are reported in %ID/g. Shows that the activity travels through the gastrointestinal track. Also shows some decomposition to $^{99m}\text{TcO}_4^-$ as seen with thyroid accumulation

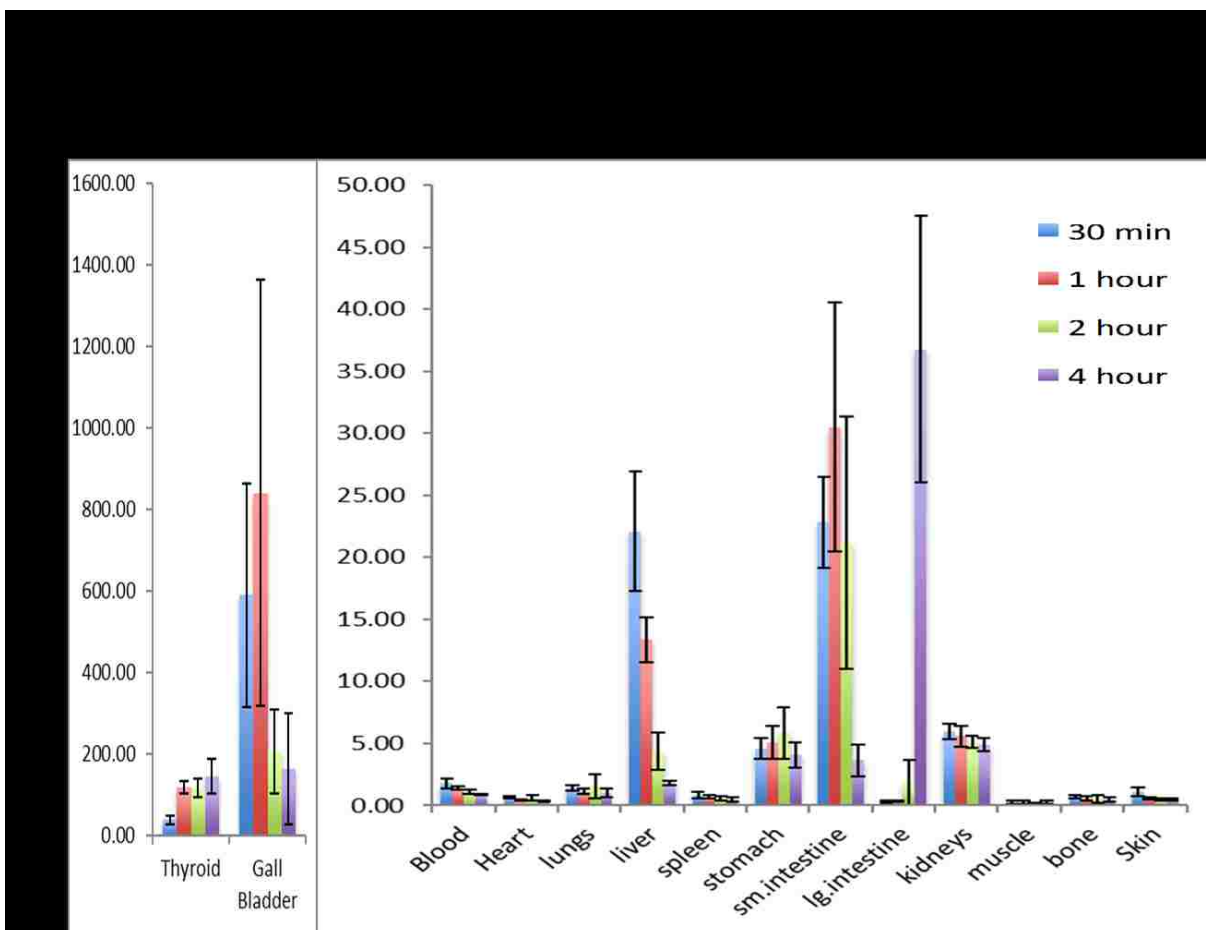


Figure 39. $^{99m}\text{TcO-KYCAR}(\text{syn})$. The results are reported in %ID/g. Shows that the activity travels through the gastrointestinal track. Also shows some decomposition to $^{99m}\text{TcO}_4^-$ as seen with thyroid accumulation

$^{99m}\text{Tc-KYCAR}$ shows high uptake in the liver after 30 minutes (22.10 %ID/g). High liver uptake may be due to the large size and structure of the complex. After 4 hours, the radioactivity in the liver decreased to 1.83 %ID/g indicating efficient clearance and low amounts of accumulation over time in the liver. Concurrently, $^{99m}\text{Tc-KYCAR}$ exhibited rapid accumulation in the small intestine 30 minutes post injection (22.82%ID/g), with subsequent depletion 4 hours post injection (3.62 %ID/g). As expected from this trend, levels of the radiotracer in the

large intestine increased from 0.31 %ID/g at 30 minutes to 36.77 %ID/g at 4 hours. Thus, it can be assumed that the majority of the radioactivity in the intestines arrives and is excreted via the hepatobiliary system despite the hydrophilic nature of our radiotracer ($\log D = -2.631$).

Uptake and retention of our radioligand is also seen in moderate amounts in the kidneys (5.95 %ID/g at 30 min to 4.87 %ID/g at 4 hours) indicating some excretion through the renal system. These findings are contradictory to the hypothesis that increased hydrophilicity would favor renal excretion over hepatobiliary excretion, but it is believed that the large molecular weight of the radiolabeled peptide complex favors this method of excretion. The radioactivity accumulation in the stomach for $^{99m}\text{Tc-KYCAR}$ decreased with time, showing 4.07 %ID/g retained 4 hours post injection, as compared to 4.57 %ID/g at 30 minutes, indicating that the in vivo stability correlates well with the high in vitro stability that was previously observed. Significantly, low uptake and retention of $^{99m}\text{Tc-KYCAR}$ was observed at 4 hours in the heart (0.33 %ID/g), lungs (0.99 %ID/g), spleen (0.44 %ID/g) and muscle (0.24 %ID/g). The low level of radioactivity in the blood already at 30 minutes (1.77 %ID/g) indicates favorable and rapid blood clearance (decreases to 0.91 %ID/g at 4 hour).

Figure 40 shows the stability of $^{188}\text{ReO-KYCAR}$ in PBS over time. It shows an immediate decomposition of the complex with two peaks. The first peak which elutes at around 5 minutes corresponds to $^{188}\text{ReO}_4^-$, and the second is the $^{188}\text{ReO-KYCAR}$ complex. Though the initial contact with PBS results in a relatively large amount of decomposition the sub sequential HPLC traces show very little growth of the perrhenate peak. The stability of $^{188}\text{ReO-KYCAR}$ in serum is particularly interesting in that the complex does not appear to be very stable. After contacting

the rhenium complex with human serum for 30 minutes there is only $^{188}\text{ReO}_4^-$ present in the supernatant (Figure 41).

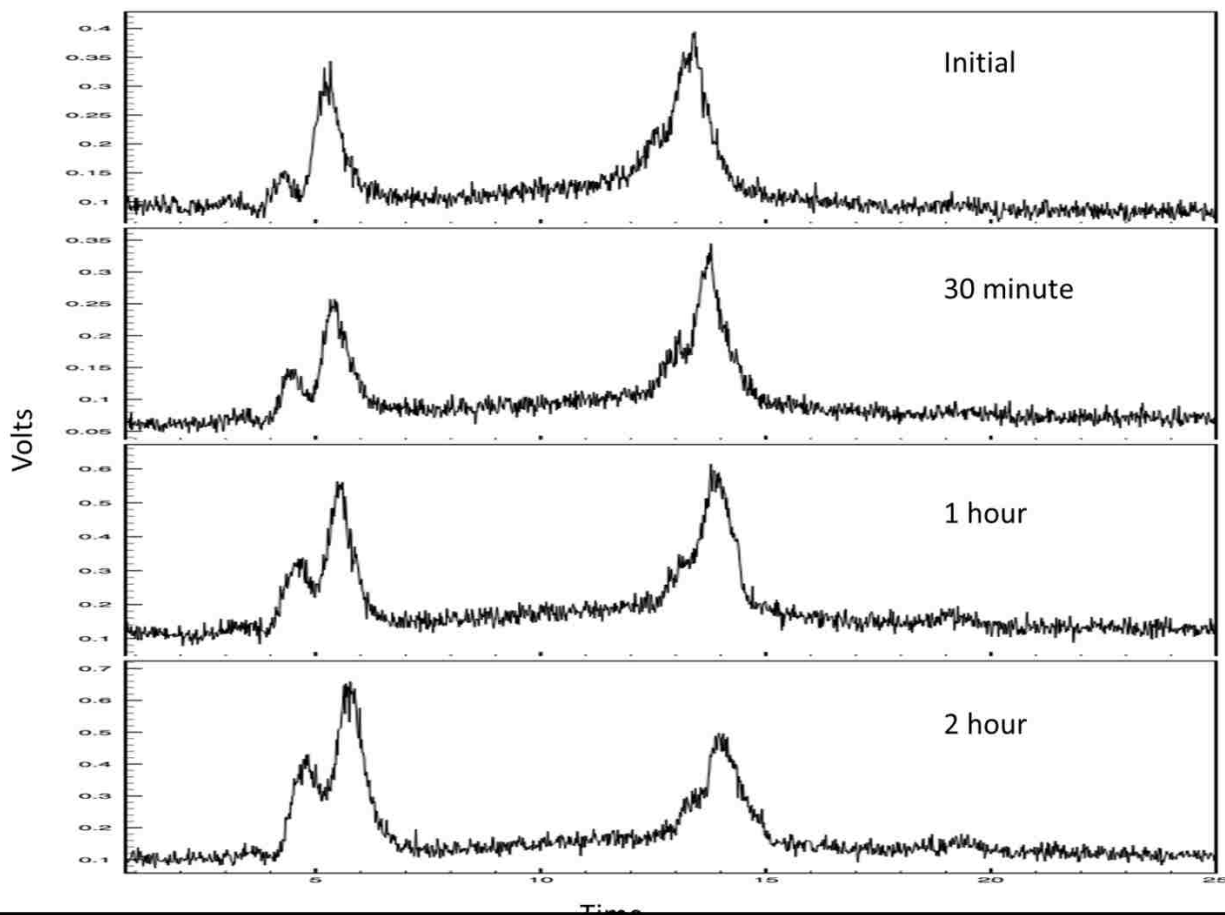


Figure 40. HPLC of $^{188}\text{ReO-KYCAR (syn)}$ in PBS monitored over time

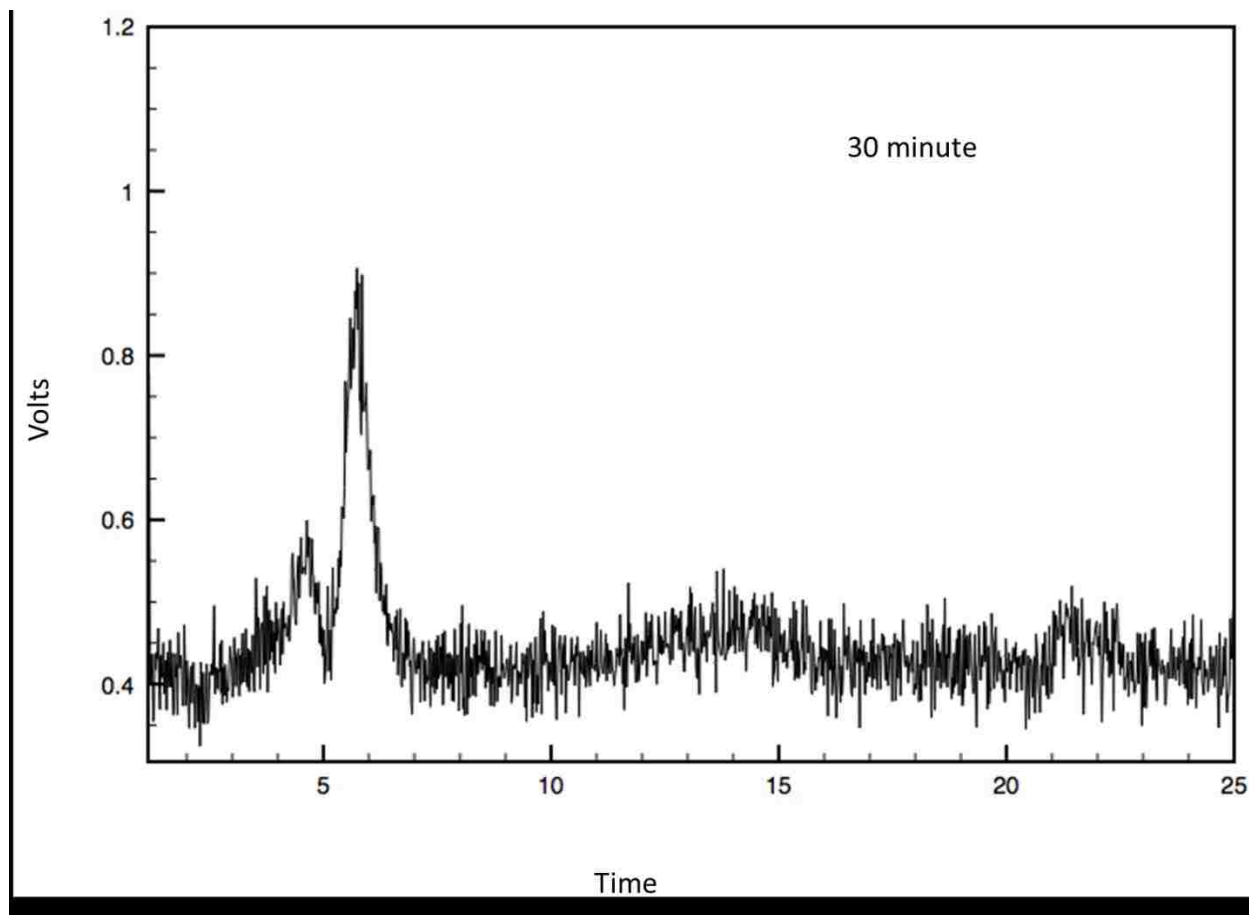


Figure 41. HPLC of $^{188}\text{ReO-KYCAR}$ (syn) monitored in Human Serum over time

Despite the *in vitro* biology results it was important to analyze the behavior of $^{188}\text{ReO-KYCAR}$ *in vivo* which is shown (Table 14, Figure 42). Very similar trends are observed with the $^{188}\text{ReO-KYCAR}$ construct and the $^{99\text{m}}\text{TcO-KYCAR}$. Its logD value of -2.280 reveals that it is slightly more hydrophobic than the $^{99\text{m}}\text{TcO-KYCAR}$ construct, therefore we expect it to have an increased preference for the hepatobiliary pathway. At 30 minutes, radioactivity in the liver is 17.61 %ID/g, and just as the technetium-labeled pentapeptide, after 4 hours radioactivity

decreases to 0.99 %ID/g. There is a large amount of accumulation observed in the intestines, similar to the technetium construct. At 30 minutes, the radioactivity in the small intestine is 33.15 %ID/g, while the radioactivity in the large intestine is expectedly low at 0.38 %ID/g. After 4 hours, the radioactivity in the small intestine decreases to 0.95 %ID/g, while the radioactivity in the large intestine increases to 31.99 %ID/g. Although there is uptake in the kidneys (3.81 %ID/g at 30 minutes), the amount of uptake is less than it is for ^{99m}Tc -KYCAR, corresponding with the logD values, and confirming that the rhenium construct is even more inclined to be excreted through the hepatobiliary system. Similarly, to the technetium construct, the radioactivity accumulation in the stomach for ^{188}Re -KYCAR decreases with time, showing 2.50 %ID/g retained 4 hours post injection, as compared to 6.24 %ID/g at 30 minutes. Again, this indicates that it retains stability and does not decompose to perrhenate at high rates in vivo over time. Significantly, the uptake value for all other collected organs is <1%ID/g after 4 hours.

%ID/g \pm S.D.				
Organ	30 min	1 hr	2 hr	4 hr
Blood	1.29 \pm 0.43	0.94 \pm 0.12	0.71 \pm 0.18	0.38 \pm 0.07
Heart	0.45 \pm 0.15	0.54 \pm 0.28	0.34 \pm 0.23	0.14 \pm 0.02
Lungs	0.97 \pm 0.31	2.13 \pm 1.50	0.87 \pm 0.59	0.29 \pm 0.07
Liver	17.61 \pm 4.30	9.93 \pm 1.53	3.07 \pm 0.68	0.99 \pm 0.14
Spleen	0.65 \pm 0.06	3.07 \pm 5.50	0.38 \pm 0.05	0.24 \pm 0.03
Stomach	6.24 \pm 2.49	7.76 \pm 5.12	7.32 \pm 3.80	2.50 \pm 0.79
Small Intestine	33.15 \pm 14.41	48.77 \pm 12.68	20.68 \pm 22.60	0.95 \pm 0.76
Large Intestine	0.38 \pm 0.15	0.65 \pm 0.44	4.03 \pm 4.47	31.99 \pm 9.13
Kidneys	3.81 \pm 1.26	3.26 \pm 1.47	2.33 \pm 0.07	1.33 \pm 0.22
Muscle	0.49 \pm 0.53	0.38 \pm 0.08	0.35 \pm 0.23	0.18 \pm 0.10
Bone	0.58 \pm 0.05	0.55 \pm 0.10	0.41 \pm 0.07	0.32 \pm 0.05
Skin	0.74 \pm 0.35	0.49 \pm 0.09	0.36 \pm 0.09	0.24 \pm 0.04
Thyroid	57.21 \pm 23.57	113.99 \pm 67.52	118.34 \pm 49.75	84.39 \pm 27.31
Gall Bladder	1085.49 \pm 1084.29	826.44 \pm 1105.72	365.84 \pm 287.48	168.99 \pm 196.65

Table 14. ¹⁸⁸ReO-KYCAR (syn) The results are reported in %ID/g. Shows that the activity travels through the gastrointestinal track. Also shows some decomposition to ^{99m}TcO₄⁻ as seen with thyroid and stomach accumulation

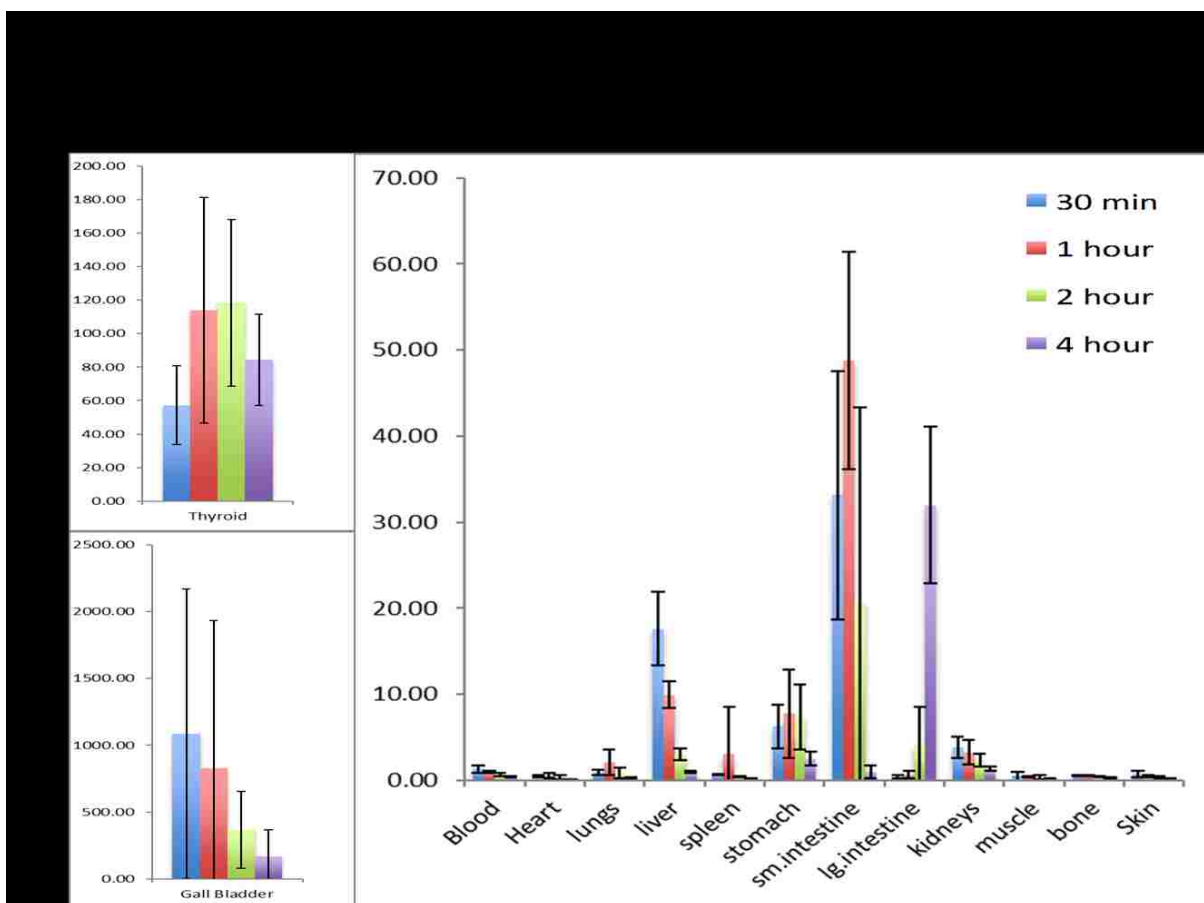


Figure 42. $^{188}\text{ReO-KYCAR (syn)}$ The results are reported in %ID/g. Shows that the activity travels through the gastrointestinal track. Also shows some decomposition to $^{99m}\text{TcO}_4^-$ as seen with thyroid and stomach accumulation

2.14. Conclusion

Without crystal structure data, it is difficult to designate specific diastereomers of metal peptide complexes. Unfortunately, due to the nature of the KYCAR ligand there were no successful crystallization attempts. Most resulted in amorphous powders or impurity filled oils. However, through crystallization of the tripeptide ReO-KYC the diastereomers can be properly assigned. It was determined that the crystallized species was in the syn confirmation and

correlates to peak 2 in the HPLC trace. From this data, it is also determined that the ReO-KYCAR peak 2 is also in the syn confirmation.

HPLC results of ReO-KYCAR initially indicate that two isomeric species of the same complex may be present with both peaks eluting within a few minutes of each other. IR data further conclude that the two isolated species are diastereomers due to the similar stretches and frequencies observed in both complexes.

However, results obtained from ^1H NMR show shifts in the ligand residues that correspond to electron density shifts resulting from a change in the position of the Re-oxo core. Proton NMR data confirms the complex to the metal core by monitoring the absorption of the amide protons of the tyrosine and Cysteine residues. This is also confirmed by the shift in the β -protons on the lysine side chain resulting from a change in electron density about the chelation region. And by the shift in the β -protons on the cysteine side chains due to the deprotonation of the thiol. Proton NMR also begins to assign each of the isolated isomers. The data shows that the second isolated complex has chemical shifts downfield from the free ligand as well as the first peak. The downfield chemical shift correlates to the deshielding effect imposed by the Re-oxo core.

Circular Dichroism data and previous work done on rhenium and various peptides give the most solid information into the diastereomers of ReO-KYCAR. Here we see that the first eluted complex, the anti peak follows the trend of having a large positive Cotton effect about the region that correlates to the oxygen to rhenium charge transfer transitions. Furthermore,

the second eluted complex follows the trend of having a negative Cotton effect about the same region.

Biologically, tracer level complexes (^{99m}Tc , ^{188}Re) are both relatively stable under biological conditions up to 2 hours, though that are some decomposition products present shown by thyroid uptake. $^{99m}\text{TcO-KYCAR}$ shows high uptake in the liver, small intestines and large intestines up to 4 hours post injection. This concludes that the complex is excreted via the hepatobiliary system despite the hydrophilic nature of our radiotracer. However, there is not a large uptake in the stomach and thyroid, which would indicate *in vivo* decomposition. The $^{188}\text{ReO-KYCAR}$ complex shows very similar organ uptake to $^{99m}\text{TcO-KYCAR}$. One noticeable difference is the increased uptake in the stomach. Though relatively low it still indicates decomposition of the complex.

3. ^{99m}Tc and ^{188}Re Pretargeting Spect and Radioimmunotherapy Agents Employing Bioorthogonal Diels Alder Click Chemistry

3.1. Introduction

Monoclonal antibodies (mAbs) offer highly selective binding and affinity for the recognition of virtually any antigen thus represent essential molecules for diagnostic and therapeutic applications.³⁸⁻⁴⁰ Antibodies generally exhibit slow distribution kinetics and slow clearance from the body.^{41, 42} The multi-day biological half-life of an antibody necessitates the use of radioisotopes with comparable physical half-lives, such as ^{89}Zr ($t_{1/2}=3.2$ d) and ^{124}I ($t_{1/2}=4.2$ d), which can lead to high radiation doses to healthy organs.⁴³⁻⁴⁵ In order to reduce the dose to healthy tissues, pretargeting methodologies have been developed. Pretargeted radioimmunoimaging and radioimmunotherapy proceeds by decoupling the monoclonal antibody from the radioisotope and injecting the two components separately, essentially leading to the synthesis of the radioimmunoconjugate at the target tumor site itself.⁴⁷

There have been attempts at *in vivo* pretargeting using a variety of bioorthogonal click ligations. This biorthogonal reaction does not interfere with the biological system and must form a stable covalent linkage between functional groups at a reasonable rate even when concentrations are low.^{50, 51} Vugts et al. developed a pretargeting approach based on the Staudinger ligation reaction between an azide-bearing antibody and phosphine-containing probe labeled with ^{68}Ga , ^{89}Zr , ^{177}Lu , and ^{123}I , however the product could not be observed *in vivo* due to the reactions slow kinetics of the reaction.⁵² Rossin et al. were the first to develop a

pretargeting strategy based on the inverse electron demand Diels-Alder (IEDDA) reaction.⁵³ The IEDDA reaction proceeds with a fast rate without the need of a catalyst and displays the remarkably promising results among any other bioorthogonal reaction investigated in tumor pretargeting.^{54, 55} The reaction generally utilizes a TCO-labeled antibody and a tetrazine (Tz)-based radioligand.^{56, 57} The coupling is irreversible, and forms a stable pyridazine product after release of dinitrogen from the reaction intermediate.^{58, 59}

The IEDDA reaction is carried out in 4 steps: (1) the TCO-modified antibody is injected, (2) the modified antibody is given a few days to localize at the tumor site and clear from the blood, (3) a small Tz based radioligand is injected, and (4) an in vivo click reaction between the antibody and radioligand occurs at the tumor site.^{42, 60-64} This allows time for the antibody to accumulate at the site of interest, while also clearing from non-target organs, before injection of a radiolabeled coupling partner that reacts selectively with the antibody and allows rapid clearance of excess radioactivity.^{67, 68} The pharmacokinetics of small-molecule ligands enables the use of radioisotopes with short half-lives, such as ^{99m}Tc and ¹⁸⁸Re, and reduces radiation dose to nontarget organs. The isotope ^{99m}Tc was selected as an imaging radionuclide because of its exceptional 6.02 h half-life and γ -radiation component of 0.140 MeV allowing for SPECT imaging. Similarly, ¹⁸⁸Re is a beta emitter, 2.0 MeV β_{\max} , half-life: 17 hours, and is considered a radiotherapy analog to ^{99m}Tc. This isotope also possesses an imageable gamma of 0.155 MeV.⁶⁹

This chapter discusses the development of a pretargeted SPECT imaging approach that facilitates the rapid inverse electron demand [4+2] Diels-Alder cycloaddition reaction between a tetrazine-based radioligand and TCO-labeled antibody. The tetrazines used were tetrazine-NHS ester, and tetrazine-PEG₅-NHS ester (Figure 43, 44) Within the study, the following were

used: the SW1222 colorectal cancer cell line, the A33 antibody, and two gamma-emitting radiometals ^{99m}Tc and ^{188}Re as a model system. Ultimately, we have shown rapid and clear visualization of tumor tissue with excellent tumor-to-background activity concentration ratios using the in vivo cycloaddition methodology.

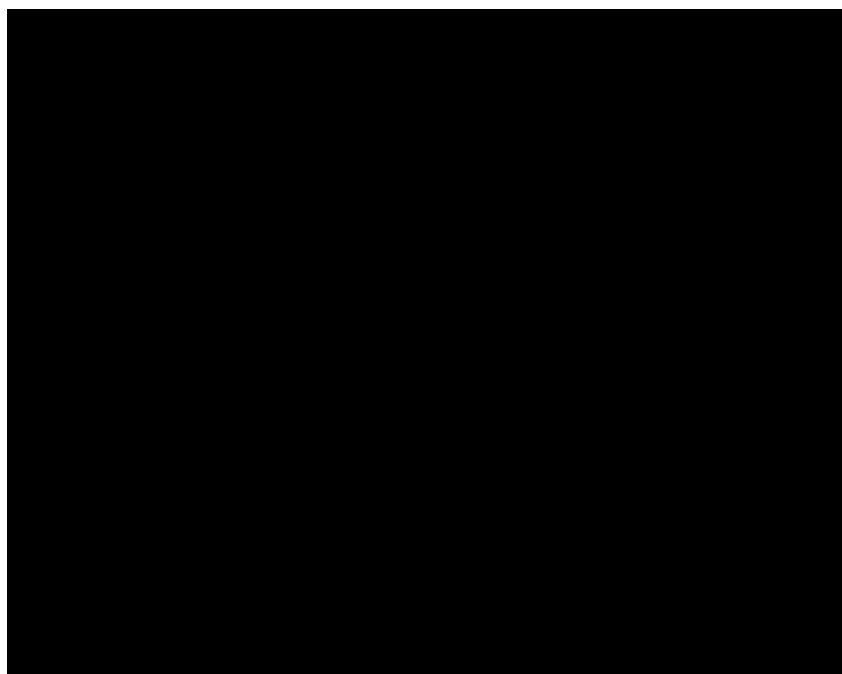


Figure 43. Structure of tetrazine-NHS ester (sh-Tz)

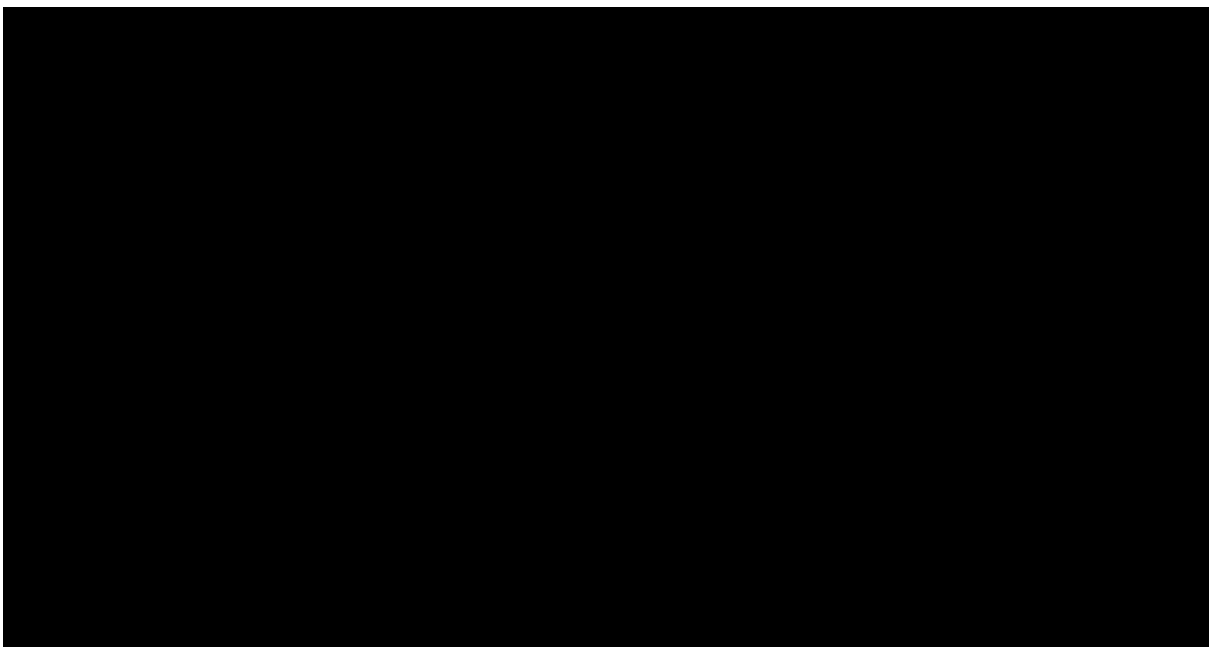


Figure 44. Structure tetrazine-PEG₅-NHS ester (PEG₅-Tz)

3.2. Materials

The ^{99m}Tc was obtained via Memorial Sloan Kettering Cancer Center, New York, New York, as Na^{99m}TcO₄, eluted from a ⁹⁹Mo/^{99m}Tc Generator. The ¹⁸⁸Re was obtained as Na¹⁸⁸ReO₄ was eluted from an ¹⁸⁸W/¹⁸⁸Re generator with 0.9% NaCl solution. The ¹⁸⁸W/¹⁸⁸Re generator was purchased from RadioMedix, Houston, Texas, USA. Activity measurements were obtained from an Atomic Products Corporation Atomlab 100 Dose Calibrator. The ligand, KYCAR, was purchased from United Peptide, Herndon, Virginia, USA. Tetrazine-NHS Ester (sh-Tz) and Tetrazine-PEG5-NHS Ester (Tz-PEG5) were purchased from BroadPharm, San Diego, California, USA. Isoflurane was purchased from Baxter Healthcare. Humanized A33 antibody was provided by the Ludwig Institute for Cancer Immunotherapy. All *in vivo* experiments were

performed according to protocols approved by the Memorial Sloan-Kettering Institutional Animal Care and Use Committee.

Methanol (MeOH), dimethyl sulfoxide (DMSO), N,N-diisopropylethyl amine (DIEA), HPLC-grade acetonitrile, trifluoroacetic acid (TFA), 0.9% NaCl solution were purchased from Fisher Scientific. Tin (II) tartrate 99%, tin (II) chloride dehydrate, and d- gluconic acid and all other chemicals were purchased from Fisher Scientific or Sigma Aldrich. Deionized water was obtained from a 0.22 μ m Millipore filtration system.

3.3. Synthesis

3.3.1. ReO-KYCAR

The KYCAR Ligand (0.0403 mmol) was dissolved in 500 μ L CH₃OH. The (Bu₄N)[ReOBr₄(H₂O)]•H₂O (0.0403 mmol) was dissolved in 500 μ L CH₃OH and added dropwise to the ligand and allowed to stir at 200 rpm for 10 minutes. Following stirring the solution was allowed to sit at room temperature for 30 minutes. The ReO-KYCAR (syn) product was analyzed and purified via HPLC. Yield 40%.

3.3.2. ^{99m}TcO-KYCAR

To a saline solution of ^{99m}Tc pertechnetate, KYCAR ligand (200 μ L, 0.00234 mmol solution) in saline was added. To that mixture tin(II) tartrate (40 μ L, 0.0221 mmol solution) in water was added and vortexed. The reaction mixture was then kept at 90°C for 10 minutes followed by sitting at room temperature for 30 minutes. The reaction mixture was then filtered through a 0.1 μ m syringe filter and analyzed via HPLC. Radiochemical Purity 99.9%.

3.3.3. $^{188}\text{ReO-KYCAR}$

To a saline solution of ^{188}Re perrhenate solution, tin(II) chloride (75 μL , 0.105 mmol solution) in water and d-gluconic acid (150 μL , 0.102 mmol solution) in water were added. The reaction mixture was vortexed and kept at 37°C for 30 minutes. To this the KYCAR ligand (150 μL , 0.03313 mmol solution) in saline was added, the reaction mixture was vortexed and kept at 37°C for 30 minutes. The solution was then filtered through a 0.1 μm syringe filter and analyzed via HPLC. Radiochemical Purity 99.9%.

3.3.4. Conjugation with Tetrazine-NHS ester and Tetrazine-PEG5-NHS ester

3.3.4.1. ReO-KYCAR-Sh-Tz and ReO-KYCAR-PEG5-Tz

0.013 mmol of purified, lyophilized ReO-KYCAR (syn) was dissolved in 100 μL DMSO. To that 0.0013 mmol of desired tetrazine construct in DMSO was added followed by an addition of 0.04 to 0.09 mmol of DIEA. The reaction was allowed to sit at room temperature for 30 minutes. The construct was then purified via preparative HPLC. The major peak was collected and lyophilized.

3.3.4.2. $^{99\text{m}}\text{TcO-KYCAR-Sh-Tz}$ and $^{99\text{m}}\text{TcO-KYCAR-PEG5-Tz}$

$^{99\text{m}}\text{TcO-KYCAR(syn)}$ (purified as described above) was dissolved in DMSO. To that 0.0007 mmol of desired tetrazine construct in DMSO was added followed by an addition of 0.0287 mmol DIEA. The reaction was allowed to react for 30 minutes at room temperature and purified via HPLC. The major fraction was collected and dried down by vacuum.

3.3.4.3. $^{188}\text{ReO-KYCAR-Sh-Tz}$ and $^{188}\text{ReO-KYCAR-PEG5-Tz}$

$^{188}\text{ReO-KYCAR}$ (syn) (purified as described above) was dissolved in DMSO. To that 0.0007 mmol of desired tetrazine construct in DMSO was added followed by an addition of 0.0287 mmol DIEA. The reaction was allowed to react for 30 minutes at room temperature and purified via HPLC. The major fraction was collected and dried down by vacuum.

3.3.5. A33 Modification with TCO-NHS

The A33 antibody was modified with transcyclooctene-NHS following the method of Zeglis et. al.⁶⁶ Briefly 5 mg A33 was dissolved in 500 μL PBS. The pH was adjusted to 8.8 – 8.9 using 0.1M NaHCO_3 . To this the adequate amount of TCO-NHS in N,N-dimethylformamide (25mg/mL) was added and the solution was mixed at 350 rpm for 1 hour at 25°C. Following incubation, the antibody was purified using a size-exclusion Sephadex G-25M PD-10 column (2.5 mL dead volume), and concentrated using centrifugal filtration units with a 50,000 molecular weight cut off.

3.4. HPLC Analysis

HPLC experiments were completed using a Varian Pro Star HPLC system. Complexes were analyzed and purified using a Waters Atlantis dc18 3 μm 100 Å column 4.6 x 150 mm. γ emissions were monitored using a Bicorn 2m2/2 NaI detector and Tennelec Minibin components. The software used for all HPLC systems was the ProStar WorkStation. The solvents used were ultra-pure deionized water with 0.1% trifluoroacetic acid (solvent A), and HPLC-grade acetonitrile with 0.1% trifluoroacetic acid (solvent B). Method: 20-30% B over 25 minutes

with a flow rate of 1 mL/minute. For all HPLC analyses the UV detection was monitored at 260 and 525 nm.

3.5. Mass Spectrometry Analysis

For cold rhenium compounds, mass spectral data were obtained from samples analyzed on an LCMS system comprised of an Agilent 1200 LC system coupled to an Agilent 6340 ion trap mass spectrometer. Samples were injected onto an Agilent Zorbax column (SB-C8, 5 μ M, 2.1 x 50 mm) using a linear gradient of 5-95% acetonitrile in water (0.5% formic acid) over 10 minutes. The samples were prepared by dissolving the ReO-KYCAR tetrazine samples in a water:acetonitrile solution (v:v, 450:50 μ L).

3.6. Proton NMR Analysis

1D proton and 2D COSY (correlation spectroscopy) NMR spectra were obtained from a Bruker Avance III 600 MHz with a TCI cryoprobe NMR spectrometer with chemical shift referenced to H₂O, at T=296 K. The ReO-KYCAR tetrazines (1-5 mg) was dissolved in an 800 μ L solution of 0.01 M HCl/D₂O 50:50 (v:v). The solution was then transferred to a 5 mm U-Thin NMR tube. 1D proton NMR spectra were collected at 8 scans. 2D cosy scans were collected at 2 scans, 256 increments.

3.7. Infrared Spectroscopy

Infrared spectra were obtained using a Perkin-Elmer Spectrum Two IR Spectrometer with attached UATR in the range of 500-4000 nm. Briefly a small amount of lyophilized sample was placed on the UATR and the appropriate pressure was applied.

3.8. LogD Studies

To determine the extinction coefficients the radioactive metal (^{99m}Tc , ^{188}Re) complexes dried via high vacuum system following synthesis. The product was reconstituted in PBS and placed into a micro centrifuge tube with an equal amount of 1 octanol. The samples were vortexed followed by centrifugation at 10,000 rpm for 5 minutes.

3.9. SPECT Imaging

Pretargeting SPECT imaging experiments were conducted on a NanoSPECT/CT Plus In Vivo Animal Imager. Athymic nude female mice 6-8 weeks old bearing subcutaneous SW1222 xenografts (right shoulder, 100 -150 mm³, 14-21 days post-inoculation) were administered 125 µg. A33-TCO (in 250 µL PBS) via tail vein injection. Prior to imaging mice were anesthetized by inhalation of a 2% isofluorane: oxygen gas mixture and placed on a scanner bed. SPECT data was obtained for each mouse (5 mice per time point) at 1 hour, 4 hour and 8 hour post injection. Following imaging mice were sacrificed. The following tissues were collected, blood, tumor, heart, lungs, liver, spleen, stomach, small intestines, large intestines, kidneys, muscle, bone, skin, thyroid, and gall bladder. The tissues were then counted on a Perkin Elmer Automatic Wizard γ counter and the %ID/g and were calculated and reported.

3.10. Biodistribution Studies

The ^{99m}Tc and ^{188}Re labelled KYCAR tetrazine complexes were evaluated for their biological distribution in healthy athymic nude female mice 6-8 weeks old. About 100 to 200 μCi (3.7×10^3 - 7.4×10^3 kBq) of the radiolabeled complex was injected intravenously into the mice via the tail vein. Mice were sacrificed 30 minutes, 1 hour, 2 hour, and 4 hour post injection; 5 mice per time point. The following tissues were collected, blood, heart, lungs, liver, spleen, stomach, small intestines, large intestines, kidneys, muscle, bone, skin, thyroid, and gall bladder. The tissues were then counted on a Perkin Elmer Automatic Wizard γ counter and the %ID/g were calculated and reported.

Blood half-life studies were completed by injecting 100 μCi to 200 μCi (3.7×10^3 - 7.4×10^3 kBq) of the radiolabeled complex into healthy athymic nude female mice 6-8 weeks old, intravenously via the tail vein. Mice were sacrificed 5 minutes, 15 minutes, 30 minutes, and 1 hour post injection; 4 mice per time point. Terminal blood draws were collected via cardiac puncture. The tissues were then counted on a Perkin Elmer Automatic Wizard γ -counter and the percent injected dose per gram (%ID/g) were calculated and reported.

3.11. Results and Discussion

3.11.1. Synthesis of $^{99m}\text{TcO-KYCAR}$, $^{188}\text{ReO-KYCAR}$, and ReO-KYCAR tetrazines

The reaction of ReO-KYCAR with either short-tetrazine NHS ester or PEG_5 -tetrazine in the presence of DIEA results in one major product. The amine found on the side chain of KYCAR's

lysine is deprotonated by the DIEA producing a NH_2^- . This nucleophile then attacks the carbonyl of the tetrazine resulting in the conjugation of the tetrazine to the ligand and NHS ester as a byproduct (Figure 45). It is theoretically possible that the conjugation could occur at the guanidinium group of the arginine, however it is highly unlikely due to steric hindrances.

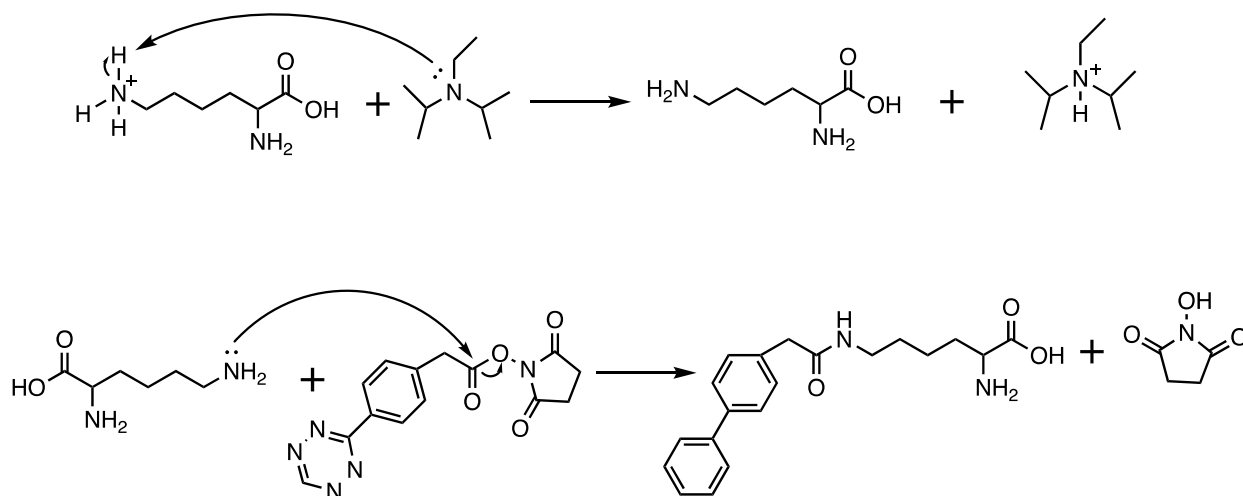


Figure 45. Lysine-tetrazine Reaction Mechanism

3.11.2. Reversed phase HPLC Analysis and Mass Spectroscopy

Following the synthesis of ReO-KYCAR with Sh-tetrazine the reaction mixture was purified via reversed phased HPLC (Figure 46). The major fraction was collected and lyophilized.

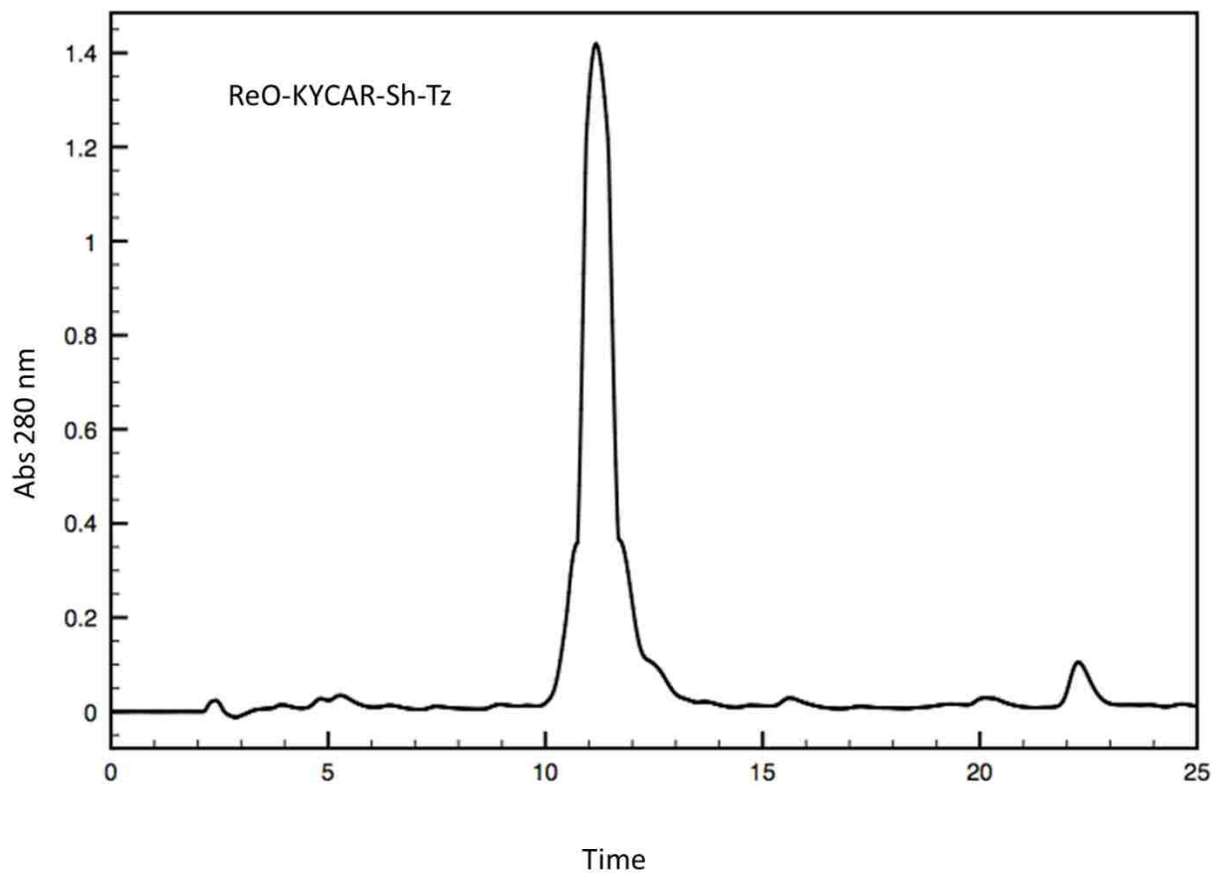


Figure 46. HPLC of ReO-KYCAR-Sh-Tz showing one major peak.

The lyophilized sample was then submitted for mass spectral analysis where it was determined that the collected product carried the appropriate molecular ion $[M + H]^+$ peak at m/z 1038 (Figure 47) which corresponds to the exact mass of 1037.30 g/mol.

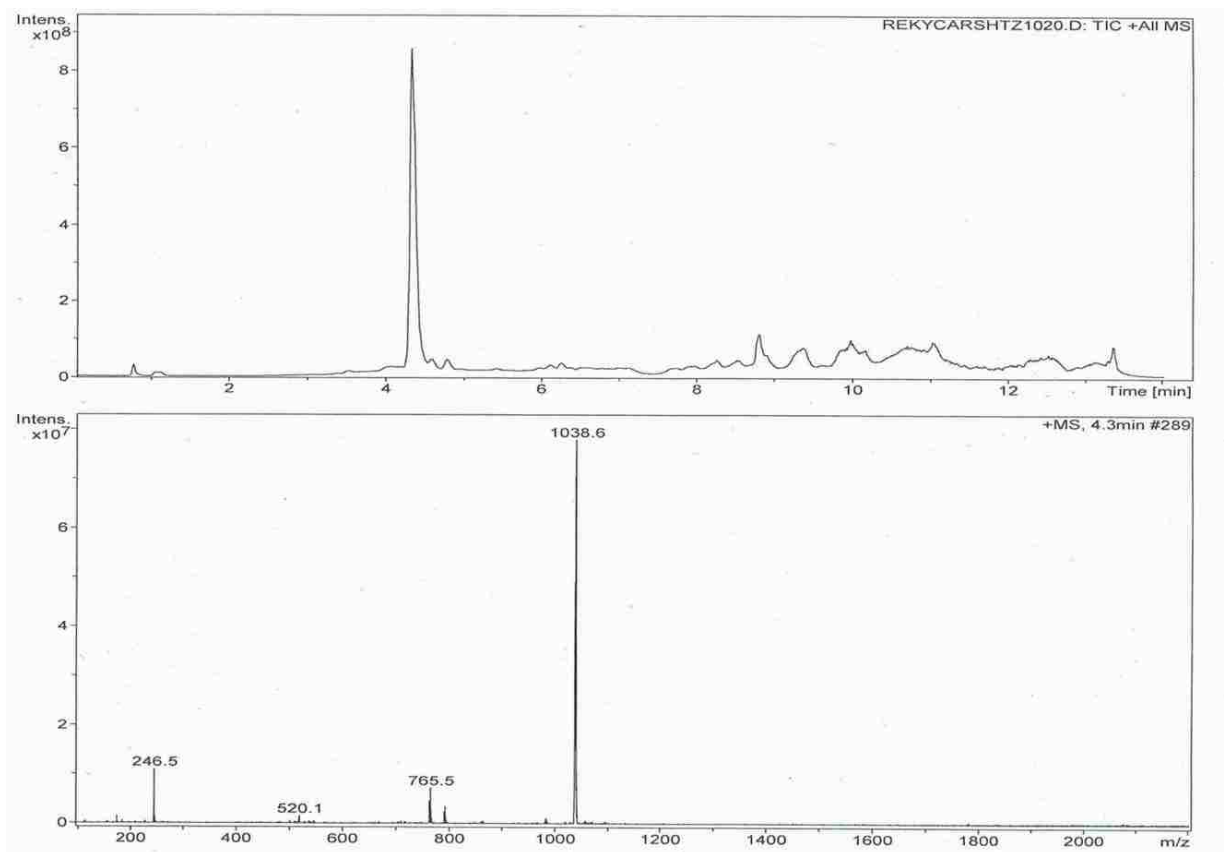


Figure 47. Mass Spectroscopy of ReO-KYCAR-Sh-Tz molecular ion $[M + H]^+$ peak at m/z 1038 which corresponds to an exact mass of 1037.30 g/mol.

Similarly, the ReO-KYCAR-PEG₅-Tz was purified viz HPLC (Figure 48) and the lyophilized product was analyzed after mass spectral submission (Figure 49). The mass spectroscopy also shows a pure sample with the appropriate molecular ion $[M + H]^+$ peak at m/z 1329, corresponding to an exact mass of 1328.47 g/mol

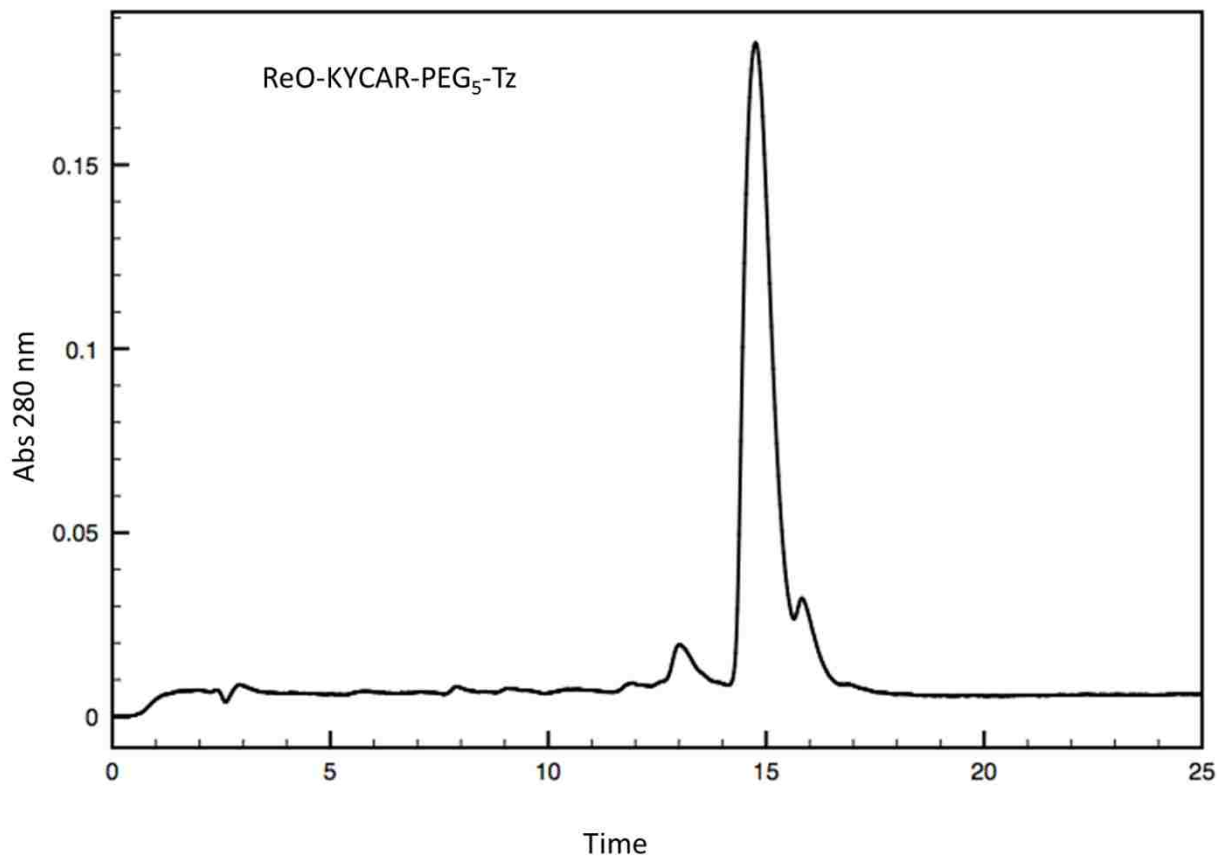


Figure 48. HPLC of ReO-KYCAR-PEG5-Tz showing one major peak

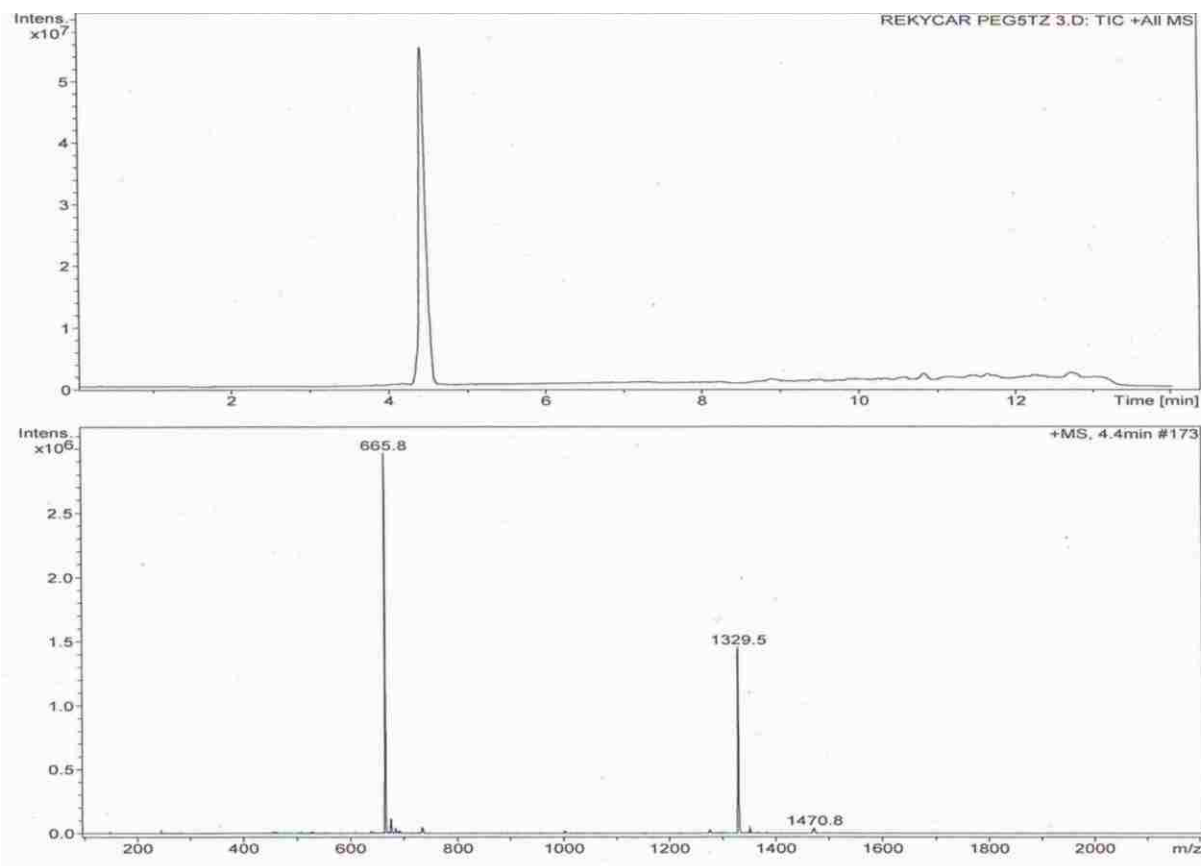


Figure 49. Mass Spectroscopy of ReO-KYCAR-PEG₅-Tz molecular ion [M + H]⁺ peak at *m/z* 1329 which corresponds to an exact mass of 1328.47 g/mol.

3.11.2.1. Coelution studies

To correlate the macroscopic Re product with the trace level ^{99m}Tc and ¹⁸⁸Re products, coelutions of the two materials were HPLC analyzed. Due to the increased stability of the ^{99m}Tc products they were chosen to perform coelution test. The ReO-KYCAR-Sh-Tz/^{99m}TcO-KYCAR-Sh-Tz coelution (Figure 59) shows the macroscopic rhenium product eluting between 16 and 18.5 minutes, and the tracer technetium product eluting between 16.5 and 19 minutes.

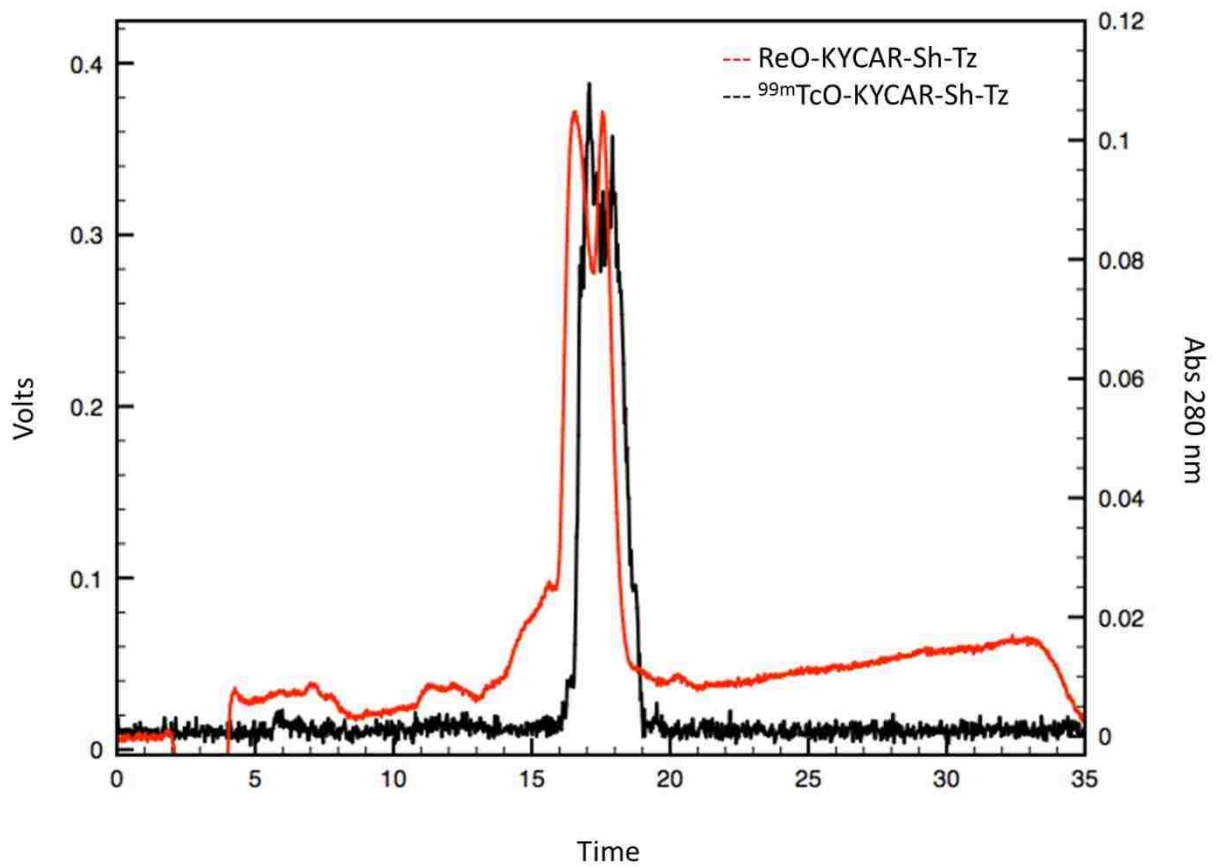


Figure 50. Coelution of ReO-KYCAR-Sh-Tz and ^{99m}TcO-KYCAR-Sh-Tz

ReO-KYCAR-PEG₅-Tz was then coeluted with ^{99m}TcO-KYCAR-PEG₅-Tz (Figure 51). Comparable to the Sh-Tz system the macroscopic rhenium elutes between 18 and 24 minutes and the technetium product elutes between 19 and 24 minutes. Here it is observed that the products elute with multiple peaks. This is due to the interaction of the bulky PEG₅ complex

with the column. This phenomenon is less observed with the cold rhenium due to its macroscopic nature.

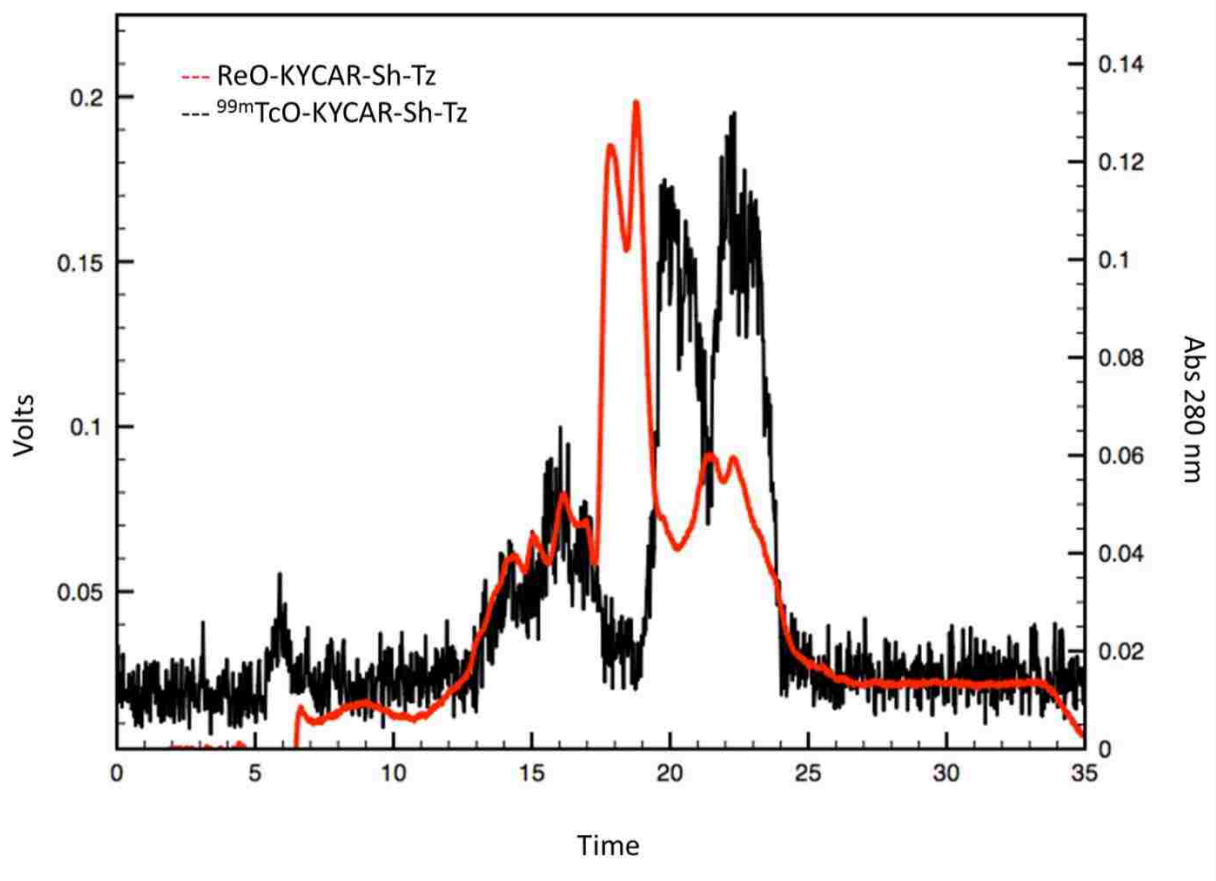


Figure 51. Coelution of ReO-KYCAR-PEG5-Tz and ^{99m}TcO-KYCAR-PEG5-Tz

3.11.3. Infrared Spectroscopy

After conjugation with the Sh-Tz the infrared spectra of ReO-KYCAR-Sh-Tz (Figure 52) retains the Re=O stretching frequency around 1000 cm^{-1} . However, it is slightly obscured by the stretching frequencies of the compound's secondary amide C=O amine III band. Overall the indication of a successful conjugation lies in the change in intensities in the various functional groups. Most noticeable is the phenol, carboxylic acid O-H and amine N-H stretching frequencies, 2800 cm^{-1} - 3500 cm^{-1} , which exhibits a medium frequency. This is also observed at 1665 cm^{-1} and 1655 cm^{-1} , a very strong intensity, which correspond to the increase in the amount of C=N and C=C bonds within the compound.

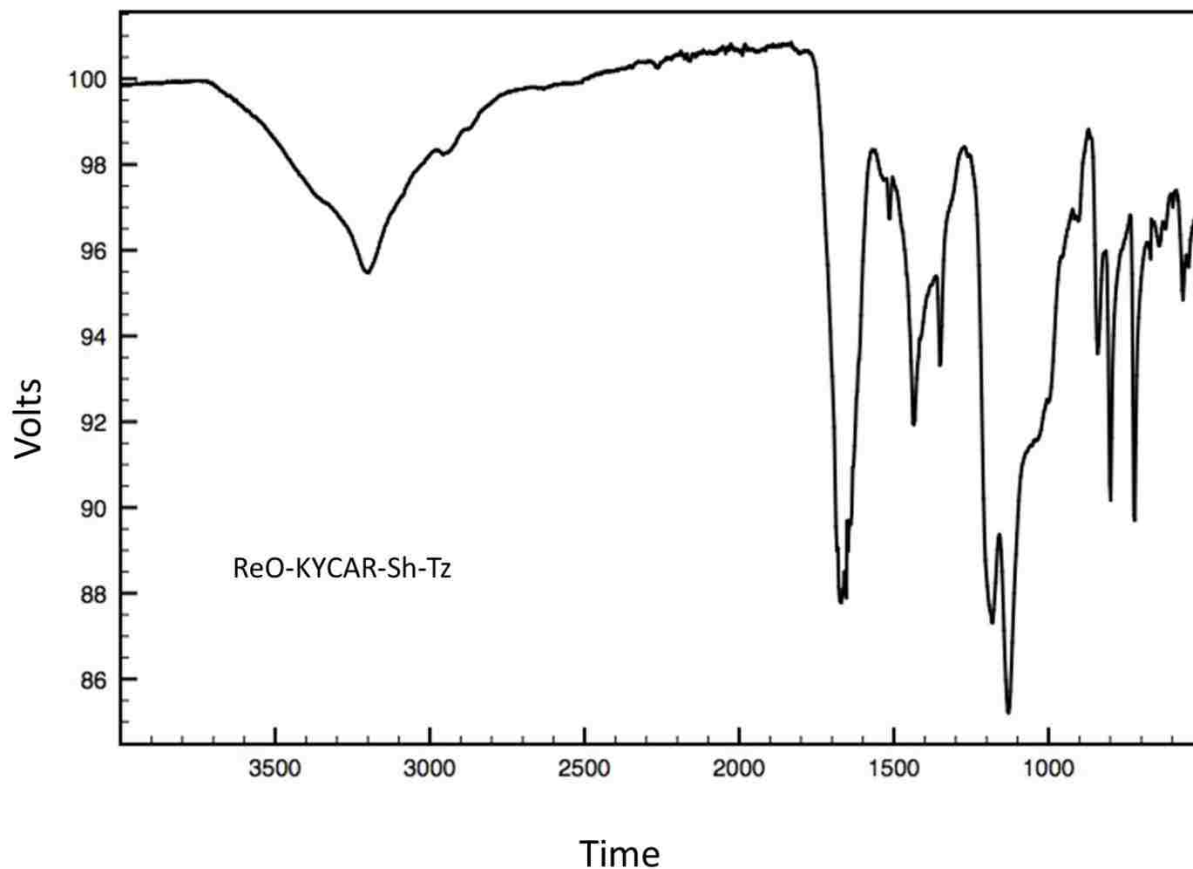


Figure 52. Infrared Spectra of ReO-KYCAR-Sh-Tz

The infrared spectra of ReO-KYCAR-PEG₅-Tz exhibit a very similar fingerprint to that of ReO-KYCAR-Sh-Tz in the observation of the intensities of the frequencies. However, ReO-KYCAR-PEG₅-Tz can be distinguished by the C-H fingerprint at a stretching frequency of 2880 cm^{-1} – 2930 cm^{-1} (Figure 53)

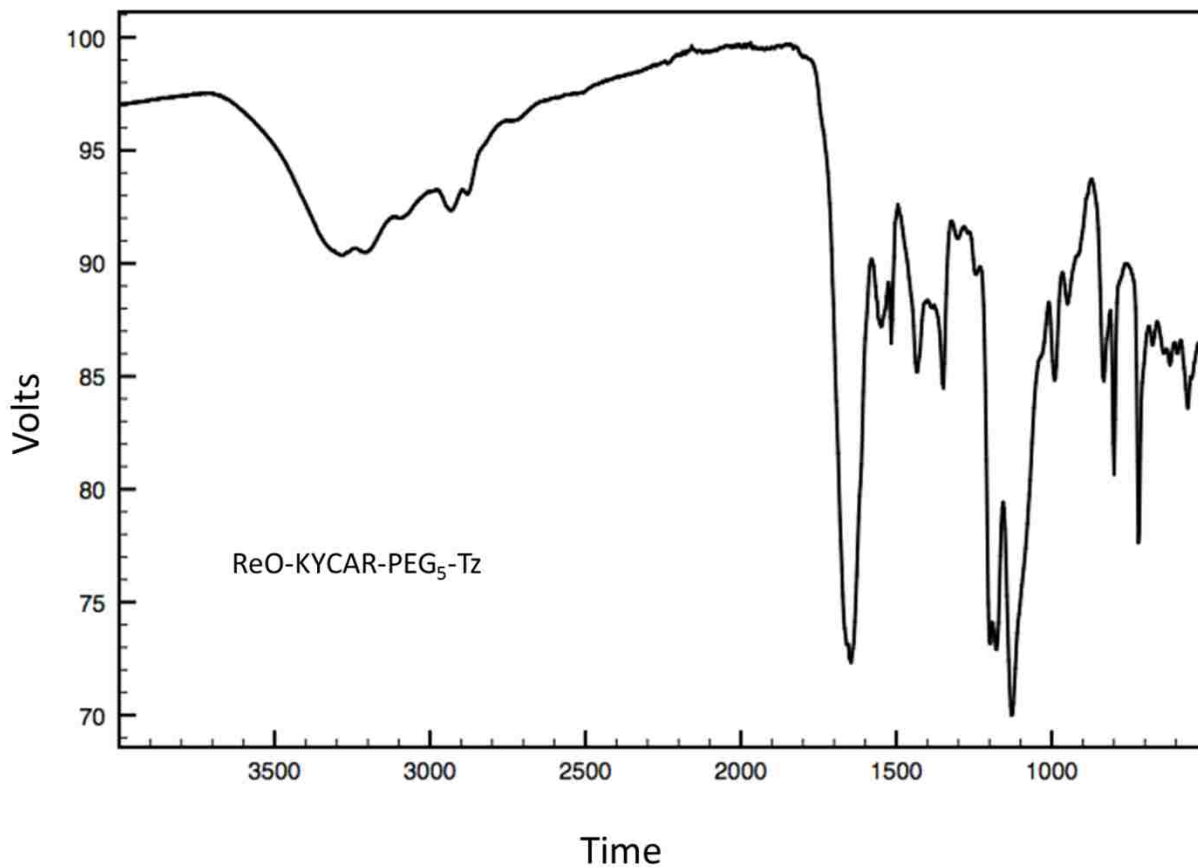


Figure 53. Infrared Spectra of ReO-KYCAR-PEG5-Tz

3.11.4. Biology

To obtain a baseline of distribution of the newly conjugated complex *in vivo* the complexes we injected in PBS into healthy athymic nude female mice. The biological distribution of ^{99m}TcO-KYCAR-Sh-Tz is tabulated in table 15 and shown in Figure 54.

%ID/g \pm S.D.				
Organ	30 min	1 hr	2 hr	4 hr
Blood	0.38 \pm 0.03	0.47 \pm 0.28	2.76 \pm 5.49	0.28 \pm 0.02
Heart	0.28 \pm 0.7	0.23 \pm 0.06	0.27 \pm 0.05	0.17 \pm 0.06
Lungs	2.05 \pm 0.21	1.72 \pm 0.49	2.21 \pm 1.18	1.14 \pm 0.60
Liver	1.10 \pm 1.01	1.41 \pm 0.18	1.90 \pm 0.64	1.58 \pm 0.74
Spleen	0.68 \pm 0.34	0.94 \pm 0.37	0.82 \pm 0.44	0.83 \pm 0.24
Stomach	0.62 \pm 0.12	0.49 \pm 0.31	0.43 \pm 0.24	0.91 \pm 1.00
Small Intestine	25.45 \pm 16.06	11.13 \pm 12.88	2.87 \pm 3.58	0.80 \pm 0.38
Large Intestine	0.11 \pm 0.04	0.27 \pm 0.21	37.05 \pm 15.15	64.43 \pm 30.15
Kidneys	3.40 \pm 1.30	1.57 \pm 0.68	1.53 \pm 0.45	0.96 \pm 0.17
Muscle	1.21 \pm 1.48	0.16 \pm 0.14	0.68 \pm 1.24	0.48 \pm 0.74
Bone	0.48 \pm 0.23	0.18 \pm 0.14	0.12 \pm 0.13	0.11 \pm 0.09
Skin	0.83 \pm 0.38	0.61 \pm 0.14	0.31 \pm 0.07	0.21 \pm 0.12
Thyroid	3.36 \pm 1.48	12.86 \pm 7.42	11.91 \pm 5.08	8.02 \pm 4.65
Gall Bladder	1133.91 \pm 274.09	1879.90 \pm 2549.34	1020.63 \pm 1502.49	171.40 \pm 240.27

Table 15. Biodistribution of $^{99m}\text{TcO-KYCAR-Sh-Tz}$. The results are reported in %ID/g. Shows that the activity travels through the gastrointestinal track.

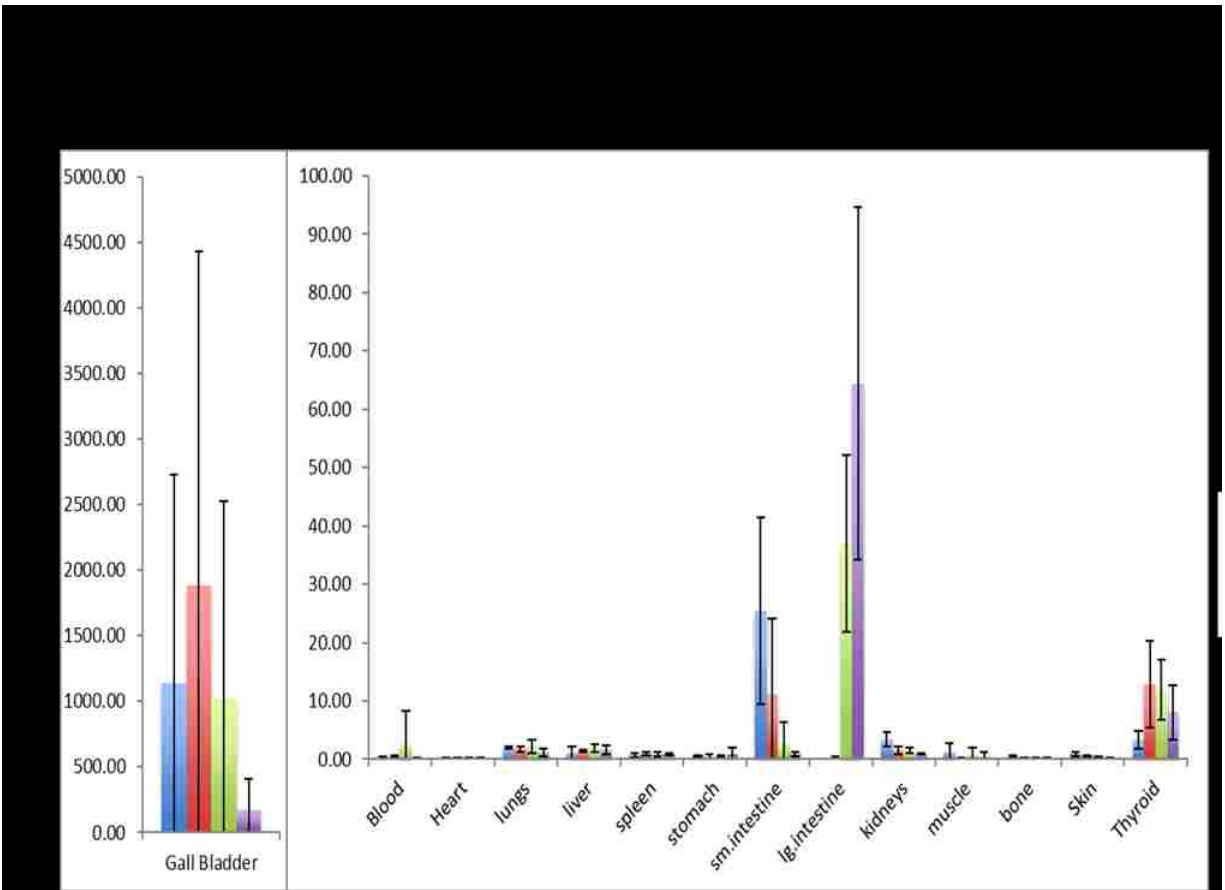


Figure 54. Biodistribution of $^{99m}\text{TcO-KYCAR-Sh-Tz}$. The results are reported in %ID/g. Shows that the activity travels through the gastrointestinal track.

Thirty minutes post injection the large majority of the uptake is found in the small intestines (25.45 ± 16.06 %ID/g). There is a noticeable decrease in small intestine uptake (11.13 ± 12.88 %ID/g) after one hour, followed by eventual complete depletion. Simultaneously as depletion occurred in the small intestines uptake increased in the large intestines (from 0.27 ± 0.21 %ID/g at 1 hour to 37.05 ± 15.15 %ID/g at 2 hours). The activity found in the large

intestines continues to increase at 4 hours post injection (64.43 ± 30.15 %ID/g). These observed trends matched the *in vitro* studies showing the lipophilicity of the complex ($\log D = -0.975$). There is a slight uptake and depletion found in the thyroid, which could correlate to some decomposition of the complex to $^{99m}\text{TcO}_4^-$. Overall the complex shows favorable stability *in vivo* showing no inexplicable uptake.

Organ	%ID/g ±S.D.			
	30 min	1 hr	2 hr	4 hr
Blood	1.48 ± 0.20	1.49 ± 0.22	0.88 ± 0.11	3.86 ± 5.57
Heart	0.42 ± 0.07	0.49 ± 0.08	0.28 ± 0.04	0.45 ± 0.23
Lungs	1.07 ± 0.18	2.10 ± 1.68	0.85 ± 0.18	1.27 ± 0.70
Liver	1.70 ± 0.37	1.72 ± 0.14	1.17 ± 0.11	1.72 ± 0.67
Spleen	0.62 ± 0.06	0.88 ± 0.13	0.65 ± 0.13	0.85 ± 0.31
Stomach	16.36 ± 10.24	18.04 ± 4.98	8.67 ± 2.34	15.12 ± 8.97
Small Intestine	54.52 ± 33.31	45.06 ± 39.93	1.28 ± 0.34	2.77 ± 1.85
Large Intestine	0.27 ± 0.06	0.44 ± 0.15	60.73 ± 27.32	82.23 ± 33.28
Kidneys	2.21 ± 0.25	2.10 ± 0.27	1.73 ± 0.34	1.96 ± 0.34
Muscle	0.30 ± 0.12	0.76 ± 0.31	0.27 ± 0.08	0.96 ± 1.14
Bone	0.48 ± 0.14	0.49 ± 0.06	0.42 ± 0.08	0.59 ± 0.16
Skin	0.78 ± 0.26	0.78 ± 0.16	0.51 ± 0.15	0.95 ± 0.29
Thyroid	87.43 ± 18.56	138.0 ± 64.57	126.89 ± 28.06	154.53 ± 103.63
Gall Bladder	1267.08 ± 667.89	478.55 ± 486.75	457.10 ± 513.59	337.33 ± 169.51

Table 16. Biodistribution of $^{188}\text{ReO-KYCAR-Sh-Tz}$. The results are reported in %ID/g. Shows that the activity travels through the gastrointestinal track. Also shows some decomposition to $^{188}\text{ReO}_4^-$ through stomach and thyroid accumulation.

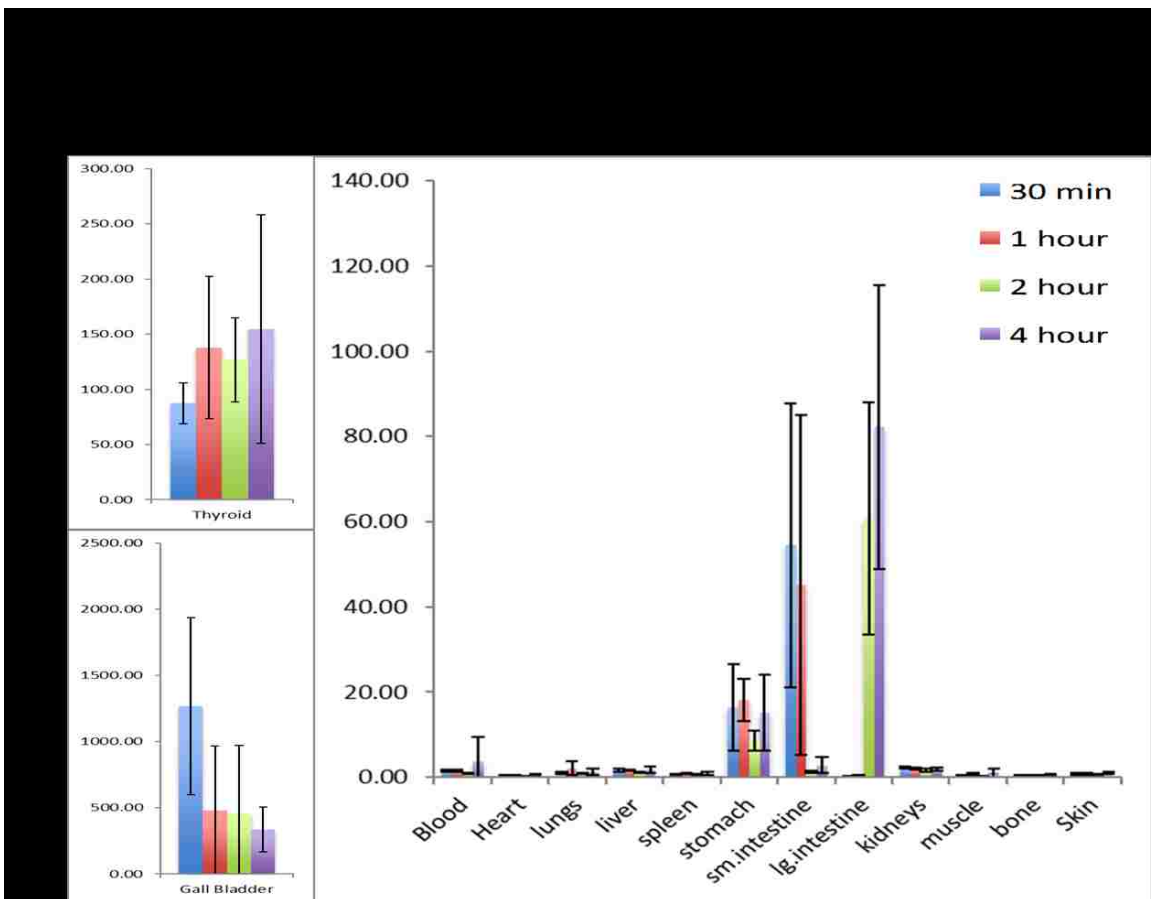


Figure 55. Biodistribution of $^{188}\text{ReO-KYCAR-Sh-Tz}$. The results are reported in %ID/g. Shows that the activity travels through the gastrointestinal track. Also shows some decomposition to $^{188}\text{ReO}_4^-$ through stomach and thyroid accumulation.

The biological distribution of $^{188}\text{ReO-KYCAR-Sh-Tz}$ is tabulated in table 16 and shown in Figure 55. The $^{188}\text{ReO-KYCAR-Sh-Tz}$ complex behaves similarly to the technetium complex. There is very little uptake seen in most organs which mostly indicates rapid excretion. *In vitro* studies show that the compound is slightly lipophilic ($\log D = -0.967$). This is observed by the uptake into the small intestines 30 minutes (54.52 ± 33.31 %ID/g), and 1 hour (45.06 ± 39.93 %ID/g) post injection. Followed by uptake in the large intestines at 2 hours (60.73 ± 27.32 %ID/g)

%ID/g) and 4 hours post injection (82.23 ± 33.28 %ID/g). Unlike the technetium complex there is a slight stomach uptake and retention of the rhenium complex, which remains constant (16.36 ± 10.24 %ID/g at 30 minutes to 15.12 ± 8.97 %ID/g at 4 hours). The uptake and retention in the stomach is indicative of absorption of free $^{188}\text{ReO}_4^-$. Another observation of decomposition within the compound is the uptake in the thyroid, (87.43 ± 18.56 %ID/g and 30 minutes to 154.53 ± 103.63 %ID/g at 4 hours).

The biological distribution of $^{99m}\text{TcO-KYCAR-PEG}_5\text{-Tz}$ is tabulated in table 17 and shown in Figure 56. Compared to the biological distribution of the technetium complex with Sh-Tz the uptake in the organs as a whole is increased. Despite the increased hydrophilicity of this compound ($\log D = -1.83$) the excretion route remains through the gastrointestinal tract. Stomach uptake and retention remains (56.17 ± 11.92 %ID/g at 30 minutes to 54.13 ± 38.51 %ID/g at 2 hours). Followed by a shift to the large intestines at 4 hours (70.23 ± 9.90 %ID/g). An increased uptake is seen in the thyroid (37.46 ± 28.31 %ID/g at 30 minutes to 387.09 ± 80.29 %ID/g at 4 hours) indicating possible decomposition to pertechnetate.

Organ	%ID/g ±S.D.			
	30 min	1 hr	2 hr	4 hr
Blood	2.19 ± 0.49	3.99 ± 1.47	2.27 ± 0.39	1.45 ± 0.21
Heart	0.92 ± 0.30	1.05 ± 0.21	0.88 ± 0.25	0.48 ± 0.09
Lungs	2.18 ± 1.46	2.82 ± 0.73	2.32 ± 1.10	1.30 ± 0.31
Liver	3.81 ± 0.77	5.55 ± 1.56	3.31 ± 0.95	1.55 ± 0.29
Spleen	1.90 ± 1.75	1.43 ± 0.82	1.62 ± 1.28	0.61 ± 0.11
Stomach	6.65 ± 2.43	7.60 ± 3.83	8.42 ± 2.72	5.14 ± 1.28
Small Intestine	56.17 ± 11.92	42.97 ± 18.03	54.13 ± 38.51	1.92 ± 1.30
Large Intestine	0.79 ± 0.53	0.91 ± 0.45	8.19 ± 6.29	70.23 ± 9.90
Kidneys	3.55 ± 0.57	4.88 ± 0.71	3.56 ± 0.45	3.57 ± 0.70
Muscle	0.67 ± 0.38	2.05 ± 2.81	0.55 ± 0.23	1.10 ± 1.01
Bone	1.42 ± 1.29	0.99 ± 0.41	0.95 ± 0.35	0.58 ± 0.12
Skin	1.38 ± 0.29	1.76 ± 0.23	0.76 ± 0.08	0.64 ± 0.19
Thyroid	37.46 ± 28.31	86.68 ± 33.07	432.32 ± 188.46	387.09 ± 80.29
Gall Bladder	1033.30 ± 627.92	1197.95 ± 1638.93	9161.18 ± 8937.72	1564.13 ± 2850.01

Table 17. Biodistribution of $^{99m}\text{TcO-KYCAR-PEG}_5\text{-Tz}$. The results are reported in %ID/g. Shows that the activity travels through the gastrointestinal track. Also shows some decomposition to $^{99m}\text{TcO}_4^-$ over time through slow thyroid accumulation.

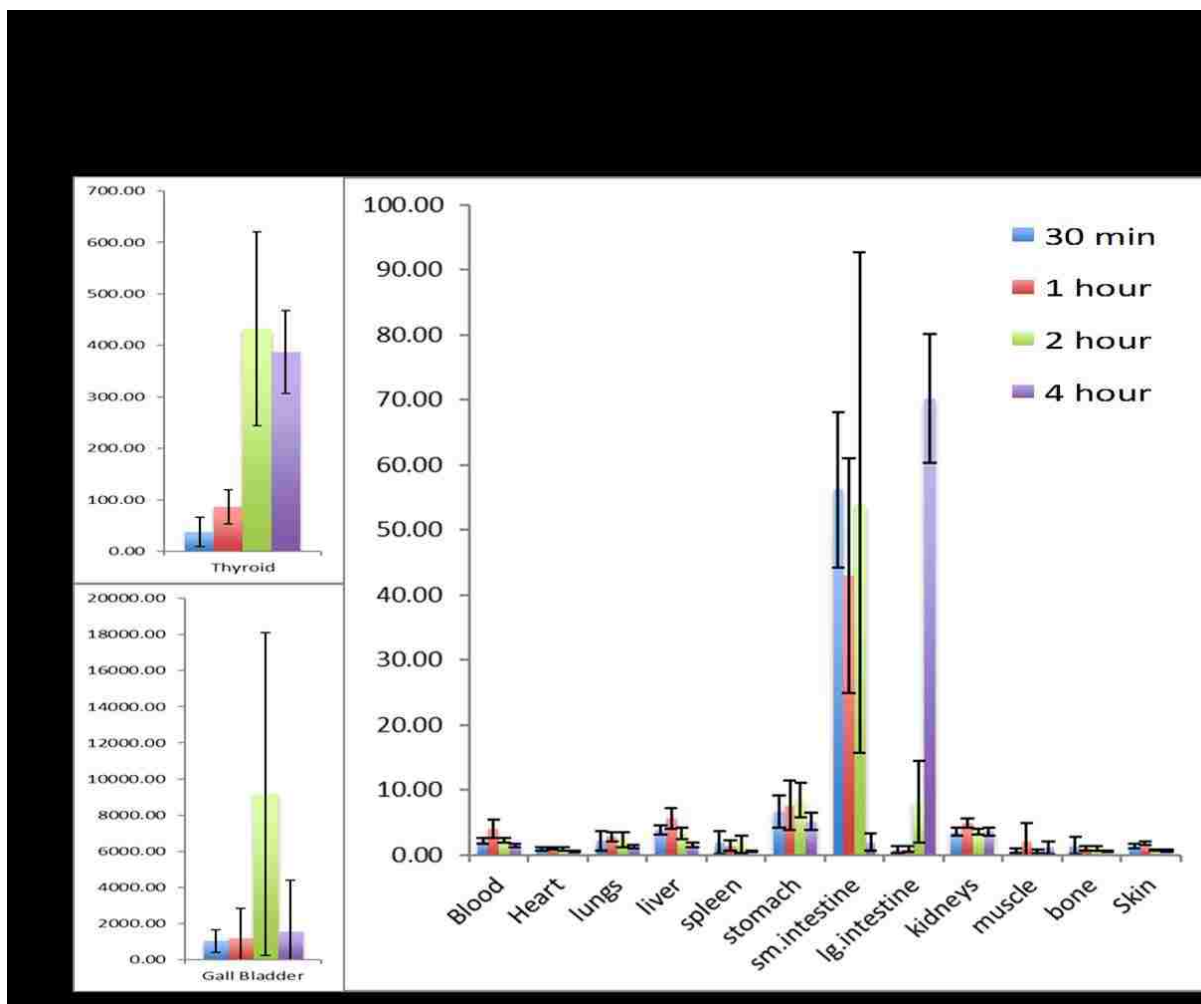


Figure 56. Biodistribution of ^{99m}TcO-KYCAR-PEG₅-Tz. The results are reported in %ID/g. Shows that the activity travels through the gastrointestinal track. Also shows some decomposition to ^{99m}TcO₄⁻ over time through slow thyroid accumulation.

The biological distribution of ¹⁸⁸ReO-KYCAR-PEG₅-Tz is tabulated in table 18 and shown in Figure 57. Excretion through the gastrointestinal tract is observed with the ¹⁸⁸ReO-KYCAR-PEG₅-Tz complex despite the hydrophilic nature (logD= -1.69). Uptake begins in the small intestines (31.26 ± 23.02 %ID/g at 30 minutes to 42.47 ± 43.64 %ID/g at 1 hour). This is followed by a shift into the large intestines (52.47 ± 26.99 %ID/g at 2 hours to 65.09 ± 34.49 %ID/g at 4

hours). Decomposition is observed in the thyroid (124.63 ± 27.34 %ID/g at 30 minutes to 161.72 ± 75.86 %ID/g at 4 hours) and also in the stomach (10.84 ± 4.26 %ID/g at 30 minutes to 8.44 ± 6.18 at 4 hours). However, there is insignificant uptake found in all other organs.

Organ	%ID/g \pm S.D.			
	30 min	1 hr	2 hr	4 hr
Blood	1.98 \pm 0.32	2.16 \pm 0.16	1.18 \pm 0.30	1.14 \pm 0.70
Heart	0.61 \pm 0.11	0.63 \pm 0.05	0.40 \pm 0.15	0.39 \pm 0.25
Lungs	1.40 \pm 0.21	1.49 \pm 0.13	1.04 \pm 0.29	1.30 \pm 1.32
Liver	3.24 \pm 0.88	2.61 \pm 0.60	1.51 \pm 0.27	1.43 \pm 0.68
Spleen	0.97 \pm 0.16	1.11 \pm 0.18	0.72 \pm 0.13	1.03 \pm 0.91
Stomach	10.84 \pm 4.26	23.44 \pm 12.70	10.86 \pm 6.07	8.44 \pm 6.18
Small Intestine	31.26 \pm 23.02	42.47 \pm 43.64	1.58 \pm 1.16	2.99 \pm 4.99
Large Intestine	0.46 \pm 0.10	0.59 \pm 0.25	52.47 \pm 26.99	65.09 \pm 34.49
Kidneys	2.79 \pm 0.45	2.52 \pm 0.18	2.00 \pm 0.22	2.12 \pm 0.56
Muscle	1.26 \pm 0.51	1.15 \pm 0.33	0.80 \pm 0.47	0.98 \pm 0.85
Bone	0.85 \pm 0.15	1.01 \pm 0.09	0.61 \pm 0.12	0.61 \pm 0.35
Skin	1.03 \pm 0.26	1.01 \pm 0.13	0.70 \pm 0.14	0.67 \pm 0.46
Thyroid	124.63 \pm 27.34	233.39 \pm 127.99	190.49 \pm 69.59	161.72 \pm 75.86
Gall Bladder	1218.70 \pm 638.01	1384.32 \pm 938.22	263.70 \pm 424.31	134.23 \pm 147.58

Table 18. Biodistribution of $^{188}\text{ReO-KYCAR-PEG}_5\text{-Tz}$. The results are reported in %ID/g. Shows that the activity travels through the gastrointestinal track. Also shows some decomposition to $^{188}\text{ReO}_4^-$ through stomach and thyroid accumulation.

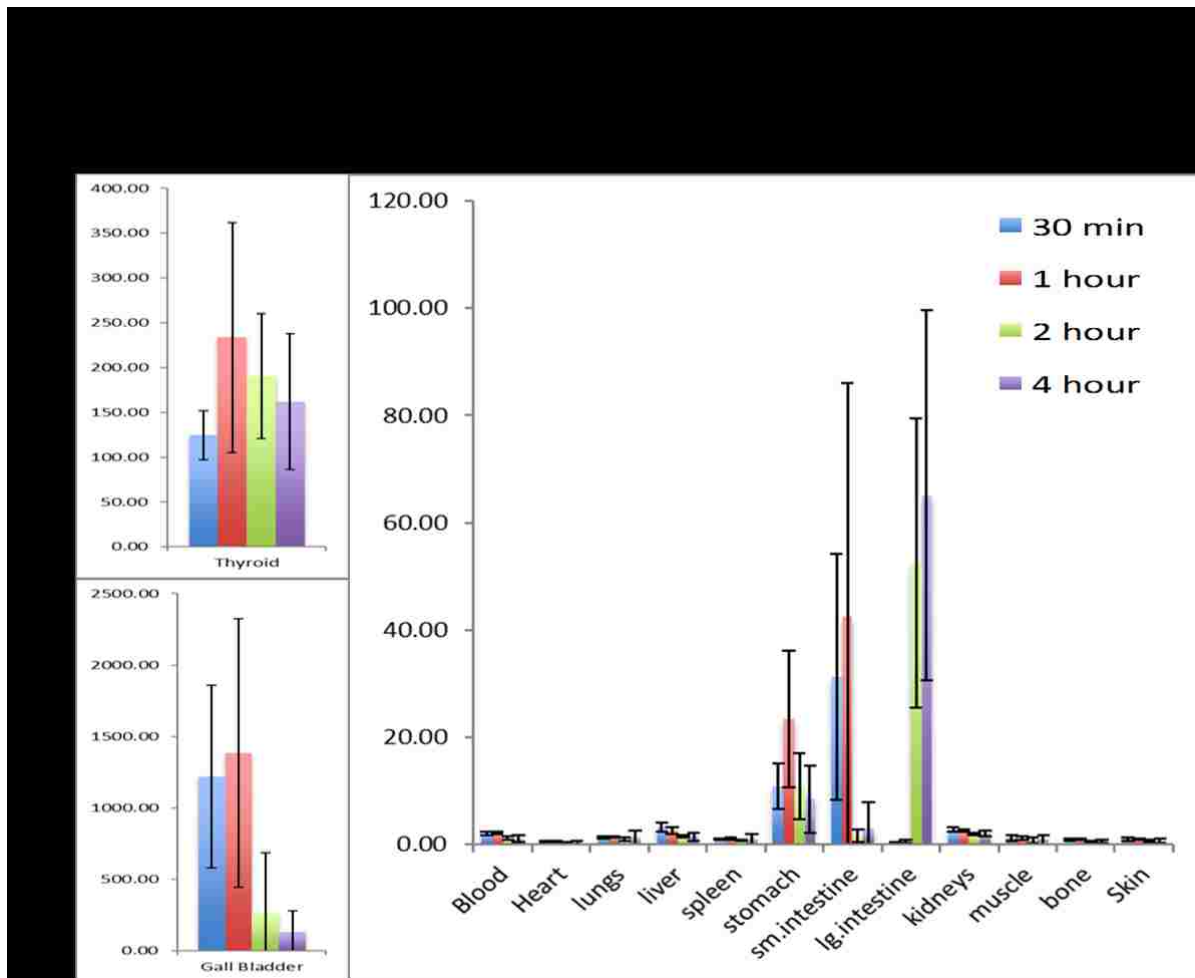


Figure 57. Biodistribution of $^{188}\text{ReO-KYCAR-PEG}_5\text{-Tz}$. The results are reported in %ID/g. Shows that the activity travels through the gastrointestinal track. Also shows some decomposition to $^{188}\text{ReO}_4^-$ through stomach and thyroid accumulation.

Throughout all biological distributions in healthy mice the clearance within each system seems to be rapid which show promise for reducing dose to non-target organs. Regardless of

the change in the partition coefficients the route of excretion appears to remain through the gastrointestinal tract. There is slight decomposition of the complexes found throughout each system, though it is more prevalent in the ^{188}Re systems.

To observe the rate at which $^{99}\text{TcO-KYCAR-PEG}_5\text{-Tz}$ were removed from the bloodstream, blood half-life studies were completed. Using a two phase decay, via Prism, the two components of the blood half-life were obtained. The fast component was determined to be 0.024 minutes which means the majority of the compound is removed from the blood in <30 seconds. The slow component was determined to be 4.597 minutes which show that the remainder of the construct that is in the blood stream circulates for about 5 additional minutes.

3.11.4.1. Biological Studies in Tumored Mice

In order to observe the stability of $^{99\text{m}}\text{TcO-KYCAR-PEG}_5\text{-Tz-A33-TCO}$ and the effectiveness of the entire moiety through tumor uptake, the $^{99\text{m}}\text{TcO-KYCAR-PEG}_5\text{-Tz}$ was clicked to A33-TCO *ex vivo* prior to injection into SW1222 xenografted mice. This is called “pre-clicked”, here the antibody drives the biodistribution. The biological distribution of the pre-clicked $^{99\text{m}}\text{TcO-KYCAR-PEG}_5\text{-Tz-A33-TCO}$ is tabulated in table 19 and shown in Figure 58.

%ID/g \pm S.D.			
Organ	1 hr	4 hr	8 hr
Blood	32.95 \pm 6.08	35.71 \pm 7.27	38.62 \pm 12.03
Tumor	9.26 \pm 6.25	32.76 \pm 4.21	31.05 \pm 9.78
Heart	7.68 \pm 1.40	11.63 \pm 2.03	12.79 \pm 3.87
Lungs	13.55 \pm 3.03	17.00 \pm 5.41	14.75 \pm 4.83
Liver	11.16 \pm 3.32	10.43 \pm 1.97	12.66 \pm 5.05
Spleen	6.88 \pm 2.37	8.18 \pm 1.58	11.46 \pm 5.67
Stomach	1.27 \pm 0.29	2.22 \pm 0.92	3.06 \pm 1.20
Small Intestine	7.11 \pm 3.68	4.91 \pm 0.64	4.34 \pm 1.15
Large Intestine	0.80 \pm 0.26	3.02 \pm 0.71	10.82 \pm 3.64
Kidneys	10.61 \pm 2.51	11.15 \pm 2.08	13.67 \pm 3.81
Muscle	1.19 \pm 0.82	1.27 \pm 0.30	4.44 \pm 2.39
Bone	4.59 \pm 0.78	5.27 \pm 1.32	5.22 \pm 2.14
Skin	1.74 \pm 0.40	3.69 \pm 1.20	5.09 \pm 2.38
Thyroid	10.89 \pm 4.11	28.41 \pm 19.14	33.73 \pm 14.11
Gall Bladder	61.45 \pm 71.20	108.86 \pm 52.91	97.31 \pm 47.12

Table 19. Pre-clicked Biodistribution of $^{99m}\text{TcO-KYCAR-PEG}_5\text{-Tz-A33-TCO}$. The results are reported in %ID/g. Shows retention of activity in the blood due to long circulation time. Also shows significant tumor uptake.

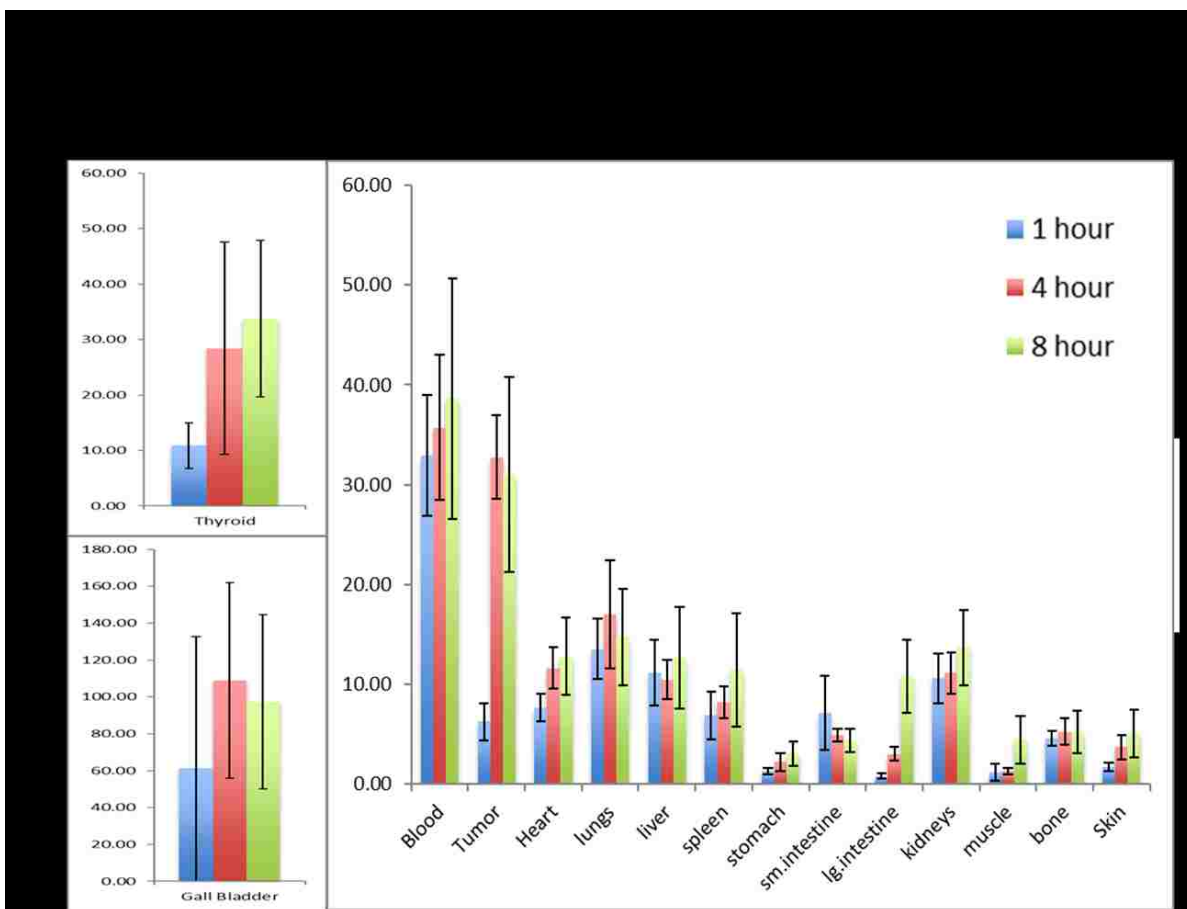


Figure 58. Pre-clicked Biodistribution of $^{99m}\text{TcO-KYCAR- PEG}_5\text{-Tz-A33-TCO}$. The results are reported in %ID/g. Shows retention of activity in the blood due to long circulation time. Also shows significant tumor uptake.

In the pre-clicked biodistribution experiment, the antibody drives the biodistribution and this experiment can inform about the stability of the ^{99m}Tc construct. The first noticeable but expected observation is the retention of the moiety in the blood (32.95 ± 6.08 %ID/g at 1 hour to 38.62 ± 12.03 %ID/g at 8 hours). This is attributed to the long circulation time of the antibody which typically takes up to 24 hours to completely localize. In fact, the presence of increased antibody in the blood is shown as increased uptake throughout all organs. There is a

dramatic decrease in uptake within the gastrointestinal tract. Retention in the small intestine decreases throughout the time points (from 7.11 ± 3.68 %ID/g at 1 hour to 4.34 ± 1.15 %ID/g at 8 hours). There is a slight increase in uptake in the large intestine across the time points (0.80 ± 0.26 %ID/g at 1 hour to 10.82 ± 3.64 %ID/g at 8 hours). These values seem negligible when compared to $^{99m}\text{TcO-KYCAR-PEG}_5\text{-Tz}$ in healthy mice. There is significant tumor uptake present which is most notable. At 1 hour post injection, there is 9.26 ± 6.25 %ID/g and the uptake increases to 32.76 ± 4.21 %ID/g at 4 hours and 31.05 ± 9.78 %ID/g at 8 hours. The increase in the thyroid suggests decomposition of the Tc complex to form pertechnetate. However, the biodistribution results suggest that the $^{99m}\text{TcO-KYCAR-PEG}_5\text{-Tz-A33-TCO}$ construct is reasonably stable *in vivo* for moving forward with pretargeting experiments. SPECT imaging of the $^{99m}\text{TcO-KYCAR-PEG}_5\text{-Tz-A33-TCO}$ in SW1222 xenografted mice were carried out simultaneously with biodistribution studies (Figure 59). As expected 1 hour after injection there is a large amount of activity remaining in the blood pool. This continues for each subsequent time point. The bladder, which is not observed in the biodistribution, obtains the most uptake at hour 1, but is completely undetected for other time points. At 4 hours post injection, the gallbladder is where the majority of uptake is retained. The tumor shows uptake throughout all time points; however it is difficult to distinguish from the blood pool.

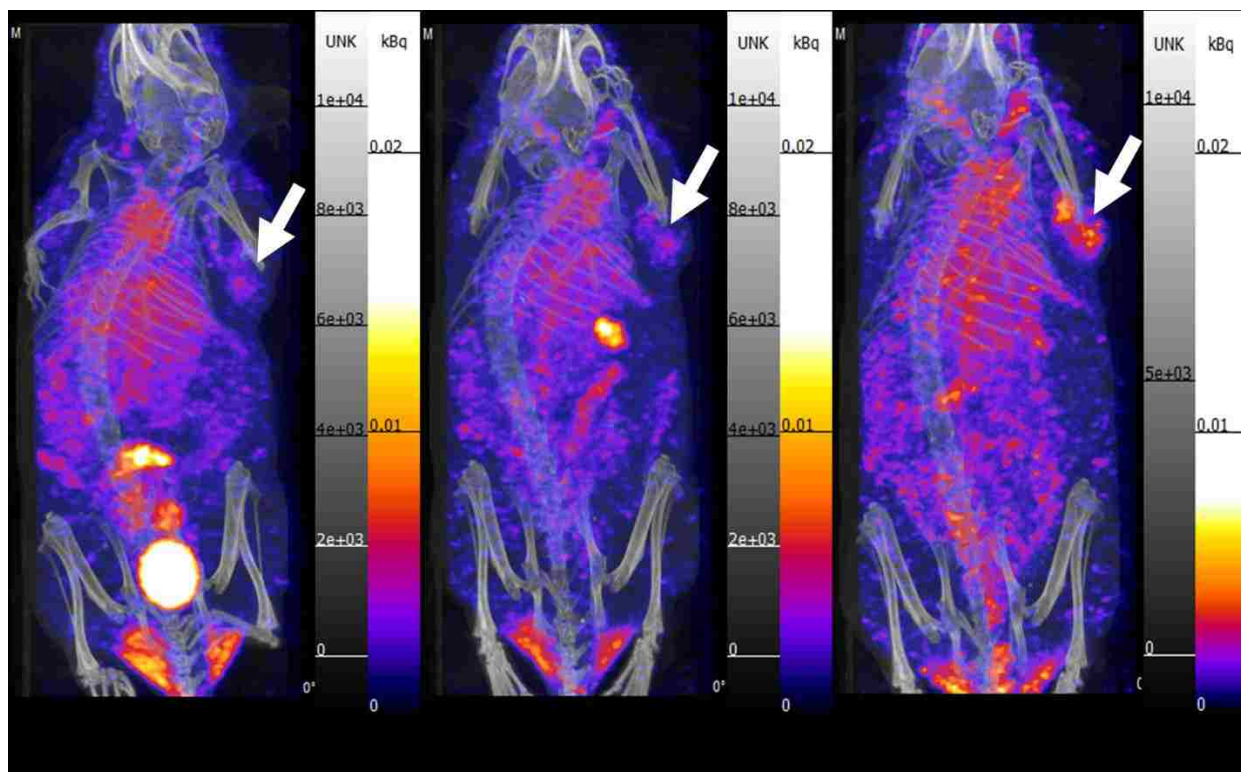


Figure 59. SPECT Images of pre-clicked ^{99m}Tc -KYCAR-PEG5-Tz-A33-TCO. A large amount of activity is found in the blood pool through all time points. However, shows significant tumor uptake by 8 hours. The tumor is marked by the white arrow.

The pre-clicked imaging demonstrated that the ^{99m}Tc construct is reasonably stable *in vivo*. Moving forward pretargeting experiments were evaluated for each system. The biological distribution of ^{99m}Tc -KYCAR-Sh-Tz pretargeted with A33-TCO is tabulated in table 20 and shown in Figure 60.

%ID/g \pm S.D.			
Organ	1 hr	4 hr	8 hr
Blood	2.08 \pm 0.35	2.98 \pm 0.28	1.10 \pm 0.87
Tumor	1.26 \pm 0.20	5.14 \pm 20.6	0.96 \pm 0.62
Heart	1.04 \pm 0.27	1.96 \pm 0.99	0.68 \pm 0.14
Lungs	3.80 \pm 0.83	5.94 \pm 1.64	1.47 \pm 1.53
Liver	4.76 \pm 1.21	7.25 \pm 0.10	1.63 \pm 1.75
Spleen	2.20 \pm 0.63	4.71 \pm 0.52	1.48 \pm 1.19
Stomach	0.72 \pm 0.18	1.12 \pm 0.22	0.40 \pm 0.25
Small Intestine	2.46 \pm 1.13	1.35 \pm 0.55	0.30 \pm 0.14
Large Intestine	0.31 \pm 0.08	30.81 \pm 18.47	12.58 \pm 21.05
Kidneys	5.32 \pm 1.18	7.71 \pm 0.64	2.17 \pm 1.96
Muscle	4.46 \pm 6.02	8.58 \pm 5.30	17.05 \pm 29.45
Bone	1.86 \pm 1.36	3.45 \pm 0.90	2.66 \pm 2.13
Skin	1.07 \pm 0.62	1.90 \pm 0.68	11.92 \pm 24.68
Thyroid	22.42 \pm 6.81	56.18 \pm 25.12	71.85 \pm 102.00
Gall Bladder	396.36 \pm 421.39	436.10 \pm 406.38	2197.05 \pm 4803.32

Table 20. Pretargeted Biodistribution of $^{99m}\text{TcO-KYCAR-Sh-Tz}$. The results are reported in %ID/g. Shows an unusual high accumulation in the muscle. There is some decomposition $^{99m}\text{TcO}_4^-$ accumulating over time in the thyroid, a minimal tumor uptake.

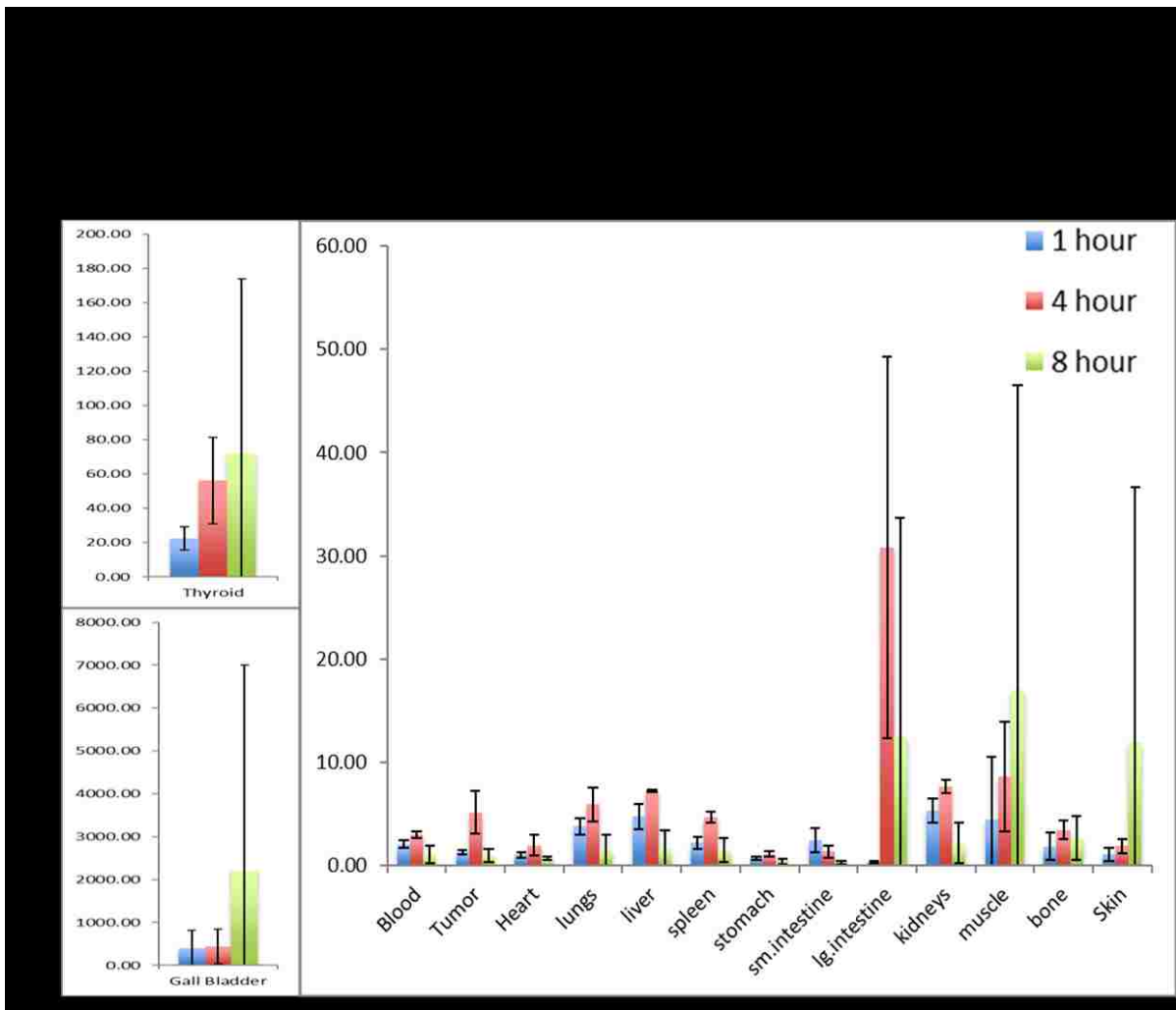


Figure 60. Pretargeted Biodistribution of ^{99m}Tc -KYCAR-Sh-Tz. The results are reported in %ID/g. Shows an unusual high accumulation in the muscle. There is some decomposition $^{99m}\text{TcO}_4^-$ accumulating over time in the thyroid, a minimal tumor uptake.

The biological distribution shows minimal uptake in most organs. There is an unusually high uptake found in the muscle that shows an upward trend with each time point. At 1 hour post injection, the muscle showed 4.46 ± 6.02 %ID/g, at 4 hours it showed 8.58 ± 5.30 %ID/g, and at 8 hours 17.05 ± 29.45 %ID/g. This result is surprising since there was little uptake in the muscle

shown in biological distribution in healthy mice. The complex is not retained in small intestines; however, some uptake is seen at 4 and 8 hour post injection in the large intestine (30.81 ± 18.47 %ID/g and 12.58 ± 21.05 %ID/g respectively). The thyroid shows a significant upward trend through each time point (22.42 ± 6.81 %ID/g at 1 hour and 71.85 ± 102.00 %ID/g at 8 hours) This could be indicative of decomposition to $^{99m}\text{TcO}_4^-$. The tumor uptake is minimal; at 1 hour uptake is 1.26 ± 0.20 %ID/g, 4 hour it is 5.14 ± 20.6 %ID/g, and 8 hour is 0.96 ± 0.62 %ID/g.

Simultaneous SPECT images were also collected, and immediately the uptake in the blood is considerably lower than in the pre-clicked experiments, lowering the background (Figure 61). At 1 hour post injection, the small intestines and bladder exhibit the major uptake in the images. Also, the gallbladder shows accumulation which is seen in the biodistribution at early time points. Throughout the remaining timepoints the uptake moves through the large intestine and remains in the gallbladder. Tumor uptake at 1 and 4 hours post injection is observed and is distinctive, however by hour 8 the activity found in the tumor has decreased.

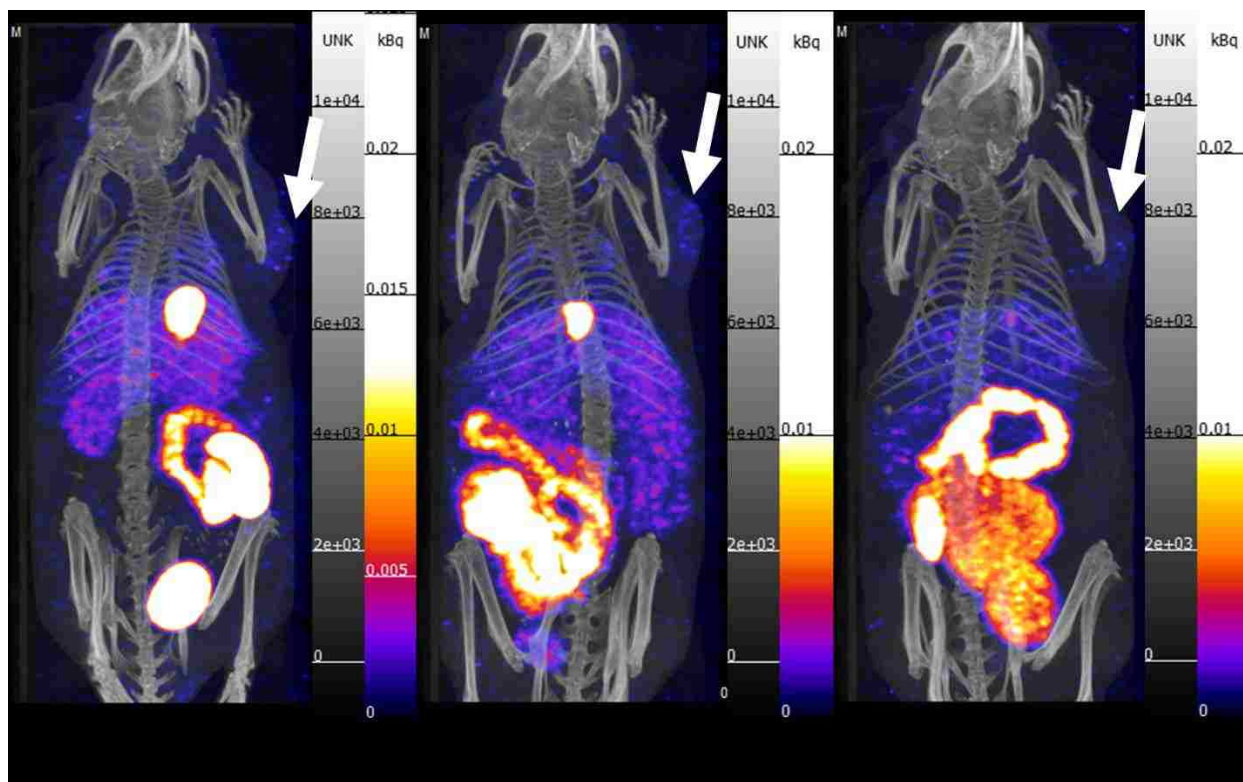


Figure 61. Pretargeted SPECT Images of $^{99m}\text{TcO-KYCAR-Sh-Tz}$. Shows high accumulation in the gallbladder in early time points. There is a large amount of gut uptake. Tumor uptake at 1 and 4 hours post injection is observed and distinctive. The tumor is marked by the white arrow.

The biological distribution of $^{188}\text{ReO-KYCAR-Sh-Tz}$ pretargeted with A33-TCO is tabulated in table 21 and shown in Figure 62.

%ID/g \pm S.D.			
Organ	1 hr	4 hr	8 hr
Blood	3.49 \pm 0.38	2.44 \pm 0.28	1.52 \pm 0.25
Tumor	1.46 \pm 0.13	1.49 \pm 0.39	1.85 \pm 0.31
Heart	1.00 \pm 0.12	0.73 \pm 0.15	0.49 \pm 0.09
Lungs	1.98 \pm 0.18	1.35 \pm 0.16	0.80 \pm 0.14
Liver	2.37 \pm 0.33	1.26 \pm 0.18	0.83 \pm 0.22
Spleen	0.93 \pm 0.11	0.67 \pm 0.12	0.45 \pm 0.10
Stomach	12.15 \pm 2.32	9.60 \pm 6.05	4.35 \pm 5.94
Small Intestine	22.31 \pm 24.45	1.60 \pm 0.72	0.39 \pm 0.21
Large Intestine	1.10 \pm 1.03	43.13 \pm 7.99	18.57 \pm 10.88
Kidneys	2.82 \pm 0.25	1.93 \pm 0.23	1.55 \pm 0.16
Muscle	0.47 \pm 0.14	0.36 \pm 0.18	0.47 \pm 0.48
Bone	0.68 \pm 0.10	0.53 \pm 0.15	0.28 \pm 0.15
Skin	1.03 \pm 0.10	0.60 \pm 0.12	0.43 \pm 0.09
Thyroid	154.10 \pm 29.54	159.44 \pm 47.78	68.14 \pm 47.77
Gall Bladder	1182.56 \pm 617.08	96.70 \pm 19.56	4.24 \pm 2.37

Table 21. Pretargeted Biodistribution of $^{188}\text{ReO-KYCAR-Sh-Tz}$. The results are reported in %ID/g. Shows an unusual high accumulation in the muscle. There is some decomposition $^{188}\text{ReO}_4^-$ accumulating in the thyroid and stomach, Minimal tumor uptake.

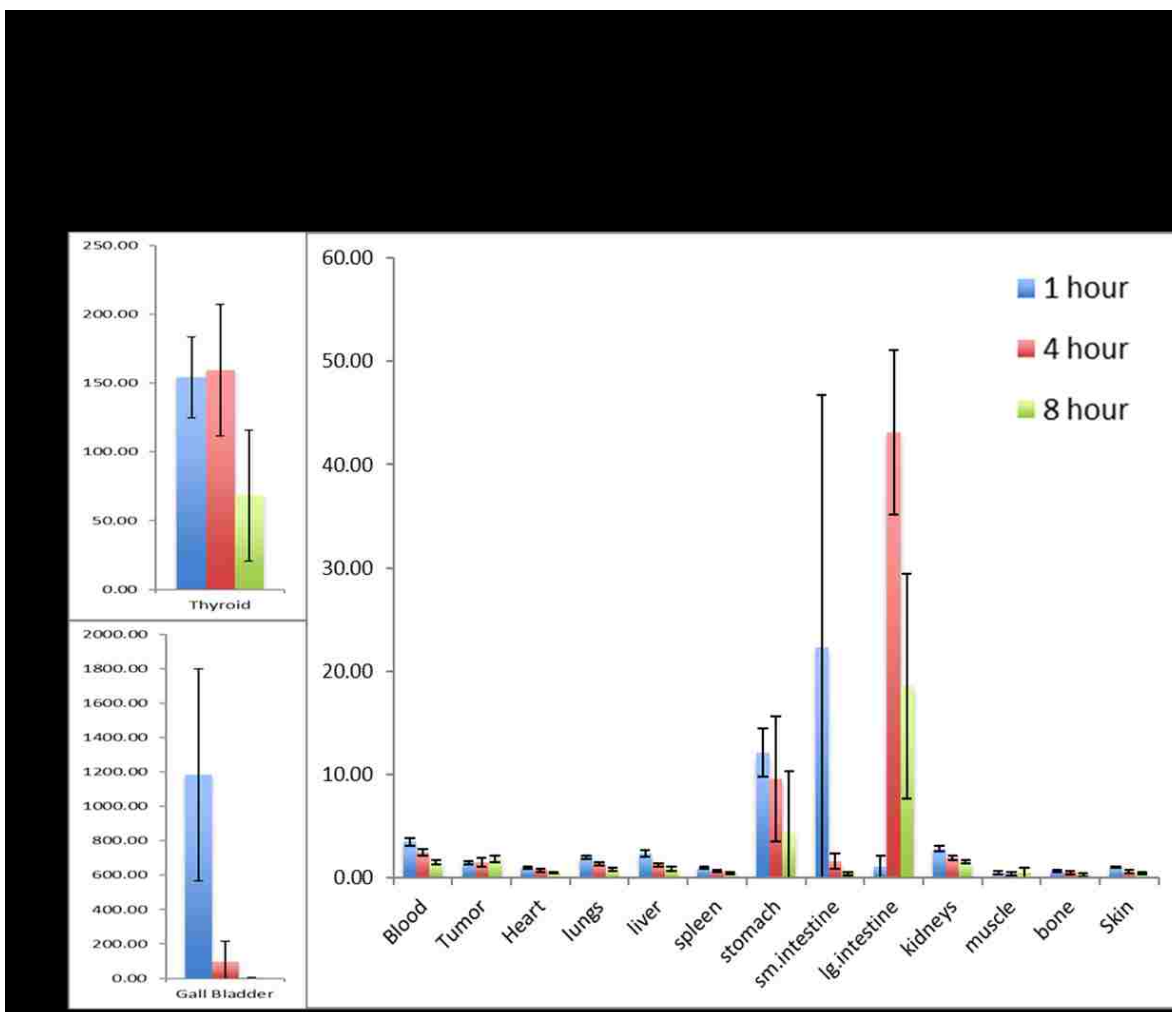


Figure 62. Pretargeted Biodistribution of $^{188}\text{ReO-KYCAR-Sh-Tz}$. The results are reported in %ID/g. Shows an unusual high accumulation in the muscle. There is some decomposition $^{188}\text{ReO}_4^-$ accumulating in the thyroid and stomach, Minimal tumor uptake.

Stomach uptake is apparent, although a reduction in uptake is seen at each time point (12.15 ± 2.32 %ID/g at 1 hour and 4.35 ± 5.94 %ID/g at 8 hour). There is also uptake and depletion found in the thyroid (154.10 ± 29.54 %ID/g at 1 hour and 68.14 ± 47.77 %ID/g). Accumulation in both organs suggests decomposition to $^{188}\text{ReO}_4^-$. Movement through the gastrointestinal track is

observed, and is likely due to circulation of unclicked complex. Small intestines show uptake at 1 hour (22.31 ± 24.45 %ID/g) and the large intestines show uptake at 4 and 8 hours (43.13 ± 7.99 %ID/g and 18.57 ± 10.88 %ID/g, respectively). There is minimal uptake found in the tumor (1.46 ± 0.13 %ID/g at 1 hour and 1.85 ± 0.31 %ID/g at 8 hours).

SPECT images of the $^{188}\text{ReO-KYCAR-Sh-Tz}$ complex were also obtained (Figure 63). At 1 hour post injection the gallbladder, small intestines and bladder all show uptake. Gut uptake remains throughout all timepoints. Tumor uptake is not observed, low tumor uptake and low gamma emission could be the cause.

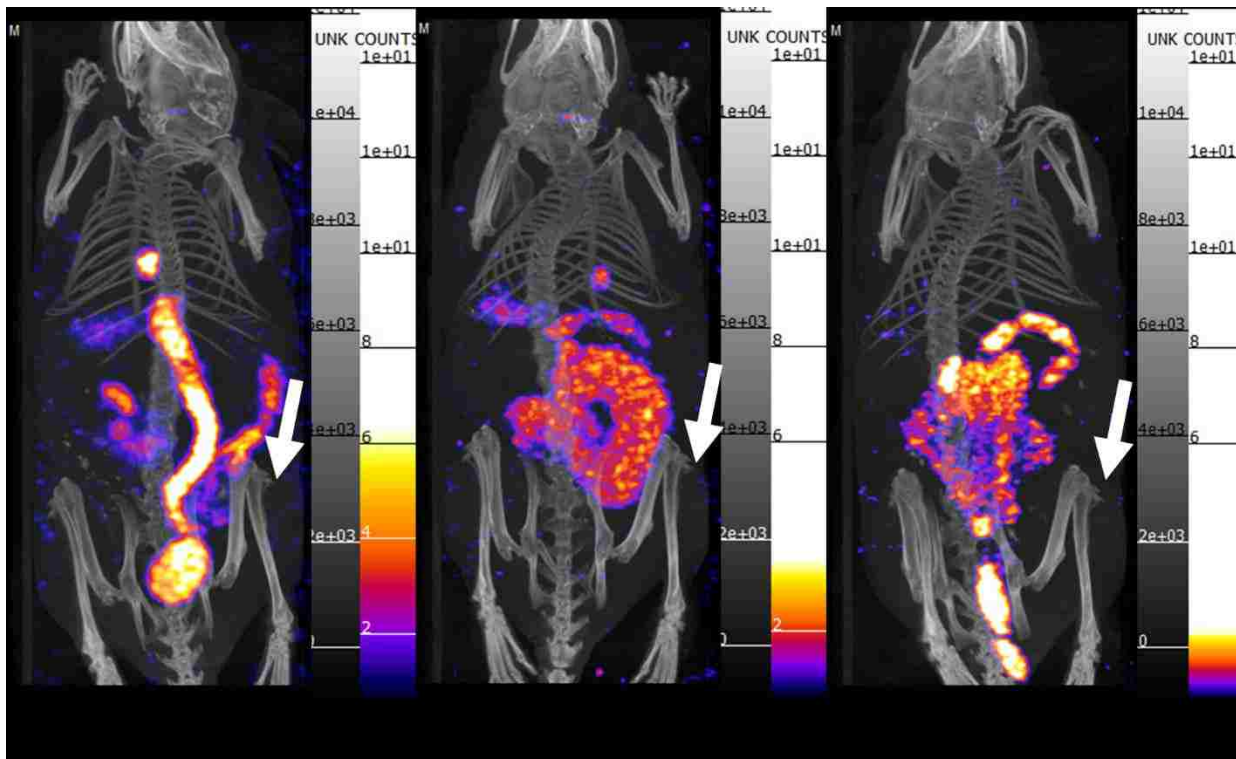


Figure 63. Pretargeted SPECT Images of $^{188}\text{ReO-KYCAR-Sh-Tz}$. Shows high accumulation in the gallbladder, small intestines and bladder. Tumor uptake is not observed. Tumor is marked by the white arrow.

The biological distribution of $^{99\text{m}}\text{TcO-KYCAR-PEG}_5\text{-Tz}$ pretargeted with A33-TCO is tabulated in table 22 and shown in Figure 64.

%ID/g \pm S.D.			
Organ	1 hr	4 hr	8 hr
Blood	19.81 \pm 4.45	14.16 \pm 3.06	14.64 \pm 2.02
Tumor	10.31 \pm 2.24	13.42 \pm 4.05	20.04 \pm 3.26
Heart	6.66 \pm 1.70	4.61 \pm 1.32	5.15 \pm 0.94
Lungs	14.20 \pm 6.33	8.95 \pm 3.73	7.47 \pm 1.33
Liver	10.89 \pm 2.83	7.11 \pm 1.11	5.41 \pm 0.62
Spleen	6.45 \pm 2.23	4.93 \pm 1.30	4.75 \pm 1.27
Stomach	3.57 \pm 0.83	4.83 \pm 1.12	13.19 \pm 24.56
Small Intestine	125.56 \pm 159.93	6.54 \pm 1.63	2.09 \pm 0.24
Large Intestine	1.95 \pm 0.78	201.59 \pm 94.52	191.59 \pm 187.42
Kidneys	14.03 \pm 2.14	13.04 \pm 1.85	15.38 \pm 1.97
Muscle	5.07 \pm 3.75	14.09 \pm 10.47	11.76 \pm 5.06
Bone	3.08 \pm 0.98	4.68 \pm 1.04	5.72 \pm 1.38
Skin	3.10 \pm 0.38	3.32 \pm 1.04	4.20 \pm 1.38
Thyroid	103.01 \pm 73.14	49.99 \pm 15.80	55.21 \pm 8.56
Gall Bladder	17425.57 \pm 20434.43	5419.03 \pm 5162.55	74.99 \pm 34.45

Table 22. Pretargeted Biodistribution of $^{99m}\text{TcO-KYCAR-PEG}_5\text{-Tz}$. The results are reported in %ID/g. Shows possible unclicked $^{99m}\text{TcO-KYCAR-PEG}_5\text{-Tz}$ in the gastrointestinal track. Shows slow accumulation at the tumor site.

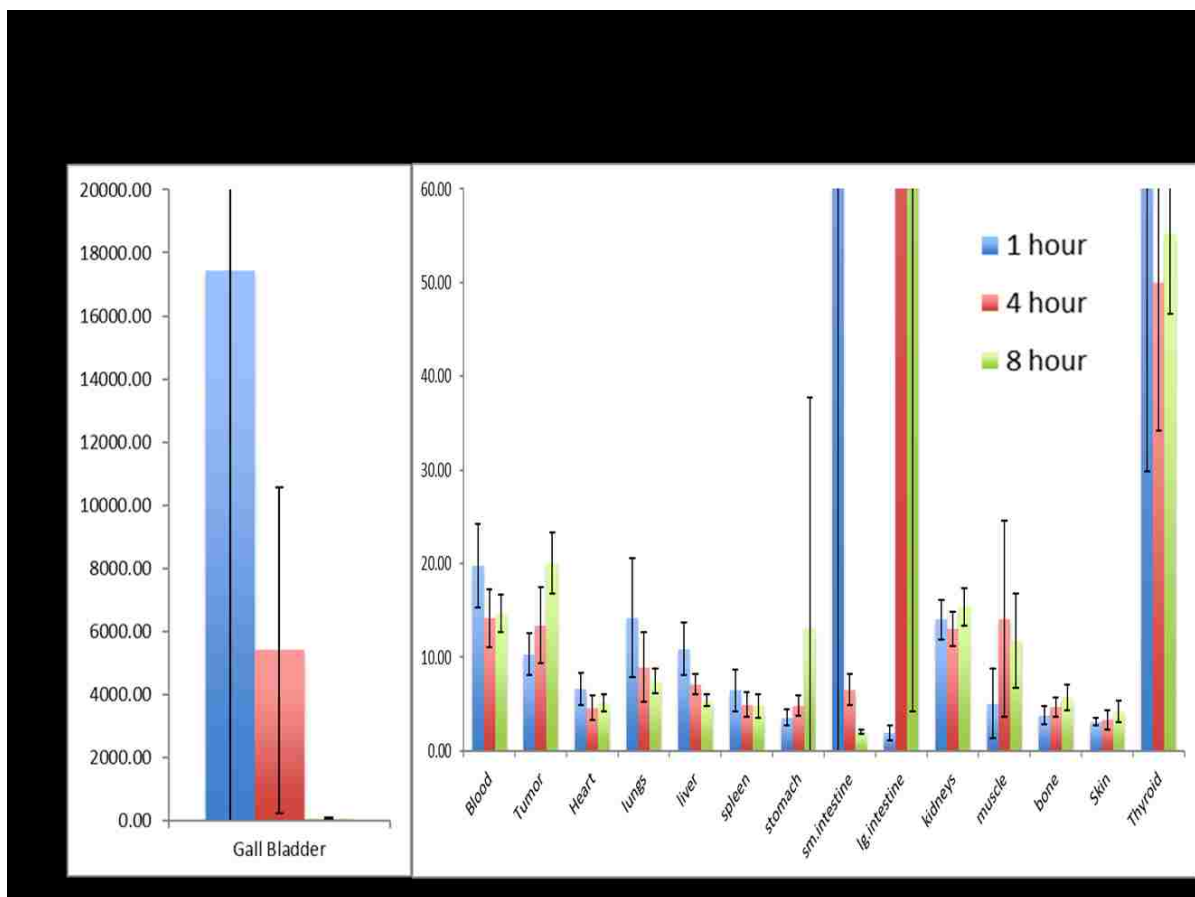


Figure 64. Pretargeted Biodistribution of $^{99m}\text{TcO-KYCAR-PEG}_5\text{-Tz}$. The results are reported in %ID/g. Possible unclicked $^{99m}\text{TcO-KYCAR-PEG}_5\text{-Tz}$ is found in the gastrointestinal track. These data show slow accumulation at the tumor site.

Uptake is found at higher elevation for all organs in comparison to the previous systems. There is a rapid accumulation and depletion observed in the blood (19.81 ± 4.45 %ID/g at 1 hour and 14.64 ± 2.02 %ID/g at 8 hours). This quick accumulation and depletion is also found in the lungs (14.20 ± 6.33 %ID/g at 1 hour and 7.47 ± 1.33 %ID/g at 8 hours) and liver (10.89 ± 2.83 %ID/g at 1 hour and 5.41 ± 0.62 %ID/g at 8 hours). Unclicked $^{99m}\text{TcO-KYCAR-PEG}_5\text{-Tz}$ complex is likely

observed in the gastrointestinal track. The small intestines show uptake at 1 hour (125.56 ± 159.93 %ID/g), and the accumulation travel to the large intestines (201.59 ± 94.52 %ID/g at 4 hours and 191.59 ± 187.42 %ID/g). Most notably there is a slow accumulation at the tumor site. At 1 hour post injection (10.31 ± 2.24 %ID/g), 4 hour (13.42 ± 4.05 %ID/g) and 8 hour (20.04 ± 3.26 %ID/g).

Simultaneously SPECT images were collected (Figure 65). As previous studies show most accumulation is seen in the gallbladder, small intestines and bladder at 1 hour. Gut uptake remains most prevalent throughout the timepoints. Uptake at the tumor site is rapid and is retained throughout the time points. Moreover, tumor accumulation is discernible throughout.

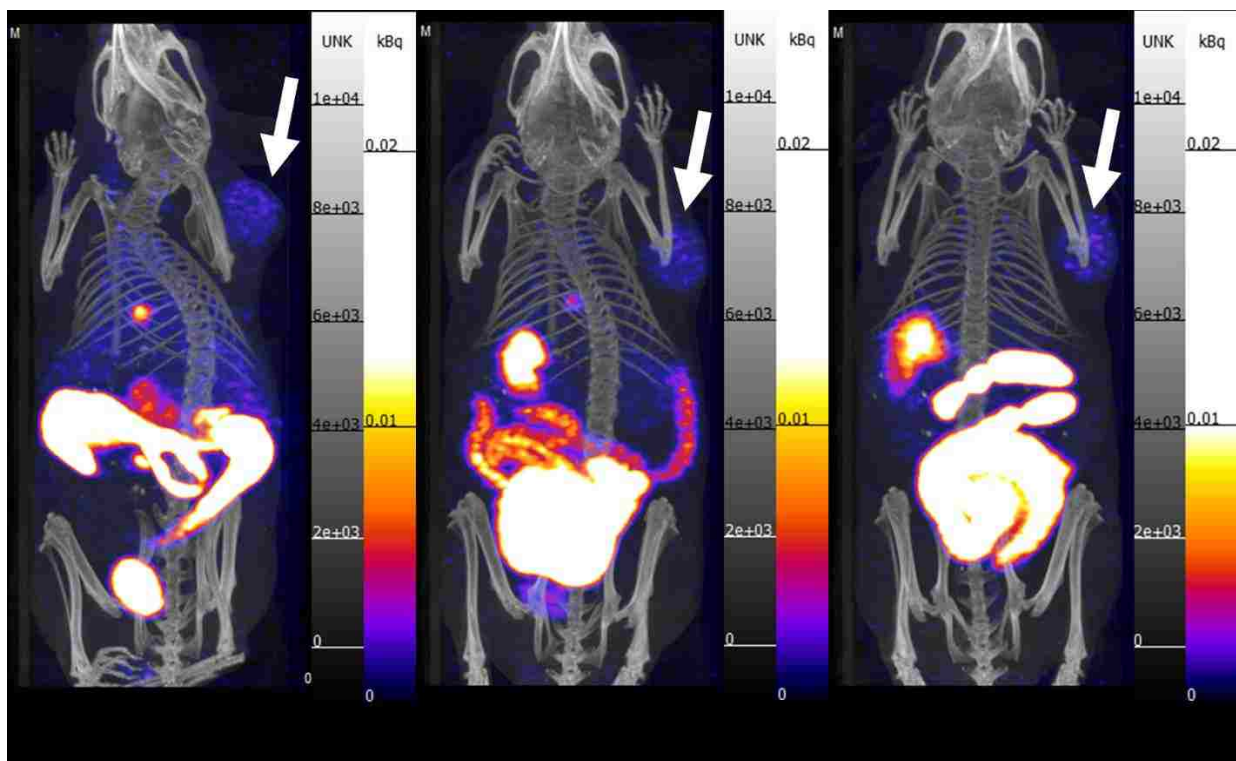


Figure 65. Pretargeted SPECT Images $^{99m}\text{TcO-KYCAR-PEG}_5\text{-Tz}$. Shows high accumulation in the gallbladder, small intestines and bladder. Tumor uptake is observed and discernable throughout the experiment. The tumor is marked by the white arrow.

The biological distribution of $^{188}\text{ReO-KYCAR-PEG}_5\text{-Tz}$ pretargeted with A33-TCO is tabulated in table 23 and shown in Figure 66.

%ID/g \pm S.D.			
Organ	1 hr	4 hr	8 hr
Blood	2.33 \pm 0.30	2.43 \pm 1.03	1.74 \pm 0.23
Tumor	1.06 \pm 0.06	1.50 \pm 0.51	1.64 \pm 0.21
Heart	0.76 \pm 0.10	0.67 \pm 0.26	0.56 \pm 0.13
Lungs	1.73 \pm 0.34	1.41 \pm 0.62	1.03 \pm 0.20
Liver	1.44 \pm 0.29	1.29 \pm 0.72	0.89 \pm 0.25
Spleen	0.68 \pm 0.10	0.77 \pm 0.44	0.53 \pm 0.15
Stomach	8.09 \pm 5.00	10.40 \pm 6.51	5.14 \pm 2.62
Small Intestine	30.63 \pm 24.74	14.56 \pm 29.74	0.50 \pm 0.25
Large Intestine	0.32 \pm 0.21	23.50 \pm 36.68	28.23 \pm 14.23
Kidneys	1.68 \pm 0.26	1.49 \pm 0.52	1.17 \pm 0.13
Muscle	0.58 \pm 0.28	0.73 \pm 0.64	0.62 \pm 0.18
Bone	0.53 \pm 0.06	0.49 \pm 0.29	0.30 \pm 0.08
Skin	0.64 \pm 0.16	0.56 \pm 0.17	0.42 \pm 0.07
Thyroid	124.55 \pm 50.26	136.91 \pm 86.29	67.45 \pm 30.06
Gall Bladder	959.16 \pm 833.50	369.43 \pm 468.55	71.43 \pm 61.42

Table 23. Pretargeted Biodistribution of $^{188}\text{ReO-KYCAR-PEG}_5\text{-Tz}$. The results are reported in %ID/g. Shows high accumulation in the gastrointestinal track. There is decomposition $^{188}\text{ReO}_4^-$ accumulating in the thyroid and stomach, Minimal tumor uptake.

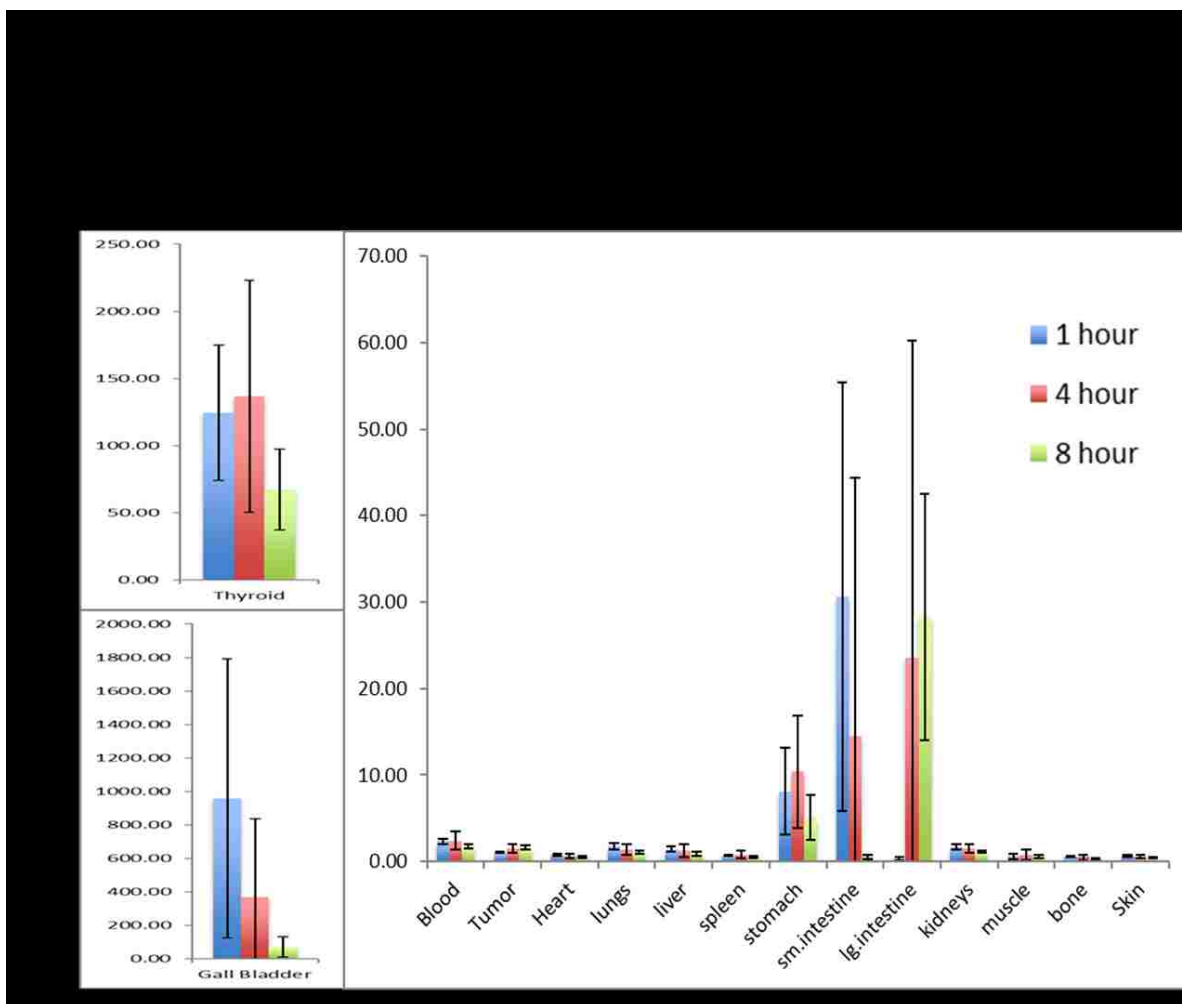


Figure 66. Pretargeted Biodistribution of $^{188}\text{ReO-KYCAR-PEG}_5\text{-Tz}$. The results are reported in %ID/g. Shows high accumulation in the gastrointestinal track. There is decomposition $^{188}\text{ReO}_4^-$ accumulating in the thyroid and stomach, Minimal tumor uptake.

The biological distribution shows a slight accumulation and depletion in the blood (2.33 ± 0.30 %ID/g at 1 hour and 1.74 ± 0.23 %ID/g at 8 hours). Uptake in the stomach (8.09 ± 5.00 %ID/g at 1 hour , 10.40 ± 6.51 %ID/g at 4 hours and 5.14 ± 2.62 %ID/g at 8 hours) shows decomposition. Uptake and depletion in the thyroid (124.55 ± 50.26 %ID/g at 1 hour, 136.91 ± 86.29 %ID/g at 4 hours, and 67.45 ± 30.06 %ID/g at 8 hours) also indicated decomposition. Intact unclicked $^{188}\text{ReO-KYCAR-PEG}_5\text{-Tz}$ complex travels through the gastrointestinal track. The small intestines

show uptake and depletion (30.63 ± 24.74 %ID/g at 1 hour, 14.56 ± 29.74 %ID/g at 4 hours and 0.50 ± 0.25 %ID/g). Slow accumulation is observed in the large intestines (0.32 ± 0.21 %ID/g at 1 hour, 23.50 ± 36.68 %ID/g at 4 hours, and 28.23 ± 14.23 %ID/g at 8 hours). Tumor accumulation is minimal and steady (1.06 ± 0.06 %ID/g at 1 hour, 1.50 ± 0.51 %ID/g at 4 hours, and 1.64 ± 0.21 %ID/g at 8 hours).

3.12. Conclusion

^{99m}Tc , ^{188}Re and Re peptides were successfully conjugated to two different tetrazine moieties. The conjugations were purified via HPLC and cold complexes were first confirmed by mass spectroscopy. IR data further concludes conjugation by the changes in the intensities of stretches. Because these constructs are novel the characterization of them creates a baseline for further optimization.

The ^{99m}Tc , ^{188}Re Sh-tetrazine complexes in healthy mice both are excreted through the gastrointestinal track. In both systems, high initial uptake is observed in the small intestine which shifts to the large intestines 2 hour post injection. This is somewhat expected due to the lipophilicity of the complexes. There is little decomposition shown in the technetium complexes, while the rhenium complex shows considerable thyroid accumulation.

The ^{99m}Tc , ^{188}Re PEG₅-tetrazine complexes in healthy mice are unaffected by increase of hydrophilic components and the route of excretion remains through the gastrointestinal track. The technetium complexes show decomposition, observed as accumulation in the thyroid than the $^{99m}\text{TcO-KYCAR-Sh-Tz}$ complex. Similarly, the rhenium PEG₅-tetrazine complex also decomposes *in vivo*, and shows uptake in the stomach and thyroid.

The pre-clicked moiety, $^{99m}\text{TcO-KYCAR-PEG}_5\text{-Tz-A33-TCO}$, showed less accumulation through the gastrointestinal track, though high uptake in the blood pool. Favorable tumor uptake is achieved; however, tumor uptake competes with uptake in the blood pool.

Pretargeting experiments overall show less than desirable tumor accumulations. In the Sh-Tz systems the technetium complexes showed an unusual accumulation in the muscle. These complexes also exhibited slight decomposition and excretion through the gut, however SPECT images show discernible tumor uptake. The rhenium Sh-Tz complexes behave similarly to the technetium complex. The biodistribution data shows slight tumor uptake, though it is not visible through SPECT imaging.

The $\text{PEG}_5\text{-Tz}$ complexes both show decomposition and gut excretion despite their hydrophilic nature. The $^{99m}\text{TcO-KYCAR-PEG}_5\text{-Tz}$ complex exhibited the best tumor accumulation of the 4 complexes. Despite the considerable gut uptake other non-target organs are relatively low thus showing distinct tumor uptake in SPECT images.

Comparing the pre-clicked experiment to the pretargeting experiments it is hypothesized that the decrease tumor uptake is due to the rapid clearance of the complex from the blood. The small size of the radioligand possibly only allows one pass through the tumor site for the click reaction to occur. Another possibility is that the A33-TCO is in circulation in the blood thus preventing click reaction to occur at the tumor site. It is important to note that in each system, in healthy and SW1222 xenografted mice there is appreciable uptake in the gall bladder. It is hypothesized that accumulation to the gallbladder is influenced by the C-terminus of the pentapeptide.

4. Summary

Complexes with ^{99m}Tc and ^{188}Re and a pentapeptide (KYCAR) have been synthesized, and characterized by the macroscopic non-radioactive Re. The non-radioactive rhenium-peptide shows that there are two isomeric species that elute within minutes of each other. IR data further concludes that the two isolated species are diastereomers due to the similar stretches and frequencies. Proton NMR data first confirms the chelation between Re and KYCAR by showing the deprotonation of the amide nitrogens on the tyrosine and cysteine residues. The data also confirms this through the observation of the shifts in the β -protons on both the lysine side chain and the cysteine side chain. The proton NMR also assists in the assignment of the diastereomers. Purified peak 2 (syn) has chemical shifts downfield from the free ligand as well as the first peak which correlates to the deshielding effect imposed by the position of the Re-oxo core. Circular dichroism gives solid information on the diastereomers. This data shows that peak 1 (anti) follows the trend of having a large positive Cotton effect about the region that correlates to the oxygen rhenium charge transfer transition. It also shows that peak 2 (syn) follows the trend of having a negative Cotton effect about the same region. Through the crystallization of ReO-KYC information about the structure about the chelating region was obtained. It was determined that the crystal in its syn confirmation correlates to peak in HPLC analyses. This concludes that ReO-KYCAR peak 2 is also in the syn confirmation.

The fully characterized ReO-KYCAR was successfully coeluted with the tracer level $^{99m}\text{TcO-KYCAR}$ and $^{188}\text{ReO-KYCAR}$ to confirm that the complexes were chemically similar. *In vitro* both complexes are relatively stable in biological conditions up to 2 hours. *In vivo* $^{99m}\text{TcO-KYCAR}$

shows high uptake in the liver small intestines, and large intestines up to 4 hours post injection. The technetium compound is excreted via the hepatobiliary system, remains relatively stable. The $^{188}\text{ReO-KYCAR}$ show very similar organ uptake to its technetium congener. The rhenium complex is less stable, decomposing to perrhenate, accumulating in the stomach and thyroid.

Novel conjugations between non-radioactive ReO-KYCAR and tetrazine (sh-Tz and $\text{PEG}_5\text{-Tz}$) moieties were successful. These conjugations were purified, characterized, and confirmed by reverse phase HPLC, mass spectral analysis, and IR. The characterized complexes were then used to confirm the syntheses of the $^{99\text{m}}\text{Tc}$ and ^{188}Re complexes.

Biologically in healthy mice the $^{99\text{m}}\text{Tc}$ and ^{188}Re Sh-tetrazine complexes are excreted through the gastrointestinal track. There is little decomposition shown in the technetium complex, while the rhenium complex shows thyroid accumulation. The $^{99\text{m}}\text{Tc}$ and ^{188}Re $\text{PEG}_5\text{-tetrazine}$ complexes are also excreted through the gastrointestinal track despite the increase of hydrophilic components. Both complexes show decomposition; Tc shows accumulation in the thyroid and Re shows accumulation in the stomach and thyroid.

The pre-clicked moiety $^{99\text{m}}\text{TcO-KYCAR-PEG}_5\text{-Tz-A33-TCO}$ shows favorable tumor uptake, though tumor uptake competes with uptake in the blood pool. Pretargeting experiments with $^{99\text{m}}\text{TcO-KYCAR-Sh-Tz}$ show slight decomposition and excretion through the gut, however SPECT images show discernable tumor uptake. The complex $^{188}\text{ReO-KYCAR-Sh-Tz}$ behaves similarly to the technetium complex. biodistribution data show tumor uptake, despite being invisible through SPECT imaging. The $^{188}\text{ReO-KYCAR-PEG}_5\text{-Tz}$ complex shows minimal tumor uptake, and has increased decomposition to $^{188}\text{ReO}_4^-$. The $^{99\text{m}}\text{TcO-KYCAR-PEG}_5\text{-Tz}$ complex exhibited the

best tumor accumulation of the 4 pretargeting complexes. Despite the considerable gut uptake dose to other non-target organs is low thus showing distinct tumor uptake in SPECT images.

These constructs show promise for *in vivo* applications. The characterization of the nonradioactive rhenium complexes creates a baseline library for the investigation of similar constructs. These constructs could be optimized further to enhance the biological results. Some future experiments for the optimization of these complexes are summarized in the next chapter.

5. Future Work

Investigations of the effects of altering the order or exchanging the amino acids within the peptide could produce a more favorable chelator and result in better *in vivo* distribution. Exchanging the C-terminus on the arginine for an amine could prevent uptake in the gallbladder. Crystallization of the anti ReO-KYC should be completed to fully understand the diastereomers of the ReO-KYCAR complexes.

To optimize the radiolabeling process the peptide could be conjugated to the tetrazine prior to radiolabeling. This could reduce the decomposition that occurs by radiolabeling the entire chelator in one step.

Conjugation to other tetrazines should be tested, which could increase *in vivo* click at the tumor site. Bulkier tetrazines will increase the molecular weight and could assist in slowing the blood clearance, thus facilitating occurrence of click reactions at the tumor site.

In pretargeting experiments the use of a clearing agent should be investigated to observe whether dose to non-target organs is decreased. Injecting with a clearing agent after the injection of the antibody will assist in removing residual antibody circulating through the body. This extra step can increase tumor uptake and decrease dose to non-tumor organs.

To enhance the stability of ^{188}Re -peptide conjugation a radioprotectant that is inert to the components of the chelator should be used. The emitted β particle causes damage to the

catalysts and other compounds in the reaction mixture. The radioprotectant can absorb the β particle reducing the radiolytic damage.

References

1. American Cancer Society. Cancer facts and figures. American Cancer Society 2016.
2. Jurisson S, Berning D, Jia W, Ma D. Coordination compounds in nuclear medicine. *Chem Rev* 1993;93(3):1137-56.
3. Carlson S. A glance at the history of nuclear medicine. *Acta Oncologica* 1995;34(8):1095-1102.
4. Prinzmetal M, Corday E, Bergman H, Schwartz L, Spritzler R. Radiocardiography. A new method for studying the blood flow through the chambers of the heart in human beings. *Science* 1948;108:340-2.
5. Nylin G, Celander H. Determination of blood volume in the heart and lungs and the cardiac output Through the injection of radiophosphorus. *Circulation* 1950;1:76-83.
6. Hamilton J, Soley M. Studies in iodine metabolism by use of a new radioactive isotope of iodine. *American Journal of Physiology* 1939;127:557-72.
7. Hertz S, Roberts A, Evans R. Radioactive iodine as an indicator in the study of thyroid physiology. *Proceedings of the Society of Experimental Biology and Medicine* 1938;38:510.
8. Strauss H, Harrison K, Langan J, Lebowitz E, Pitt B. Thallium-201 for myocardial imaging. relation of thallium-201 to regional myocardial perfusion. *Circulation* 1975;51:641-5.
9. Langner J. Event driven motion compensation in positron emission tomography: Development of a clinically applicable method. 2008.
10. Muehllehner G, Karp J. Positron emission tomography. *Physics in Medicine and Biology* 2006;51:117-37.
11. Ollinger J, Fessler J. Positron-emission tomography. *IEEE Signal Processing Magazine* 1997:43-55.
12. Lundqvist H, Lubberink M, Tolmachev V. Positron emission tomography. *European Journal of Physics* 1998;19:537-52.
13. [Internet] [cited 2017 02/22]. Available from: By Kieranmaher - Own work, Public Domain, <https://commons.wikimedia.org/w/index.php?curid=12719562>.

14. Anger H. Scintillation camera. Review of Scientific Instruments 1958;29:27-33.
15. Anger H. Scintillation camera with multichannel collimators. Journal of Nuclear Medicine 1964;5:515-31.
16. Knoll G. Single-photon emission computed tomography. Proceedings of the Institute of Electrical and Electronics Engineers 1983;71(3):320-9.
17. Holly T, Abbott B, Al-Mallah M, Calnon D, Cohen M, DiFilippo F, Ficaro E, Freeman M, Hendel R, Jain D, et al. Single photon-emission computed tomography. Journal O Nuclear Cardiology 2010;17(5):941-73.
18. Perrier C, Segre E. Radioactive isotopes of element 43. Nature 1937;140:193-4.
19. Baum E, Ernesti M, Knox H, Miller T, Watson A. Nuclides and isotopes chart of the nuclides. 17th ed. Bechtel Marine Propulsion Corporation; 2009. .
20. Schwochau K. Technetium. chemistry and radiopharmacuetical applications. Germany: Wiley-vch; 2000. .
21. International Atomic Energy Agency. Technetium-99m radiopharmaceuticals: Manufacture of kits- vienna. Vienna: ; 2008. Report nr 466.
22. Okarvi s. Peptide-based radiopharmaceuticals: Future tools for diagnostic imaging of cancers and other diseases. Medicinal Research Reviews 2004;24:357-97.
23. Vanbilloen H, Bormans G, De Roo M, Verbruggen A. Complexes of technetium-99m with tertapeptides, A new class of 99mTc-labelled agents. Nuclear Medicine and Biology 1995;2:325-38.
24. Wadas T, Wong E, Weisman G, Anderson C. Coordinating radiometals of copper, gallium, indium, yttrium, and zirconium for PET and SPECT imaging of disease. Chemical Reviews 2010;110:2858-902.
25. Tucker W, Greene M, Weiss A, Murrenhoff A. Methods of preparation of some carrier-free radio-isotopes involving sorption on alumina. report BNL-3746. Transactions of the American Nuclear Society 1958;1:160.
26. Cantorias MV. Structural elucidation and dynamic studies of $[M^V=O]$ tripeptide diastereomers ($M=^{99m}Tc, ^{99}Tc, re$): An extension to targeted radiopharmaceuticals. ; 2006.
27. Francesconi LC, Cantorias MV, Howell RC. Metal-based imaging agents. In: Encyclopedia of inorganic chemistry. John Wiley & Sons, Ltd; 2006. .

28. Francesconi LC, Zheng Y, Bartis J, Blumenstein M, Costello C, De Rosch MA. Preparation and characterization of ^{99}TcO] apcitide: A technetium labeled peptide. *Inorg Chem* 2004 05/01;43(9):2867-75.
29. Lister-James J, Knight LC, Maurer AH, Bush LR, Moyer BR, Dean RT. Thrombus imaging with a technetium-99m-labeled activated platelet receptor-binding peptide. *J Nucl Med* 1996 May;37(5):775-81.
30. Lister-James J, Dean R. Technetium-99m-labeled receptor specific small synthetic peptides: Practical imaging agents of biomedical markers. In: M. Nicolini, U. Mazzi, editors. *Technetium, rhenium and other metals in Chemistry and nuclear medicine*. 5th ed. Padova: Servizi Grafici Editoriali; 1999. .
31. Cyr JE, Pearson DA, Nelson CA, Lyons B, A., Zheng Y, Bartis J, He J, Cantorias MV, Howell RC, Francesconi LC. Isolation, characterization, and biological evaluation of syn and anti diastereomers of $^{99\text{mTc}}$ technetium depreotide: A somatostatin receptor binding tumor imaging agent. *Journal of Medicinal Chemistry* 2007;50:4295-4303.
32. Abram UAA, Roger. Technetium and rhenium: Coordination chemistry and nuclear medical applications. *Journal of the Brazilian Chemical Society* 2006 12;17:1486.
33. G. Bormans, B. Cleynhens, P. Adriaens, H. Vanbilloen, M. De Roo, A. Verbruggen,. Investigation of the labelling characteristics of $^{99\text{mTc}}$ -mercaptoacetyltryglycine. *Nucl Med Biol* 1995;22(3):339.
34. - R. Dilworth J, - J. Parrott S. - The biomedical chemistry of technetium and rhenium. - *Chem Soc Rev*(- 1):- 43.
35. Quirijnen J, HAn S, Zonnenberg B, de Klerk J, van het Schip A, van Dijk A, ten Kroode H, Blijham G, van Rijk P. Efficacy of rhenium-186-etidronate in prostate cancer patients with metastatic bone pain. *Journal of Nuclear Medicine* 1996;37(9):1511-5.
36. Silberstein EB. The treatment of painful osteoblastic metastases: What can we expect from nuclear oncology? *J Nucl Med* 1994 Dec;35(12):1994-5.
37. Knapp Jr. F, Beets A, Pinkert J, Kropp J, Lin W, Wang S. Rhenium radioisotopes for therapeutic radiopharmaceutical development. *International Seminar on Therapeutic Applications of Radiopharmaceuticals* 1999:59-66.
38. Boswell C, Brechbiel M. Development of radioimmunotherapeutic and diagnostic antibodies: An inside-out view. *Nuclear Medicine and Biology* 2007;34(7):757-78.
39. Pardridge W. Re-engineering biopharmaceuticals for delivery to brain with molecular trojan horses. *Bioconjugate Chemistry* 2008;19(7):1327-38.

40. Wu A, Olafsen T. Antibodies for molecular imaging of cancer. *Cancer Journal* 2008;14(3):191-7.
41. Patra M, Zarschler K, Pietzsch H, Stephan H, Gasser G. New insights into the pretargeting approach to image and treat tumours. *Chemical Society Reviews* 2016;45(23):6415-31.
42. Sharkey R, Goldenbuerg D. Cancer radioimmunotherapy. *Immunotherapy* 2011;3(3):349-70.
43. Deri MA, Zeglis BM, Francesconi LC, Lewis JS. PET imaging with ⁸⁹Zr: From radiochemistry to the clinic. *Nucl Med Biol* 2013 Jan;40(1):3-14.
44. Adumeau P, Carnazza KE, Brand C, Carlin SD, Reiner T, Agnew BJ, Lewis JS, Zeglis BM. A pretargeted approach for the multimodal PET/NIRF imaging of colorectal cancer. *Theranostics* 2016 Sep 28;6(12):2267-77.
45. van Dongen G, Visser G, Lub-de hooge M, De vries E, Perk L. Immuno-PET: A navigator in monoclonal antibody development and applications. *Oncologist* 2007;12(12):1379-89.
46. Serafini AN. From monoclonal antibodies to peptides and molecular recognition units: An overview. *J Nucl Med* 1993 Mar;34(3 Suppl):533-6.
47. van de Watering F, Rijpkema M, Robillard M, Oyen W, Boerman O. Pretargeted imaging and radioimmunotherapy of cancer using antibodies and bioorthogonal chemistry. *Frontiers in Medicine* 2014;1:44.
48. Goldenberg DM. Targeted therapy of cancer with radiolabeled antibodies. *J Nucl Med* 2002 May;43(5):693-713.
49. Karacay H, Sharkey RM, McBride WJ, Griffiths GL, Qu Z, Chang K, Hansen HJ, Goldenberg DM. Pretargeting for cancer radioimmunotherapy with bispecific antibodies: The role of the bispecific antibody's valency for the tumor target antigen. *Bioconjugate Chem* 2002 09/01;13(5):1054-70.
50. Sletten E, Bertozzi C. Bioorthogonal chemistry: Fishing for selectivity in a sea of functionality. *Angewandte Chemie International Edition* 2009;48(38):6974-98.
51. Sletten E, Bertozzi C. From mechanism to mouse: A tale of two bioorthogonal reactions. *Accounts of Chemical Research* 2011;44(9):666-76.
52. Vugts DJ, Vervoort A, Stigter-van Walsum M, Visser GW, Robillard MS, Versteegen RM, Vuldens RC, Herscheid JK, van Dongen GA. Synthesis of phosphine and antibody-azide probes for in vivo Staudinger ligation in a pretargeted imaging and therapy approach. *Bioconjug Chem* 2011 Oct 19;22(10):2072-81.

53. Rossin R, Verkerk PR, van den Bosch SM, Vulderson RC, Verel I, Lub J, Robillard MS. In vivo chemistry for pretargeted tumor imaging in live mice. *Angew Chem Int Ed Engl* 2010 Apr 26;49(19):3375-8.
54. Blackman ML, Royzen M, Fox JM. Tetrazine ligation: Fast bioconjugation based on inverse-electron-demand diels-alder reactivity. *J Am Chem Soc* 2008 Oct 15;130(41):13518-9.
55. Reiner T, Zeglis BM. The inverse electron demand diels-alder click reaction in radiochemistry. *J Labelled Comp Radiopharm* 2014 Apr;57(4):285-90.
56. Devaraj NK, Weissleder R. Biomedical applications of tetrazine cycloadditions. *Acc Chem Res* 2011 Sep 20;44(9):816-27.
57. Seitchik JL, Peeler JC, Taylor MT, Blackman ML, Rhoads TW, Cooley RB, Refakis C, Fox JM, Mehl RA. Genetically encoded tetrazine amino acid directs rapid site-specific in vivo bioorthogonal ligation with trans-cyclooctenes. *J Am Chem Soc* 2012 Feb 15;134(6):2898-901.
58. Knight JC, Cornelissen B. Bioorthogonal chemistry: Implications for pretargeted nuclear (PET/SPECT) imaging and therapy. *Am J Nucl Med Mol Imaging* 2014 Mar 20;4(2):96-113.
59. Rossin R, van Duijnhoven SM, Lappchen T, van den Bosch SM, Robillard MS. Trans-cyclooctene tag with improved properties for tumor pretargeting with the diels-alder reaction. *Mol Pharm* 2014 Sep 2;11(9):3090-6.
60. Hollander N. Bispecific antibodies for cancer therapy. *Immunotherapy* 2009 Mar;1(2):211-22.
61. Liu G, Mang'era K, Liu N, Gupta S, Rusckowski M, Hnatowich DJ. Tumor pretargeting in mice using (99m)tc-labeled morpholino, a DNA analog. *J Nucl Med* 2002 Mar;43(3):384-91.
62. Boerman OC, van Schaijk FG, Oyen WJ, Corstens FH. Pretargeted radioimmunotherapy of cancer: Progress step by step. *J Nucl Med* 2003 Mar;44(3):400-11.
63. Goldenberg DM, Sharkey RM, Paganelli G, Barbet J, Chatal JF. Antibody pretargeting advances cancer radioimmunodetection and radioimmunotherapy. *J Clin Oncol* 2006 Feb 10;24(5):823-34.
64. Sharkey RM, Karacay H, Cardillo TM, Chang CH, McBride WJ, Rossi EA, Horak ID, Goldenberg DM. Improving the delivery of radionuclides for imaging and therapy of cancer using pretargeting methods. *Clin Cancer Res* 2005 Oct 1;11(19 Pt 2):7109s-21s.
65. Sharkey RM, Chang CH, Rossi EA, McBride WJ, Goldenberg DM. Pretargeting: Taking an alternate route for localizing radionuclides. *Tumour Biol* 2012 Jun;33(3):591-600.

66. Zeglis BM, Sevak KK, Reiner T, Mohindra P, Carlin SD, Zanzonico P, Weissleder R, Lewis JS. A pretargeted PET imaging strategy based on bioorthogonal Diels–Alder click chemistry. *The Journal of Nuclear Medicine* 2013;54:1389-1396.
67. Radiolabeled fragments of monoclonal antibodies against carcinoembryonic antigen for localization of human colon carcinoma grafted into nude mice. *J Exp Med* 1983 08/01;158(2):413-27.
68. Halpern SE, Buchegger F, Schreyer M, Mach. Ludwig J-. Effect of size of radiolabeled antibody and fragments on tumor uptake and distribution in nephrectomized mice. *Clin Nucl Med* 1984;9(9).
69. Vito A, Alarabi H, Czorny S, Beiraghi O, Kent J, Janzen N, Genady AR, Alkarmi SA, Rathmann S, Naperstkow Z, et al. A ^{99m}Tc -labelled tetrazine for bioorthogonal chemistry. synthesis and biodistribution studies with small molecule trans-cyclooctene derivatives. *PLoS One* 2016;11(12):e0167425/1,e0167425/15.
70. Hoffman JM, Gambhir SS. Molecular imaging: The vision and opportunity for radiology in the future. *Radiology* 2007 Jul;244(1):39-47.
71. Lee S, Xie J, Chen X. Peptide-based probes for targeted molecular imaging. *Biochemistry* 2010 Feb 23;49(7):1364-76.
72. Massoud TF, Gambhir SS. Molecular imaging in living subjects: Seeing fundamental biological processes in a new light. *Genes Dev* 2003 Mar 1;17(5):545-80.
73. Weissleder R, Mahmood U. Molecular imaging. *Radiology* 2001 May;219(2):316-33.
74. Banerjee S, Pillai MR, Ramamoorthy N. Evolution of ^{99m}Tc in diagnostic radiopharmaceuticals. *Semin Nucl Med* 2001 Oct;31(4):260-77.
75. Jurisson S, Berning D, Jia W, Ma D. Coordination compounds in nuclear medicine. *Chem Rev* 1993 05/01;93(3):1137-56.
76. Maresca KP, Marquis JC, Hillier SM, Lu G, Femia FJ, Zimmerman CN, Eckelman WC, Joyal JL, Babich JW. Novel polar single amino acid chelates for technetium-99m tricarbonyl-based radiopharmaceuticals with enhanced renal clearance: Application to octreotide. *Bioconjug Chem* 2010 Jun 16;21(6):1032-42.
77. Jeong JM, Chung JK. Therapy with ^{188}Re -labeled radiopharmaceuticals: An overview of promising results from initial clinical trials. *Cancer Biother Radiopharm* 2003 Oct;18(5):707-17.

78. Knapp FF, Jr, Beets AL, Guhlke S, Zamora PO, Bender H, Palmedo H, Biersack HJ. Availability of rhenium-188 from the alumina-based tungsten-188/rhenium-188 generator for preparation of rhenium-188-labeled radiopharmaceuticals for cancer treatment. *Anticancer Res* 1997 May-Jun;17(3B):1783-95.
79. Ercan MT, Caglar M. Therapeutic radiopharmaceuticals. *Curr Pharm Des* 2000 Jul;6(11):1085-121.
80. Guo H, Gallazzi F, Miao Y. Design and evaluation of new tc-99m-labeled lactam bridge-cyclized alpha-MSH peptides for melanoma imaging. *Mol Pharm* 2013 Apr 1;10(4):1400-8.
81. Liu S. Bifunctional coupling agents for radiolabeling of biomolecules and target-specific delivery of metallic radionuclides. *Adv Drug Deliv Rev* 2008 Sep;60(12):1347-70.
82. Blok D, Feitsma RI, Vermeij P, Pauwels EJ. Peptide radiopharmaceuticals in nuclear medicine. *Eur J Nucl Med* 1999 Nov;26(11):1511-9.
83. Okarvi SM. Peptide-based radiopharmaceuticals: Future tools for diagnostic imaging of cancers and other diseases. *Med Res Rev* 2004 May;24(3):357-97.
84. Giblin MF, Wang N, Hoffman TJ, Jurisson SS, Quinn TP. Design and characterization of alpha-melanotropin peptide analogs cyclized through rhenium and technetium metal coordination. *Proc Natl Acad Sci U S A* 1998 Oct 27;95(22):12814-8.
85. Bormans G, Cleynhens B, Jose D, Hoogmartens M, De Roo M, Verbruggen A. Synthesis and biological characteristics of the four stereoisomers of 99mTc-N,N'-bis-(mercaptoacetyl)-2,3-diaminopropanoate. *Int J Rad Appl Instrum B* 1990;17(5):499-506.
86. Delmon-Moingeon LI, Mahmood A, Davison A, Jones AG. Strategies for labeling monoclonal antibodies and antibody-like molecules with technetium-99m. *J Nucl Biol Med* 1991 Jan-Mar;35(1):47-59.
87. Bormans G, Cleynhens B, Adriaens P, de Roo M, Verbruggen A. Synthesis and labelling characteristics of 99mTc-mercaptoacetyltripeptides. *J Labelled Compd Radiopharmaceut* 1993;33(11):1065-78.
88. Cantorias MV, Howell RC, Todaro L, Cyr J, Berndorff D, Rogers RD, Francesconi LC. MO tripeptide diastereomers (M) 99/99mTc, re): Models to identify the structure of 99mTc peptide targeted radiopharmaceuticals. *Inorganic Chemistry* 2007;46:7326-7340.
89. Kung HF, Guo YZ, Yu CC, Billings J, Subramanyam V, Calabrese JC. New brain perfusion imaging agents based on 99mTc-bis(aminoethanethiol) complexes: Stereoisomers and biodistribution. *J Med Chem* 1989 Feb;32(2):433-7.

90. Lever SZ, Burns HD, Kervitsky TM, Goldfarb HW, Woo DV, Wong DF, Epps LA, Kramer AV, Wagner HN, Jr. Design, preparation, and biodistribution of a technetium-99m triaminedithiol complex to assess regional cerebral blood flow. *J Nucl Med* 1985 Nov;26(11):1287-94.
91. Meegalla SK, Plossl K, Kung MP, Chumpradit S, Stevenson DA, Kushner SA, McElgin WT, Mozley PD, Kung HF. Synthesis and characterization of technetium-99m-labeled tropanes as dopamine transporter-imaging agents. *J Med Chem* 1997 Jan 3;40(1):9-17.
92. Sharp PF, Smith FW, Gemmell HG, Lyall D, Evans NT, Gvozdanovic D, Davidson J, Tyrrell DA, Pickett RD, Neirinckx RD. Technetium-99m HM-PAO stereoisomers as potential agents for imaging regional cerebral blood flow: Human volunteer studies. *J Nucl Med* 1986 Feb;27(2):171-7.
93. Rose DJ, Maresca KP, Kettler PB, Chang YD, Soghomomian V, Chen Q, Abrams MJ, Larsen SK, Zubieta J. Synthesis and characterization of rhenium thiolate complexes. crystal and molecular structures of $\text{NBu}_4[\text{ReO}(\text{H}_2\text{O})\text{Br}_4] \cdot 2\text{H}_2\text{O}$, $\text{Bu}_4\text{N}[\text{ReOBr}_4(\text{OPPh}_3)]$, $\text{ReO}(\text{SC}_5\text{H}_4\text{N})_3$, $\text{ReO}(\text{SC}_4\text{H}_3\text{N}_2)_3[\text{ReO}(\text{OH})(\text{SC}_5\text{H}_4\text{N}-3,6-(\text{SiMe}_2\text{But})_2)_2]$, $\text{re}(\text{N}_2\text{COC}_6\text{H}_5)(\text{SC}_5\text{H}_4\text{N})\text{cl}(\text{PPh}_3)_2$, and $\text{re}(\text{PPh}_3)(\text{SC}_4\text{H}_3\text{N}_2)_3$. *Inorg Chem* 1996 01/01;35(12):3548-58.
94. Mahood A, Halpin W, Baidoo K, Sweigart D, Lever S. Synthesis and characterization of N-ethyl-diaminedithiol oxotechnetate(V): A potential lung imaging agent. In: *Technetium and rhenium in chemistry and nuclear medicine*. 3rd ed. New York: Cortina-Raven Press; 1990. .
95. Tisato F, Refosco F, Bandoli G. Structural survey of technetium complexes. *Coord Chem Rev* 1994 11/01;135:325-97.
96. Wong E, Fauconnier T, Bennett S, Valliant J, Nguyen T, Lau F, Lu LF, Pollak A, Bell RA, Thornback JR. Rhenium(V) and technetium(V) oxo complexes of an N(2)N'S peptidic chelator: Evidence of interconversion between the syn and anti conformations. *Inorg Chem* 1997 Dec 3;36(25):5799-808.
97. Bœreau VM, Khan SI, Abu-Omar M. Synthesis of enantiopure oxorhenium(V) and arylimidorhenium(V) $\text{ReO}_3 + 2\text{Re} \cdot$ schiff base complexes. X-ray diffraction, cyclic voltammetry, UV-Vis, and circular dichroism characterizations. *Inorg Chem* 2001 12/01;40(26):6767-73.
98. Cheng Y, Yan YB, Liu J. Spectroscopic characterization of metal bound phytochelatin analogue (glu-cys)₄-gly. *J Inorg Biochem* 2005 Oct;99(10):1952-62.

Curriculum Vitae

Vanessa A. Sanders

Vanessa A. Sanders
270 W. 153rd Street Apt 14
New York, NY 10039

Telephone: 321-536-3540
E-mail: vsndrs1@aol.com

Citizenship: USA

Goal: To optimize isotope separation techniques, complete fundamental research in novel radiometal ligand complexes, and to study the biological impacts of these complexes.

Education History

August 2004– May 2006	A.A in science	Seminole Community College, Sanford FL
August 2006– May 2009	B.A. in Chemistry	Florida Memorial University, Miami Gardens, FL
August 2009-Present Anticipated graduation December 2016	Ph.D. in Radiochemistry	University of Nevada Las Vegas, Las Vegas, Nevada

Research History

Summer 2007	Intern Researcher	Scripps Research Institute, Jupiter FL	Manipulated Mouse RNA as part of Alzheimer's related research
Summer 2008	Intern Researcher	Nuclear Engineering Teaching Laboratory, University of Texas at Austin, Austin Texas	Obtained prompt gamma ray spectra for several encasing materials
Fall 2009-Present	Graduate Student	University of Nevada at Las Vegas	Characterizing Re/ ^{99m} Tc complexes for radiopharmaceuticals
Fall 2014- Present	Visiting Graduate Student	Hunter College of the City University of New York	Characterizing Re/ ^{99m} Tc complexes for radiopharmaceuticals

Synergistic Activities

Fall 2007- Spring 2009	Was a part of the inaugural class for a Radiochemistry undergraduate major at Florida Memorial University through the help of the Radiochemistry Education Award Program
Fall 2009	Conducted X-ray Absorption Fine Structure experiments at Argonne National Laboratory

April 2010- April 2012	Co-Chaired the 2012 American Nuclear Society Student Conference. Co-wrote winning proposal to host student conference at UNLV, organized the plenary seminars, technical presentations, workshops and tours. The conference was the largest to date hosting 600 attendees
August 2011-Present	National Science Foundation- Integrative Graduate Education and Research Traineeship (NSF-IGERT) Fellow.
August 2011-Present	Initiated the radiopharmaceutical efforts at UNLV. Collaborated with Hunter College and Memorial Sloan Kettering Cancer Center.
Spring 2013	Received Radiological Worker II training at the Nevada National Security Site
Summer 2013	Collected melt glass at the Nevada National Security site as a part of the Nuclear Forensics Summer School held at UNLV
Summer 2013- Present	Mentored undergraduate student in laboratory settings as a part of the Nuclear Fuel Cycle Summer School held at UNLV and research activities at Hunter College
Fall 2015- Present	Consulted Hunter College Radiation Safety Office on laboratory radiation safety. Conducted post experiment radiation surveys. Was offered radiation safety trainer position

Manuscripts In Preparation

Kimberly Fung, Vanessa Sanders , Justin Walsh, Lynn Francesconi, Brian Zeglis	Small Molecule Imaging Agents- Review
Vanessa Sanders , David Iskhakov, Huseyin Cicek, Dalya Abdel-Atti, Ken Czerwinski, Jason Lewis, Lynn Francesconi	Synthesis, Characterization, and Biological Studies of ^{99m}Tc and ^{188}Re Peptides
Vanessa Sanders , David Iskhakov, Dalya Abdel-Atti, Ken Czerwinski, Jason Lewis, Lynn Francesconi	A Pretargeted SPECT Imaging and Radiotherapy Strategy Employing ^{99m}Tc and ^{188}Re based on Bioorthogonal Diels-Alder Click Chemistry

Presentations

Spring 2011	American Nuclear Society Student Conference, Atlanta, Georgia	The Characterization of $\text{Re}/^{99m}\text{Tc}$ -Complexes for Radiopharmaceuticals
--------------------	---	---

Fall 2011	242 nd American Chemical Society National Meeting and Expo, Denver, Colorado	The Characterization of Re/ ^{99m} Tc-Complexes for Radiopharmaceuticals
Fall 2013	243 rd American Chemical Society National Meeting and Expo, Indianapolis, Indiana	The Characterization of Re/ ^{99m} Tc-Complexes for Radiopharmaceuticals
Spring 2014	Radiochemical Conference, Marianske Lazne, Czech Republic	The Characterization of Re/ ^{99m} Tc-Complexes for Radiopharmaceuticals
Spring 2015	21 st International Symposium on Radiopharmaceutical Sciences, Columbia, Missouri	A Pretargeted SPECT Imaging Strategy Employing Technetium-99m based on Bioorthogonal Diels-Alder Click Chemistry
Fall 2016	World Molecular Imaging Conference, New York, New York	A Pretargeted SPECT Imaging Strategy Employing Technetium-99m based on Bioorthogonal Diels-Alder Click Chemistry

Outside Activities

Fall 2004- Spring 2009	Received multiple athletic undergraduate scholarships including Basketball (5years), Volleyball (1year), track and field (2years)
Spring 2007- Present	Member of Zeta Phi Beta Sorority Incorporated. Current office held; Pacific Regional Secretary. Takes recording of all business meetings, sends correspondence on behalf on the executive board.

References

Dr. Ken Czerwinski	Chemistry Professor in Radiochemistry at the University of Nevada at Las Vegas	702-895-0501 czerwin2@unlv.nevada.edu
Dr. Lynn Francesconi	Professor of Chemistry at Hunter College of City University of New York	212-772-5353 lfrances@hunter.cuny.edu
Dr. Dimitri Tamalis	Assistant Professor at Florida Memorial University	305-626-0267 dtamalis@fmuniv.edu
Dr. Rose Mary Stiffin	Chair of the department of Health and Natural sciences at Florida Memorial	305-626-3697 rstiffin@fmuniv.edu

